Università
di Genova

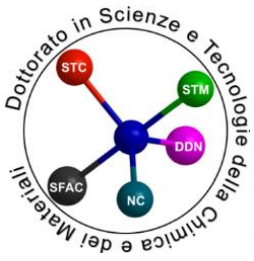

Università degli Studi di Genova

Istituto Italiano di Tecnologia

Doctorate School
in
Sciences and Technologies of Chemistry and Materials

Marco Piccinni

Synthesis, dispersion, electrochemical and optical properties of layered hydroxides nanosheets

PhD Cycle: XXXV

Curriculum: Nanochemistry

Years: 2019-2022

Supervisors: Dr. Francesco Bonaccorso (IIT), Prof. Diego Colombara (UniGe)

Institutional e-mail address: marco.piccinni@iit.it

Keywords: LDH, hydrotalcite, nickel-iron, water splitting, ligand field theory

Abstract (English)

Layered double hydroxides (LDHs) are a class of layered materials consisting of positive charged brucite-like layers spaced by water molecules and counterbalancing anions. In this thesis I will present how LDHs interact with carboxylates anions by studying the influence of such anions on the physical and electrochemical properties of LDHs. In addition, I will also discuss how transition metal elements behave when confined in the two-dimensional environment of LDH layers.

In Chapter 1, I will introduce the reader to layered materials with particular focus on transition metal dichalcogenides, transition metal oxide/hydroxides and clay minerals, since these classes of materials share similar properties with LDHs. I will also describe the exfoliation process of layered materials in terms of surface energy and solubility parameters. In Chapter 2, I will mention the history of LDHs, from their discovery to their current applications. Then I will describe the LDHs crystal structure, structural defects, and the relative X-ray diffraction patterns. In chapter 3, I will first describe the history and current developments in the liquid phase exfoliation of LDHs. Then I will provide the physical explanation of the zeta potential (ζ) and I will explain how it can be exploited to achieve the exfoliation of LDHs. Lastly, I will discuss the liquid phase exfoliation process of carbonate- and citrate-intercalated NiFe-LDH nanosheets, dispersed in ethanol and water, in terms of surface energy (introduced in Chapter 2) and ζ. A brief description of the LDH nanosheets morphology and size is also included. In Chapter 4, I will introduce the reader to the electrochemical water splitting, and the potential future overcome that LDH could have as electrocatalysts for the anodic reaction (*i.e.*, the oxygen evolution). Hence, I will also provide a detailed description of the oxygen evolution reaction (OER) kinetics in terms of overpotential applied and Tafel slope. Lastly, I will describe the OER electrocatalytic properties of NiFe-LDH and how the presence of acetate or citrate anions affects the OER rate determining step. In Chapter 5, I will describe the synthetic route, which I developed and optimized, to directly produce the single layer LDH nanosheets by exploiting the coordination chemistry of citric acid. Then, by means of pH-potentiometric titrations and electronic (optical) spectroscopy, I will perform an in-situ analysis of the reaction mechanism of NiFe-LDH nanosheets formation. Eventually, in Chapter 6 I introduce the reader to the ligand filed theory (LFT). Through the lens of LFT, I will perform an in-depth analysis on the electronic spectra of NiFe-LDHs. The nature of observed ligand field transitions will be described in detail. Then, I will provide for the first time the ligand filed parameters and the ionic degree of nickel and iron in LDH crystal lattices.

Abstract (Italian)

Le idrotalciti, conosciute anche come “Layered Double Hydroxides” (LDH), sono materiali costituiti da idrossidi lamellari, nei quali è presente una carica elettrica netta positiva sulla superficie delle lamelle. La struttura cristallina degli LDH è analoga al minerale brucite; tuttavia, la carica positiva sulle lamelle è controbilanciata da anioni intercalati tra le lamelle. In questa tesi presenterò come gli LDH interagiscono con anioni carbossilato tramite lo studio dell’effetto che tali anioni hanno sulle proprietà fisiche ed elettrochimiche degli LDH. Inoltre, discuterò il comportamento di elementi di transizione confinati all’interno dell’ambiente bidimensionale fornito dagli LDH.

Nel capitolo 1 introdurrò il lettore ai materiali lamellari ponendo particolare attenzione su calcogenuri, ossi e idrossidi di metalli di transizione, e infine le argille; in quanto tali materiali condividono simili proprietà con gli LDH. Nel medesimo capitolo descriverò il processo di esfoliazione dei materiali lamellari, attraverso una trattazione sull’energia di superficie ed i parametri di solubilità. Nel capitolo 2 tratterò gli aspetti storici degli LDH, dalla loro scoperta ai loro attuali utilizzi e, successivamente, descriverò la struttura cristallina degli LDH, compresi i loro difetti strutturali e le rispettive figure di diffrazione di raggi X. Nel capitolo 3 riporterò gli sviluppi nell’esfoliazione in fase liquida degli LDH, fornendo al lettore l’interpretazione fisica del potenziale zeta (ζ) e spiegherò come esso possa essere sfruttato al fine di esfoliare gli LDH. Infine, discuterò, in termini di energia di superficie e ζ, il processo di esfoliazione degli LDH, intercalati con anioni carbonato e citrato, dispesi in acqua ed etanolo. Nel capitolo 3 è inoltre inclusa una breve descrizione della morfologia e dimensioni delle particelle di LDH disperse. Nel capitolo 4 introdurrò il lettore al processo di elettrolisi dell’acqua, ed i potenziali sviluppi futuri degli LDH come elettro-catalizzatori per la reazione anodica nell’elettrolisi (la reazione di sviluppo di ossigeno). Fornirò una descrizione dettagliata della reazione di sviluppo di ossigeno (OER) nei termini della sovratensione necessaria per far avvenire tale reazione, e sua pendenza di Tafel. Infine, descriverò le proprietà elettro-catalitiche di NiFe-LDH verso l’OER, e come la presenza di anioni acetato o citrato influenza lo stadio determinante nella cinetica di reazione. Nel capitolo 5 descriverò il processo di sintesi, da me sviluppato e ottimizzato, in grado di produrre direttamente nano-fogli di LDH spessi una singola lamella. Tale processo sfrutta la chimica di coordinazione dell’acido citrico. Successivamente, combinando titolazioni potenziometriche del pH con la spettroscopia ottica, fornirò un’analisi in situ del meccanismo di formazione di nano-fogli di NiFe-LDH. Infine, nel capitolo 6 introdurrò il lettore alla teoria del campo dei leganti. Tramite tale teoria, effettuerò un’analisi dettagliata delle transizioni elettroniche osservate negli spettri ottici degli LDH. In seguito, fornirò i parametri del campo dei leganti ottenuti dalla suddetta analisi, assieme al grado del carattere ionico del ferro e del nichel collocati nel reticolo cristallino degli LDH.

Table of contents

List of figures

Chapter 1

Chapter 2

Chapter 3

Chapter 4

Chapter 5

Chapter 6

List of tables

Chapter 3

Chapter 6

Chapter 9

1. Layered materials

Layered materials are a class of natural and synthetic solids resulting from the stacking, on top of each other, of lamellar units (*i.e.*, layers) that are one or few atoms thick. The nature of cohesive forces between layers does not involve chemical bonds, but it is limited to van der Waals forces, hydrogen bonds and electrostatic attraction. For this reason, crystals of layered materials can be easily split along planes parallel to layers, exposing flat surfaces. In mineralogy and material science this property is referred to as "perfect basal cleavage".

"A material is defined as layered if it possesses a perfect basal cleavage".

By iteratively repeating the cleavage process, a layered material can be reduced to atomically thin sheets (usually less than 10 layers). In this case, the entire process is named "delamination" or "exfoliation", while the atomically thin sheets are referred to as "nanosheets".

"A material composed solely by nanosheets is referred to as 2D-material".

In the following first section of this chapter, I will briefly introduce the reader to layered materials and their exfoliated counterparts. I will provide a more detailed description of the structure and the electronic properties of transition metal dichalcogenides, transition metal oxides and hydroxides, and eventually clays minerals. In fact, these three classes of materials share similar properties with layered double hydroxides, *i.e.*, the topic of this thesis. Next, in the second section of this chapter I will describe the exfoliation process from a thermodynamic viewpoint.

1.1. An overview on layered materials

The idea that 2D-materials can be fabricated by cleaving layered materials down to mono-/few-layers nanosheets was present since the '60s of the 20th century[1–5]. In 2004, K.S. Novoselow and A.K. Geim showed that graphite (**Figure 1.1**) can be exfoliated into atomically thin films of carbon atoms (*i.e.*, graphene) and demonstrated the possibility to fabricate evenly thin electronic devices[6]. Since then, layered materials have drawn an ever-increasing interest from the scientific community, regarding the production, characterization, and future applications of 2D-materials[7]. Undoubtedly, graphene is the most studied 2D-material due to its remarkable mechanical properties, chemical stability, and its electrical and thermal conductivity, making graphene the backbone material for future electronics and energy storage/conversion devices[8–11]. However, the lack of semiconducting and catalytic properties in graphene requires it to be coupled with different 2D-materials for devices fabrication[7–9,12–14]. Despite single-element 2D-materials based on Si, Ge, Sn and P have been synthetized (*i.e.*, silicene, germanene, stannene and phosphorene), the former three are stable only as free-standing monolayer, while their production is limited to deposition techniques[15]. This is related to the s-p hybridization in Si, Ge and Sn. In fact, these group IV elements have a preferential sp^3 hybridization, which promotes the formation of covenants bonds between layers yielding to the corresponding bulk (non-layered) crystal[15]. On the contrary, phosphorene is stable as both single- and few-layers 2D-material, and it is produced from the exfoliation of black phosphorous (*cf.* **Figure 1.1**)[15]. Phosphorene is a semiconducting material having a tuneable bandgap, from 1.0 to 0.3 eV, that depends on the number of layers

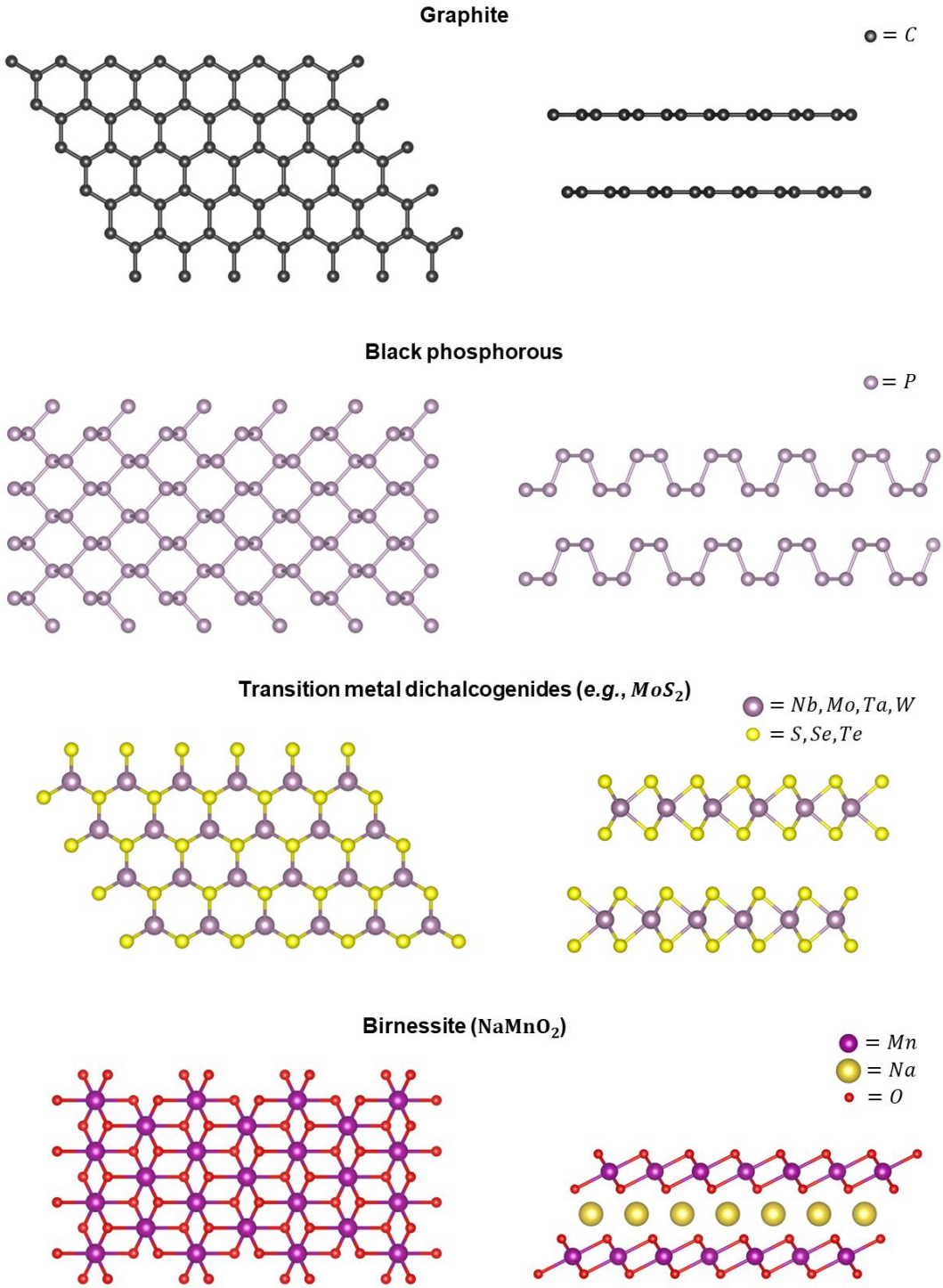

Figure 1.1. *Top view (left) and side view (right) of graphite, black phosphorous, MoS_2 and birnessite.*

making up its nanosheets[15–17]. This property makes phosphorene suitable for the fabrication of atomically thin field effect transistors and photoluminescent devices[16,17].

A popular alternative to phosphorene is represented by single-layer MoS_2,[11] which is a transition metal dichalcogenide (TMD). TMDs are materials in which transition metal atoms, usually from the 5th or 6th period, are sandwiched between group VI elements (*i.e.*, S, Se, Te), as illustrated in **Figure 1.1**. For the sake of clarity, despite oxygen belongs to the group VI, transition metal oxides, hydroxides and oxyhydroxides represent a separate class of materials. TMDs possess different electronic properties depending on the number of electrons occupying the transition metal d orbitals[18,19]. Bulk TMDs present several different polymorphs, which are defined by the stacking of layers inside the resulting crystallographic cell (*i.e.*, hexagonal, or rhombohedral stacking). However, single layer TMDs are restricted to two main phases, 1H and 1T, in which each transition metal atom is coordinated by six chalcogen atoms in D_{3h} (body centred prism) or D_{3d} (body centred antiprism) point group geometries, respectively. The geometry adopted by TMDs strongly depends on the filling of transition metal d orbitals[18,19]. If the transition metal has a d^0 (*e.g.*, $Hf^{(IV)}$) or a d^3 (*e.g.*, $Re^{(IV)}$) electronic configuration, a D_{3d} geometry is adopted. In the former case, the resulting TMD behaves as a semiconductor, because the bandgap is defined by the filled chalcogen p-band and the empty transition metal d orbitals. On the contrary, TMDs having a d^3 configuration behave as conductors, because of the half-filled t_{2g} orbitals originating from the ligand field splitting of the transition metal d orbitals[i]. The D_{3h} geometry is adopted if the transition metal in TMDs has a d^1 (*e.g.*, $Nb^{(IV)}$) or d^2 (*e.g.*, $Mo^{(IV)}$) configuration. In the D_{3h} symmetry, the ligand field splits the transition metal d orbitals into the a_1', e' and e'' orbitals. Hence, in TMDs with a d^2 configuration the a_1' orbitals are full, giving the TMD a semiconductor behaviour with a bandgap that corresponds to the separation between the a_1' and e' orbitals. On the contrary the half filled a_1' orbitals in d^1 TMDs, yields a conductor behaviour. In addition, the bandgap of d^2 TMDs is tuneable (similarly to phosphorene) while also shifting its nature from indirect to direct in monolayer nanosheets[20]. *E.g.*, bulk MoS_2 possesses an indirect bandgap of 1.29 eV, while monolayer MoS_2 has a direct bandgap of 1.8 eV. The change in the bandgap nature is ascribed to the broken symmetry that is achieved by exfoliating MoS_2 down to single layer[20,21]. Because of the variety of electronic properties of TMDs, they are promising candidates as active component in the fabrication of 2D electronic devices and energy conversion applications in the future[14,22–25].

Layered transition metal oxides (TMOs) and their hydroxide counterparts (TMHs) represent a vast class of materials, of which each subclass deserves its own review[26–28]. Hence, for the sake of conciseness, I confine the description of TMOs and TMHs within birnessite- and brucite-like structures, respectively (*cf.* **Figures 1.1** and **1.2**). Analogously to TMDs, both birnessite-like TMOs and brucite-like TMHs structures are made of layers in which transition metal atoms, from the 4th period, are sandwiched between oxygen atoms. However, in contrast to TMDs, TMOs and TMHs are limited to the D_{3d} point group symmetry, while covering all possible electronic configurations of d orbitals (*i.e.*, from d^0 to d^{10}). Moreover, because of the high electron paring energy[ii] displayed by transition metal elements from the 4th period (up to 3.7 eV for $Fe^{(III)}$), the filling of the t_{2g} and

[i] The orbital wavefunctions resulting from the ligand filed splitting are labelled according to the Mülliken notation. a, e and t letters indicate singly, doubly, and triply degenerate orbitals, respectively. 1 and 2 subscripts indicate symmetry and anti-symmetry respect to the non-principal rotation axis. g and u subscripts indicate symmetry and anti-symmetry respect to an inversion centre. $'$ and $''$ superscripts indicate symmetry and anti-symmetry respect to the mirror plane perpendicular to the principal rotation axis.

[ii] The electron paring energy is the energy difference between the high-spin and low-spin electronic configurations in d orbitals.

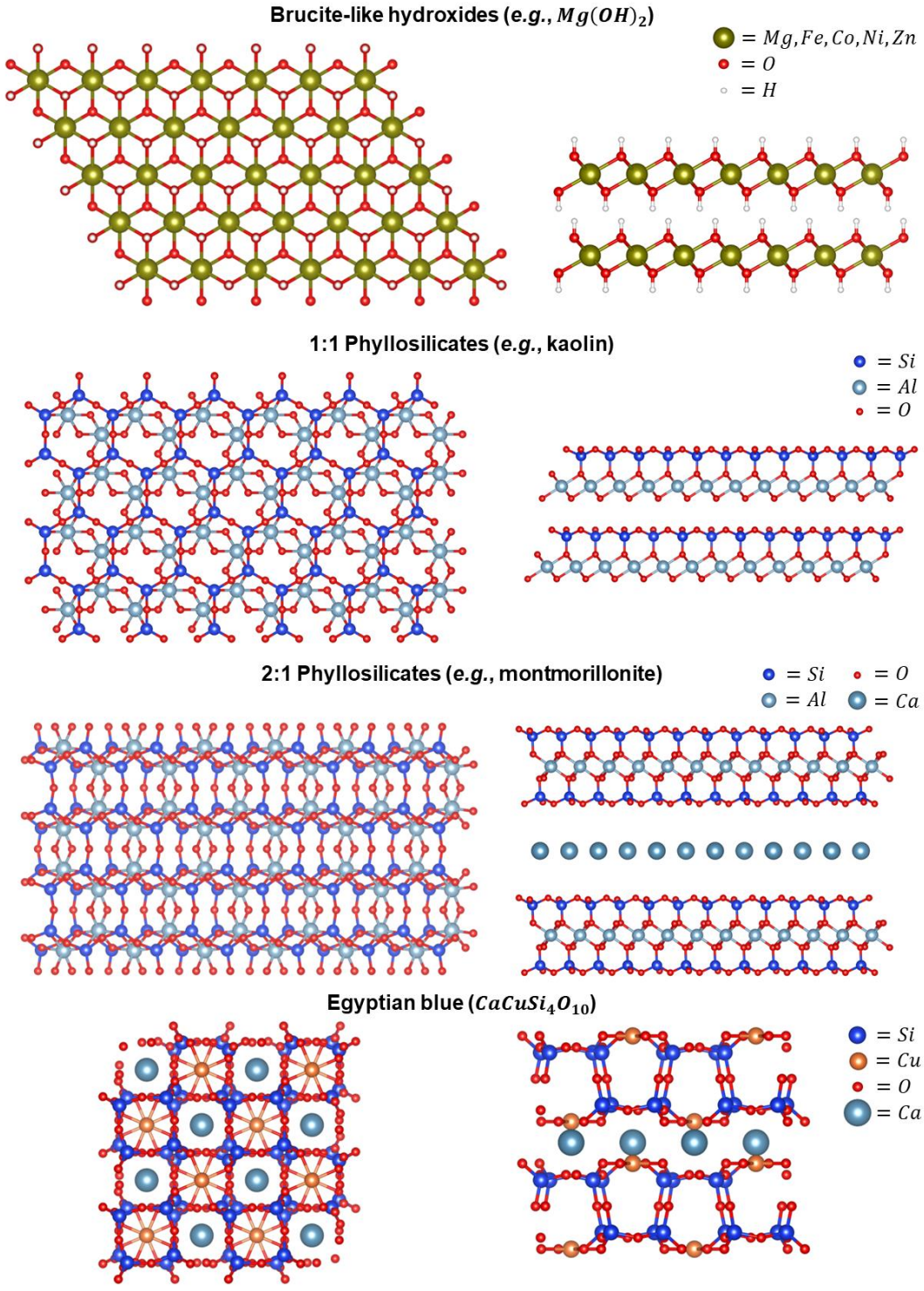

Figure 1.2. *Top view (left) and side view (right) of brucite, kaolin, montmorillonite and Egyptian blue.*

e_g orbitals favours half-filled configurations, maximizing the overall electronic spin[29]. Hence, TMOs and TMHs display unique magnetic properties. *E.g.*, single-layer $Ni(OH)_2$ possesses a ferromagnetic ordering, while bulk $Ni(OH)_2$ possesses an antiferromagnetic ordering between

layers[30–33]. Moreover, by heavy doping $Ni(OH)_2$ with paramagnetic ions (e.g., Cr^{3+} or Fe^{3+}), a spin frustrated system is obtained, yielding a 2D spin-glass[i] material[31,34]. Recently, has also been proposed that spin-glass materials possess enhanced electrocatalytic properties respect to their antiferromagnetic counterparts[35]. Because TMOs and TMHs are limited to the D_{3d} point group symmetry, the oxidation state of the transition metal can be reversibly changed with minimal distortion of its coordination environment. This makes TMOs and TMHs pivotal materials for energy storage applications. In fact, $Ni(OH)_2$ can be reversibly oxidated to $NiOOH$, with the concomitant release of H^+, while retaining the brucite-like layered structure[30]. For this reason, $Ni(OH)_2$ is widely used as cathode for nickel-cadmium and nickel-metal-hydride batteries[30]. Analogously, $LiCoO_2$ is the first TMO used in Li-ion batteries, since $Co^{(III)}$ can be partially oxidized into $Co^{(IV)}$ with a concomitant release of Li^+ cations[36,37]. However, nowadays $LiCoO_2$ has been substituted by cheaper mixed metal oxide layered materials known as NMC (*i.e.*, $LiNi_{1-x-y}Mn_xCo_yO_2$)[36,37].

Clay minerals are the first class of layered materials used by mankind. Clay minerals originate from hydrogeological processes which grind aluminium-silicates rocks into thin sheets containing silica (*i.e.*, SiO_2) and gibbsite (*i.e.*, $Al(OH)_3$) linked together by oxygen atoms. The approximate ratio between $Si^{(IV)}$ and $Al^{(III)}$ in clay sheets is 1:1 or 2:1, providing the name for their respective clay family, *i.e.*, 1:1 and 2:1 phyllosilicates[ii] (**Figure 1.2**). Furthermore, a deficiency of $Si^{(IV)}$ or $Al^{(III)}$ caused the inclusion of $Mg^{(II)}$ or $Fe^{(II)}$ species into the phyllosilicate layers, creates a negative surface charge which is compensated by the intercalation of alkali or alkali-earth cations and water molecules between layers. The nature of intercalated cation and the amount of water determinate different rheological and plastic properties of the clays[38–40]. Hence, clay materials can be engineered to fit in a multitude of applications, like catalysis[38], lubricants[41], polymeric composites[42,43], pharmaceutics and cosmetics[44]. This first completely synthetic clay consists into the Egyptian Blue (*i.e.*, $CaCuSi_4O_{10}$) dating to the third millennium B.C.[45] Originally conceived as pigment, the Egyptian Blue is now widely investigated because of its intense infrared light emission caused by the ligand field transitions of $Cu^{(II)}$ in square planar coordination[46,47]. In fact, not only the Egyptian Blue infrared light emission is pivotal in the characterization of art crafts[46], but also the research about Egyptian Blue exfoliation could lead to the fabrication of atomically thin infrared light emitting devices[47].

1.2. Liquid phase exfoliation and dispersions of layered materials

By considering a closed thermodynamic system[iii] in which an interface between an α phase and a β phase is present, the excess free energy due to the presence of the interface is defined as[48]:

$$\gamma = \left(\frac{\partial U'}{\partial A}\right)_{S',V'^{\alpha},V'^{\beta},n_i} . \qquad (\mathbf{1.1})$$

Where U' is the molar internal energy of the system, A the interface area, S' the molar entropy of the system, V'^{α} and V'^{β} are the molar volumes of the α and β phases, respectively. Lastly, n_i is

[i] A spin-glass is a magnetic state in which spins are randomly oriented.
[ii] From Greek *phýllon*, "leaf".
[iii] A closed thermodynamic system can exchange energy, but not matter, with the environment.

the number of the i^{th} chemical species[48]. Expressing γ as a function of the interface properties yields[48]:

$$\gamma \equiv U^s - TS^s - \sum_i \tilde{\mu}_i n_i^s \,. \qquad (\mathbf{1.2})$$

Where U^s and S^s are the excess of energy and entropy at the interface, respectively. T is the absolute temperature, n_i^s is the excess in the number of the i^{th} chemical species at the interface, and $\tilde{\mu}_i$ is the electrochemical potential of the i^{th} chemical species[i]. If there is no excess of the i^{th} chemical specie at the interface, and no electrostatic potential difference is present at the interface, the summatory term in $(\mathbf{1.2})$ is zero. Hence γ corresponds to both the Gibbs (G^s) and Helmholtz (F^s) free energy of the interface as follows:

$$\gamma \equiv U^s - TS^s = G^s = F^s \qquad (\mathbf{1.3})$$

Furthermore, γ can be expressed as[49]:

$$\gamma = \gamma^\alpha + \gamma^\beta - 2\sqrt{\gamma_d^\alpha \gamma_d^\beta} - 2\sqrt{\gamma_p^\alpha \gamma_p^\beta}\,, \qquad (\mathbf{1.4})$$

where γ^α and γ^β are contributions to excess free energy at the interface carried by the α and β phases, respectively. While γ_d^α and γ_p^α are the dispersive and polar component to γ^α as follows:

$$\gamma^\alpha = \gamma_d^\alpha + \gamma_p^\alpha \qquad (\mathbf{1.5})$$

An analogous statement is also valid for the β phase. In the case of a solid-liquid interface, γ can be estimated by the contact angle method through Young's equation, *i.e.*,

$$\gamma = \gamma^{solid} - \gamma^{liquid} \cdot \cos(\theta)\,, \qquad (\mathbf{1.6})$$

where θ is the contact angle between the solid-liquid interface and liquid surface. Moreover, γ^{liquid} is equal to its mechanical analogue: the surface tension (σ) of the liquid[48].

In the liquid phase exfoliation, bulk layered solid crystals are suspended into a liquid medium and exfoliated by means of shear forces or cavitation[50]. This process can be seen as an increase in the interface area between the solid phase (*i.e.*, the layered material) and the liquid medium. According to $(\mathbf{1.1})$, an increase in the interface area yields an increase in the internal molar energy of the system. Therefore, the system tends to release the excess energy to the environment reverting the exfoliation process, *i.e.*, the dispersed material coagulates. Hence, to obtain a stable dispersion of nanosheets, γ must be minimized. According to $(\mathbf{1.4})$, a close matching between γ^{solid} and γ^{liquid} (and their respective dispersive and polar components) must be achieved. However, the surface excess entropy of liquids ($S^{s,liquid}$) can be considered constant with a value ~0.1 mJ·m^{-2}·K^{-1}. Hence, it is more convenient to define the stability of nanosheets dispersed in a solvent as a function of $U^{s,liquid}$, instead of γ^{liquid}, since the former is independent by T. Moreover, the matching between the Hildebrand or Hansen solubility parameters of the solvent and the layered material facilitates the exfoliation processes. The Hildebrand parameter is defined as the square root of the cohesive energy density of a solvent, or a material as follows[51]:

[i] The electrochemical potential of the i^{th} chemical species is defined as $\tilde{\mu}_i = \mu_i + Z_i F\varphi$, where μ_i is the chemical potential of the i^{th} chemical species with Z_i the charge. F is the Faraday constant, and φ the Galvani potential[85], *cf.* also Chapter 3.1. The direct dependence of γ from the Galvani potential, for a planar plate capacitor, proceeds according to the Lippmann equation (*cf.* ref. [85]).

$$\delta_{Hil} = \sqrt{\frac{\Delta H_{vap} - RT}{V'}}\,, \qquad (\mathbf{1.7})$$

in which ΔH_{vap} is the enthalpy of vaporization, R the gas constant and V' the molar volume. In contrast, the Hansen model[51] defines the squared Hildebrand parameter as the sum of the squared contributions from dispersive (δ_d), polar (δ_p) and hydrogen bond components (δ_H), *i.e.*,

$$\delta_{Hil}^2 = \delta_d^2 + \delta_p^2 + \delta_H^2\,. \qquad (\mathbf{1.8})$$

Experimentally, suitable solvents for a proper dispersion are those which fall within a "small" sphere (*e.g.*, a sphere with radius ≤8 $MPa^{1/2}$) centred at a point corresponding to the material parameters. As an alternative to the close matching between γ^{solid} and γ^{liquid}, a dispersion can be also stabilized by the addition of a surfactant. From a thermodynamic viewpoint, a surfactant acts on the summatory term in $(\mathbf{1.2})$. Then, form $(\mathbf{1.2})$ follow that an excess of surfactant molecules at the interface lowers γ. *E.g.*, the dispersion of $Ni(OH)_2$ nanosheets is possible in water by adding sodium cholate as surfactant[52], despite water has a U^s of 102.7 $mJ{\cdot}m^{-2}$, while $Ni(OH)_2$ has a U^s of ~65-70 $mJ{\cdot}m^{-2}$.

2. Layered double hydroxides: an overview

In this chapter I briefly describe the history of layered double hydroxides from their discovery, the determination of their layered structure, their current applications in industry and research developments. Then I will provide a detailed description of layered double hydroxides crystal structures, structural defects, and their characteristics X-ray diffraction patterns.

2.1. History of layered double hydroxides

Layered double hydroxides (LDHs) are a family of natural[i] and synthetic layered materials constituted by the stacking of positively charged hydroxide layers spaced by charge counterbalancing anions and water molecules[53,54]. The first record about LDHs goes back to 1841 when a mineral was discovered in Sweden, later named as hydrotalcite, presenting itself as brittle plates or fibrous formations[54,55]. In 1915 E. Manasse determined the chemical composition of hydrotalcite to be a hydroxycarbonate of magnesium and aluminium[ii]. Fifty years later, the layered structure of hydrotalcite and the isomorphous mineral pyroaurite[iii] was determined by means of X-ray diffraction by R. Allmann in 1968 and H.F.W. Taylor in 1969. The nomenclature of LDH minerals was officially formalized in 2012[53]. In fact, during the 20th century, LDHs were also referred to as "hydrotalcite-like compounds" (shortened as HTlc)[53,54], while finding application in industry. For example, hydrotalcite provides alkaline surfaces able to catalyse epoxide polymerizations and aldolic condensations[54], whereas takovite[iv] is an effective redox catalyst for steam reforming[54]. Hydrotalcite is also used for antacid treatment against ulcers since it inhibits the activity of pepsin (a digestive enzyme) by buffering the stomach juice at pH ~4 [56]. Calcium-based LDHs are common concrete additives since they provide an enhancement of compressive and flexural strengths of the concrete by acting as fillers in its porous structure[57]. In addition, the presence of LDHs in reinforced concrete also provides protection from the corrosion of steel bars by capturing chloride anions and, at the same time, releasing anti-corrosion agents[57]. With the progressive transition to renewable, intermittent energy sources, the current research on LDH is focused on the production of LDH nanosheets based on iron-group elements (Fe, Co, and Ni) to be used for energy storage and conversion applications[58–60]. In the battery field of applications, LDHs based on iron group elements are either investigated as electrode materials for supercapacitors, Li-ion, Na-ion and Cl-ion batteries, or as precursors for mixed metal oxides to be used for the same purpose, as well as catalysts for water electrolysers and fuel cells[58–62]. LDH nanosheets are also currently investigated for other applications such as environmental remediation applications and cancer therapy. Noteworthy, the recent "alkaline vents hypothesis" correlate the presence of fougèrite[v] on the Hadean Ocean floor to the very origin of life on Earth[63,64].

[i] I refer to natural LDHs with their mineralogical name.
[ii] Hydrotalcite: $Mg_6Al_2(OH)_{16}CO_3 \cdot 4H_2O$.
[iii] Pyroaurite: $Mg_6Fe_2(OH)_{16}CO_3 \cdot 4H_2O$.
[iv] Takovite: $Ni_6Al_2(OH)_{16}CO_3 \cdot 4H_2O$.
[v] Fougèrite: $Fe_6^{(II)}Fe_2^{(III)}(OH)_{16}CO_3 \cdot 4H_2O$.

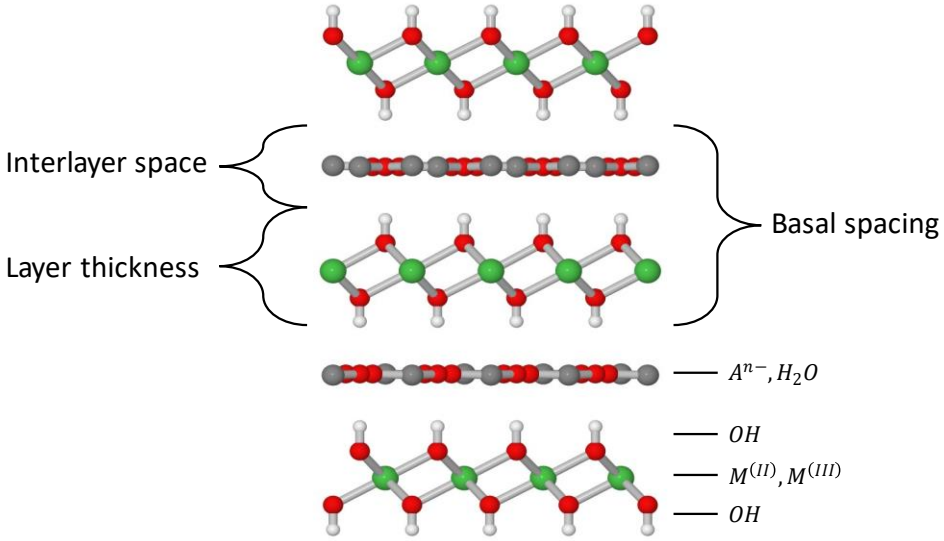

Figure 2.1. *Graphical representation of layered double hydroxides crystal structure.*

2.2. The structure of layered double hydroxides

The crystal structure of LDHs derives from brucite-like hydroxides[i] that represent a wide family of layered divalent-metal hydroxides belonging to the $P\bar{3}m1$ space group (*e.g.*, $Mg(OH)_2$, $Ca(OH)_2$, β-$Ni(OH)_2$). Their crystal structure is made by the stacking of hydroxide layers in which metal atoms, coordinated by six hydroxide groups, form layers of edge-sharing octahedral units with hydrogen atoms protruding on both sides of the layer. The transition from a brucite-like structure to an LDH results from the isomorphous substitution of a fraction of the divalent-metal species by trivalent ones. This process builds up a net positive charge on the hydroxide layers forcing the whole structure to swell, thus allowing the intercalation of charge counterbalancing anions and water molecules in the interlayer space. The resulting structure is represented in **Figure 2.1**, while the chemical composition of LDH materials can be summarized as follows:

$$\left[M^{(II)}_{1-x}M^{(III)}_{x}(OH)_2\right]^{x+} A^{n-}_{(x/n)} \cdot yH_2O \qquad (\mathbf{2.1})$$

Here $M^{(II)}$ refers to the divalent-metal species of the host brucite-like hydroxide, while $M^{(III)}$ refers to the guest trivalent-metal species. A^{n-} refers to inorganic or organic anions located in the interlayer space[ii]. The stoichiometric coefficient x usually assumes values between 0.2 and 0.33. Stoichiometric coefficients greater than 0.33 imply the presence of adjacent $M^{(III)}$ octahedral units, reducing the LDH crystallinity. Theoretically, LDHs crystallize in two different polymorphs belonging to the $R\bar{3}m$ space group ($3R$ polymorph) and the $P6_3/mmc$ space group ($2H$

[i] Brucite is the mineralogical name of natural $Mg(OH)_2$.
[ii] I refer to the charge of an ion with Arabic numbers on the top right of the chemical symbol, while I refer to the valence with Roman numbers placed in brackets. This choice is driven by the fact that, as I will discuss in Chapter 6, the metal-oxygen bond in LDHs retains a partial degree of covalence.

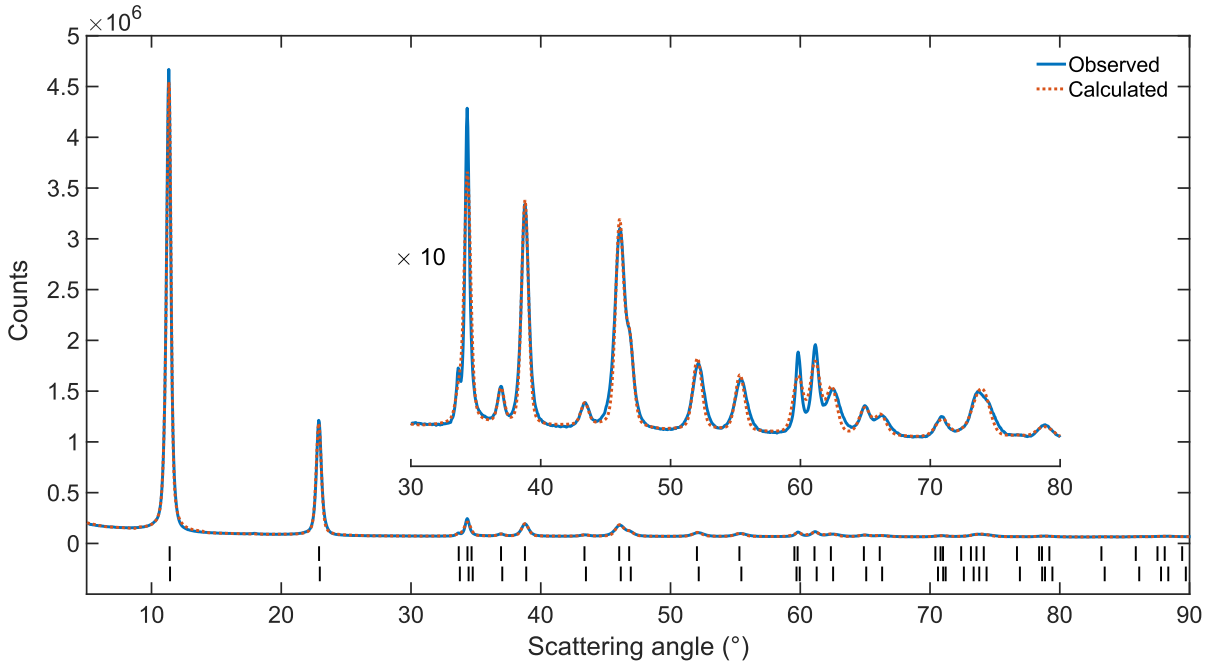

Figure 2.2. *X-ray diffraction pattern of carbonate intercalated $Ni_{0.75}Fe_{0.25}$-LDH. X-ray source: Cu Kα. Refined with Le Baile method.*

polymorph)[65]. However, the presence of stacking faults often leads to mixed interdigitated phases or turbostratic phases[65]. A typical LDH diffraction pattern is shown in **Figure 2.2**. An LDH diffraction patter can be considered divided into three main regions. The first region is located at scattering angles (2θ) below 30°, here the "basal reflections" appear. Basal reflections are related to $(00l)$ crystallographic planes that are parallel to the hydroxide layers, hence perpendicular to the unit cell c axis[66]. The second region, in the 2θ range from 30° to 55°, contains reflections related to $(0kl)$ and $(h0l)$ crystallographic planes. The shape of these reflections is indicative of faults in the layers stacking[65]. More in detail, sharp and well resolved reflections in this region, as shown in **Figure 2.2**, are typical for highly crystalline LDHs[65]. On the contrary, an asymmetric broad reflection covering the whole 30-55° 2θ region is indicative of a turbostratic disorder (*cf.* **Figure 2.3**). A layered material is defined as turbostratic when layers are randomly slid and twisted on top of each other. Being turbostratic is an intrinsic property of α-$Ni(OH)_2$[30] and LDHs intercalated with bulky anions[65,67–70]. Nevertheless, other two-dimensional materials can also be made turbostratic by restacking previously dispersed nanosheets[71,72]. The third region in the LDHs' diffraction pattern is located at 2θ angles above 55°. This region contains the (110) reflection, from which the unit cell a axis is obtained[54]. The unit cell a and c axes for a lattice of the hexagonal crystal family ($a = b \neq c$, $\alpha = \beta = 90°$, $\gamma = 120°$) is related to the crystallographic distances d_{hkl} as follows:

$$d_{hkl} = \frac{1}{(h^2 + k^2 + hk)a^{*2} + l^2c^{*2}} \,. \qquad (\mathbf{2.2})$$

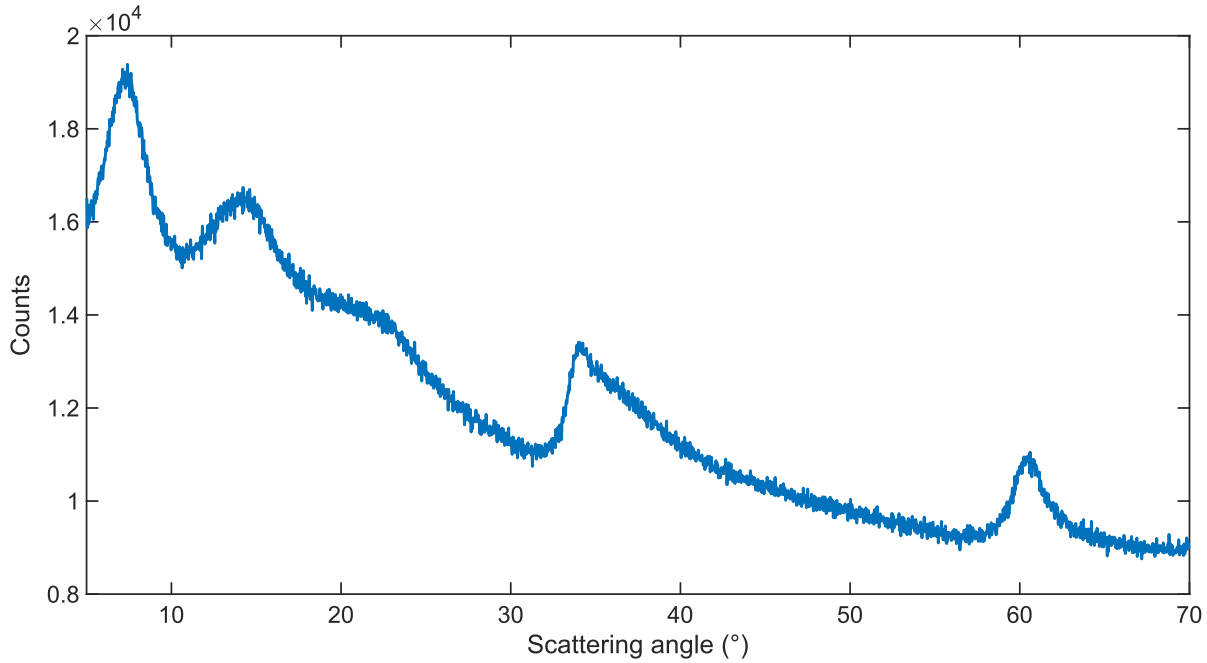

Figure 2.3. *X-ray diffraction pattern of turbostratic citrate intercalated $Ni_{0.75}Fe_{0.25}$-LDH. X-ray source: Cu Kα.*

Where a^* and c^* are the reciprocal lattice dimensions, defined as:

$$a^* = \frac{2}{a\sqrt{3}}\,, \qquad c^* = \frac{1}{c}\,. \tag{2.3}$$

While d_{hkl} are the lattice parameters calculated according to Bragg's law, as follows:

$$2d_{hkl}\sin(\theta) = n\lambda_{X\text{-}rays}\ . \tag{2.4}$$

Then, unit cell axes are calculated by the following relationships:

$$a = 2 \cdot d_{110} \tag{2.5}$$

and

$$c = \frac{1}{n}\sum_{i=1}^{n} l_i \cdot (d_{00l})_i\ . \tag{2.6}$$

Thus, the 2θ position of (110) provides the length of the a axis according to $(\mathbf{2.5})$, whereas, according to $(\mathbf{2.6})$, the 2θ position basal reflections yield the LDHs' unit cell c axis by the weighted mean of d_{00l} lattice parameters. For the sake of clarity, one third of the c axis and one half of the c axis are defined as the "basal spacing" in $R\bar{3}m$ and $P6_3/mmc$ polymorphs, respectively. Additional data on LDH crystallographic parameters are available in Appendix 8.1, **Table 8.2**.

3. Liquid phase exfoliation and dispersions of layered double hydroxides

In this chapter I provide a general overview on the current state of the liquid exfoliation of layered double hydroxides. Then I introduce the reader to the Debye-Hükel model which describes the interaction between charged surfaces and electrolytes, alongside with the physical meaning of the zeta potential. Lastly, I discuss the stability of LDH nanosheets dispersions in ethanol and suspension in water by means of the zeta potential. I will also describe the different morphologies of dispersed nanosheets.

3.1. History and current developments in the liquid phase exfoliation of layered double hydroxides

Contrary to van der Waals materials (*e.g.*, graphite, h-BN, MoS_2, etc.), the cohesive force between the layers in LDH materials results from the electrostatic attraction between the layers and the charge counterbalancing anions amid them, as well as a dense network on hydrogen bonds. The thermodynamic conclusions from Section 1.2 only partially hold in the LDH case[73], because the summatory term in $(\mathbf{1.3})$ cannot be assumed always zero due to the surface charge of LDHs. The first exfoliation of LDHs has been reported in 1999 by M. Adachi-Pagano, C. Forano and J.P. Besse who exfoliated ZnAl-LDHs in butanol by using sodium dodecyl sulphate as surfactant[4]. Two years later, T. Hibino and W. Jones reported the first surfactant-free exfoliation of LDHs, which was carried in formamide[74] that later became the most popular solvent for LDH exfoliation[75]. In the same period, E. Gardner, K.M. Huntoon and T.J. Pinnavaia delaminated alkoxide intercalated MgAl-LDHs in water[76]. Despite the authors never claimed the effective exfoliation of LDHs in water, it has been confirmed in 2004 in the study carried by T. Hibino and M. Kobayashi[77]. Nowadays, the exfoliation of LDH is possible in a multitude of solvent and mixture either with or without surfactants[75]. However, the dispersibility and exfoliation of LDHs in different solvents has been deeply characterized only recently by W. Yu et al. from a thermodynamic viewpoint[73]. In their article they reported the dispersion of few layers MgAl-LDHs with carbonate, nitrate, and chloride as intercalated anions in 40 different solvents and mixtures. Then, they also reported the efficiency of solvents and mixtures thereof at exfoliating LDHs down to single layers. Summarizing, the average surface energy (U^s) of LDHs is ~86 mJ·m^{-2}, with variations of ±2 mJ·m^{-2} depending on the metal composition and the intercalated anions[73]. Similarly, W. Yu et al. also reported the solubility Hansen parameters δ_d, δ_p and δ_H of LDHs to be 17.2±0.2, 10±1 and 26.0±2.5 MPa$^{1/2}$, respectively[73]. Hence, the most suitable solvents for LDH dispersions and exfoliation are: formamide, dimethyl sulfoxide, diethylene glycol and glycerol (*cf.* **Table 3.1**). Despite the safety concerns regarding the toxicity of formamide and diethylene glycol[i], all the aforementioned solvents have a boiling point higher than 150°C, at which temperature LDHs lose their structural water, altering the LDH properties[54]. Moreover, none of aforementioned solvents is effective at exfoliating carbonate based LDHs[73]. The impossibility to exfoliate resides into the high affinity of carbonate for LDH surfaces[78] and its negative charge, which is twice the charge of

[i] For toxicity and physical properties of solvents I refer to the safety data sheets from the supplier (Sigma-Aldrich).

chloride and nitrate anions. Nevertheless, the electrostatic nature of cohesive forces in LDHs can be exploited for different advantageous exfoliation strategies. For instance, LDHs intercalated with zwitterions can be exfoliated in water by finely tuning the pH[79]. Alternatively, LDHs intercalated with hydroxy-carboxylate anions (*e.g.*, D,L-lactate) spontaneously exfoliate in distilled water due to the osmotic swelling[80,81]. Lastly, the LDH exfoliation can also be achieved by charge reversal[82–84]. In the latter technique, multicharged anions are adsorbed onto the surface of LDH layers until their charge is reversed from positive to negative. Hence, to accurately describe the stability of LDH dispersions, understanding the interactions between charged surfaces and ions dissolved into an electrolyte is first required, *i.e.*, the Debye-Hükel model. Then, the approach must be extended to two charged surfaces that interact by electrostatic and van der Waals forces, *i.e.*, the Derjaguin, Landau, Verwey and Overbeek (DLVO) theory. Both the aforementioned topics are introduced in the next section.

Table 3.1. *LDH and solvent surface energies, Hansen parameters and boiling points. Cf. ref.* [73].

Material / Solvent	U^s **(mJ·m^{-2})**	δ_d **(MPa$^{1/2}$)**	δ_p **(MPa$^{1/2}$)**	δ_H **(MPa$^{1/2}$)**	**Boiling point (°C)**
LDHs	~86	~17.2	~10	~26.0	-
Formamide	88.0	17.2	19.0	19.0	210
Dimethyl sulfoxide	74.0	18.4	16.4	10.2	189
Diethylene glycol	77.7	17.0	12.0	20.7	245
Glycerol	93.4	17.4	12.1	29.3	182
Ethanol	53	15.8	8.8	19.4	78
Water	102.7	15.5	16.0	42.3	100

3.2. Interactions between charged surfaces: the physical meaning of zeta potential

According to the Debye-Hükel model (**Figure 3.1**), an electrically charged surface immersed into an electrolyte produces an electrostatic double layer due to the approaching of ions with opposite charge to the surface[85]. Hence, by the electroneutrality principle, the total charge balance is defined as

$$\sigma_0 + \sigma_{OHP} + \sigma_d = 0\,. \qquad (\mathbf{3.1})$$

Here σ_0 is the surface charge density, σ_{OHP} is the charge density at the outer Helmholtz plane (OHP, *i.e.*, the pane of nearest approach for ions without losing their solvation shell) and σ_d is the charge density of the diffuse layer of ions approaching the surface. In case of LDHs σ_0 results from three different contributions: the structural charge density (σ_{str}) arising from $M^{(III)}$ (*cf.* $(\mathbf{2.1})$),

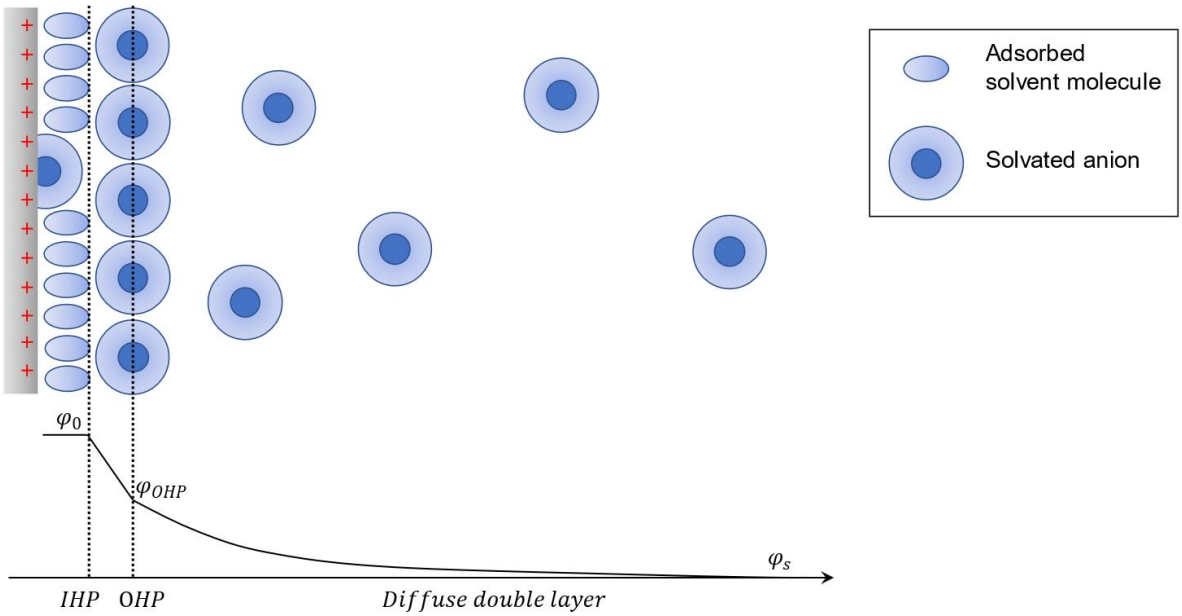

Figure 3.1. *Graphical representation of the Debye-Hükel model (not to scale).*

the proton charge density (σ_{H^+}) that results from the protonation or deprotonation of hydroxyl surface groups, and the charge density carried by anions and solvent molecules chemisorbed on the surface, *i.e.*, located at the inner Helmholtz plane (σ_{IHP}), hence

$$\sigma_0 = \sigma_{st} + \sigma_{H^+} + \sigma_{IHP} \,. \tag{3.2}$$

Since the OHP is located at a distance from the charged surface equal to half of the radius of solvated ions, all ions at the OHP can be assumed electrostatically bound to the surface and move with it[85]. Hence, the sum of the first two elements of $(\mathbf{3.1})$ can be considered as the effective charge density, σ_{eff}, that a solvated surface experiences into an electrolyte, thus

$$\sigma_{eff} = -\sigma_d \,. \tag{3.3}$$

The equation relating the charge density to the electric field ($\boldsymbol{E}$) is:

$$div\, \boldsymbol{E} = \frac{\sigma}{\varepsilon_0 \varepsilon_r} \,. \tag{3.4}$$

In which ε_0 is the absolute permittivity of vacuum and ε_r is the relative permittivity of the medium. The Galvani potential (φ) in an electrolyte is defined as the negative gradient of $\boldsymbol{E}$. Hence,

$$\boldsymbol{E} = -\boldsymbol{grad}\, \varphi \equiv -\boldsymbol{i}\frac{\partial \varphi}{\partial x} - \boldsymbol{j}\frac{\partial \varphi}{\partial y} - \boldsymbol{k}\frac{\partial \varphi}{\partial z} \,, \tag{3.5}$$

where $\boldsymbol{i}$, $\boldsymbol{j}$ and $\boldsymbol{k}$ are unitary vectors along x, y and z, respectively. By combining $(\mathbf{3.4})$ with $(\mathbf{3.5})$, it follows that

$$\frac{\sigma}{\varepsilon_0 \varepsilon_r} = div\, \boldsymbol{grad}\, \varphi \equiv \frac{\partial^2 \varphi}{\partial x^2} + \frac{\partial^2 \varphi}{\partial y^2} + \frac{\partial^2 \varphi}{\partial z^2} \tag{3.6}$$

However, in the case of planar surfaces, the number of coordinates in $(\mathbf{3.6})$ is reduced to one, *i.e.*, the distance from the surface, resulting into:

$$\frac{\partial^2 \varphi}{\partial x^2} = -\frac{\sigma(x)}{\varepsilon_0 \varepsilon_r} \,. \tag{3.7}$$

Since ions within the OHP are located from the surface at a distance that is half of their solvation shell ($a/2$), the double layer formed by σ_0 and σ_{OHP} can be considered as a planar plate capacitor, implying that:

$$\frac{\partial^2 \varphi}{\partial x^2} = 0 \tag{3.8}$$

$$\downarrow$$

$$\frac{\partial \varphi}{\partial x} = constant \tag{3.9}$$

$$\downarrow$$

$$\varphi(x) = \varphi_0 - 2\frac{\varphi_0 - \varphi_{OHP}}{a} x \,. \tag{3.10}$$

In which φ_0 and φ_{OHP} are the Galvani potential generated by σ_0 and σ_{OHP}, whereas a is the diameter of the solvation shell of ions. On the contrary, the potential in the diffuse double layer (Goüy-Chapman model)[85] depends on the Boltzmann distribution[i] as follows:

$$n_i = n_{i,0} \exp\left[-\frac{Z_i e \cdot \varphi(x)}{k_B T}\right]. \tag{3.11}$$

In which n_i is the local number per unit volume of i ions with $Z_i e$ charge, $n_{i,0}$ is the number of i ions per unit volume in the bulk electrolyte, T the absolute temperature and k_B the Boltzmann constant. By rewriting $(\mathbf{3.11})$ with respect to the distance (ξ) from the OHP, it follows that

$$n_i = n_{i,0} \exp\left[-\frac{Z_i e \cdot (\varphi(\xi) - \varphi_s)}{k_B T}\right], \tag{3.12}$$

in which $\xi = x - a/2$ and φ_s the Galvani potential in the bulk electrolyte. By considering an imaginary plane at a distance ξ, its charge density depends on the summatory of the local number of all ionic species multiplied by their charge, hence:

$$\sigma(\xi) = \sum_i [Z_i e \cdot n_i(\xi)] = \sum_i \left\{ Z_i e \cdot n_{i,0} \exp\left[-\frac{Z_i e \cdot (\varphi(\xi) - \varphi_s)}{k_B T}\right]\right\} . \tag{3.13}$$

By combining $(\mathbf{3.7})$ with $(\mathbf{3.13})$ it follows that:

$$\frac{\partial^2 \varphi}{\partial x^2} = -\sum_i \left\{ \frac{Z_i e \cdot n_{i,0}}{\varepsilon_0 \varepsilon_r} \exp\left[-\frac{Z_i e \cdot (\varphi(\xi) - \varphi_s)}{k_B T}\right]\right\} . \tag{3.14}$$

In dilute electrolytes, the solution to $(\mathbf{3.14})$ can be approximated with its Taylor series up to the second term (*i.e.*, $\exp(x) \approx 1 - x$ for $x \ll 1$)[ii], leading to:

[i] Notice than the $z_i e \cdot \varphi(x)$ in $(\mathbf{3.11})$ is the electrostatic potential energy.

[ii] Notice that, by approximating $(\mathbf{3.14})$ with its Taylor series, the first term $\sum_i \frac{Z_i e \cdot n_{i,0}}{\varepsilon_0 \varepsilon_r} = 0$.

$$\frac{\partial^2 \varphi}{\partial \xi^2} = \kappa^2(\varphi(\xi) - \varphi_s)\,. \qquad (\mathbf{3.15})$$

Here κ^{-1} is the Debye length, defined as:

$$\kappa^2 = \frac{2e^2 N_A \rho_s m_0}{\varepsilon_0 \varepsilon_r k_B T} \boldsymbol{I}\,. \qquad (\mathbf{3.16})$$

In which N_A is the Avogadro's number, ρ_s the density of the solvent and m_0 the standard molality (expressed in mol·kg^{-1}). $\boldsymbol{I}$ is the ionic strength, and it is defined as:

$$\boldsymbol{I} = \frac{1}{2}\sum_i \left(Z_i^2 \frac{m_i}{m_0}\right)\,, \qquad (\mathbf{3.17})$$

in which m_i is the molality of the i^{th} ion in the bulk electrolyte. The physical meaning of κ^{-1} represents the distance at which φ_{OHP} is reduced by a factor of e^{-1} (Neper's number, not to be confused with electric charge). *E.g.*, in dilute aqueous electrolytes at 25°C ($\mathbf{3.16}$) yields:

$$\kappa^{-1} = \frac{3.046 \cdot 10^{-10}}{\sqrt{I}}\,. \qquad (\mathbf{3.18})$$

Therefore, κ^{-1} measures tens of nanometres at 10^{-4} M $NaCl$ concentration but it drops below 1 nm at 0.1 M $NaCl$ concentration.

By solving ($\mathbf{3.15}$) it follows that

$$\varphi(\xi) - \varphi_s = constant \cdot \exp(-\kappa\xi)\,, \qquad (\mathbf{3.19})$$

then, by integrating ($\mathbf{3.19}$) from $\xi = 0$ to $\xi = \infty$ yields:

$$\varphi(\xi) - \varphi_s = (\varphi_{OHP} - \varphi_s) \cdot \exp(-\kappa\xi)\,. \qquad (\mathbf{3.20})$$

By placing $\xi = 0$, ($\mathbf{3.20}$) yields the Galvani potential difference between the OHP and the bulk electrolyte. This Galvani potential difference is commonly referred to as zeta potential (ζ)[i], *i.e.*,

$$\zeta = \varphi_{OHP} - \varphi_s\,. \qquad (\mathbf{3.21})$$

Hence, ζ is the coefficient before the exponential decay of the Galvani potential due to the diffuse double layer, *i.e.*,

$$\varphi(\xi) - \varphi_s = \zeta \cdot \exp(-\kappa\xi)\,. \qquad (\mathbf{3.22})$$

To this point, the nature of the repulsive force between two planar, equally charged surfaces immersed in an electrolyte, at a distance of $2l$, derives from the overlapping of two diffuse double layers generated by the σ_{OHP} of both surfaces according to ($\mathbf{3.12}$). The local number of ions at a distance l, *i.e.*, half the gap, is defined as[ii]:

$$\sum_i n_i = \sum_i n_{i,0} \cdot \exp\left[-\frac{Z_i e \cdot 2(\varphi(\xi) - \varphi_s)}{k_B T}\right]. \qquad (\mathbf{3.23})$$

[i] Experimentally ζ is measured at a distance of $a/2$ outside the OHP, *i.e.*, at a distance equal to half the radius of solvated ions. However, for dilute solutions the potential drop across that distance is negligible.

[ii] Note that the exponential term of ($\mathbf{3.23}$) is twice that of ($\mathbf{3.12}$), due to the overlapping of two diffuse double layers.

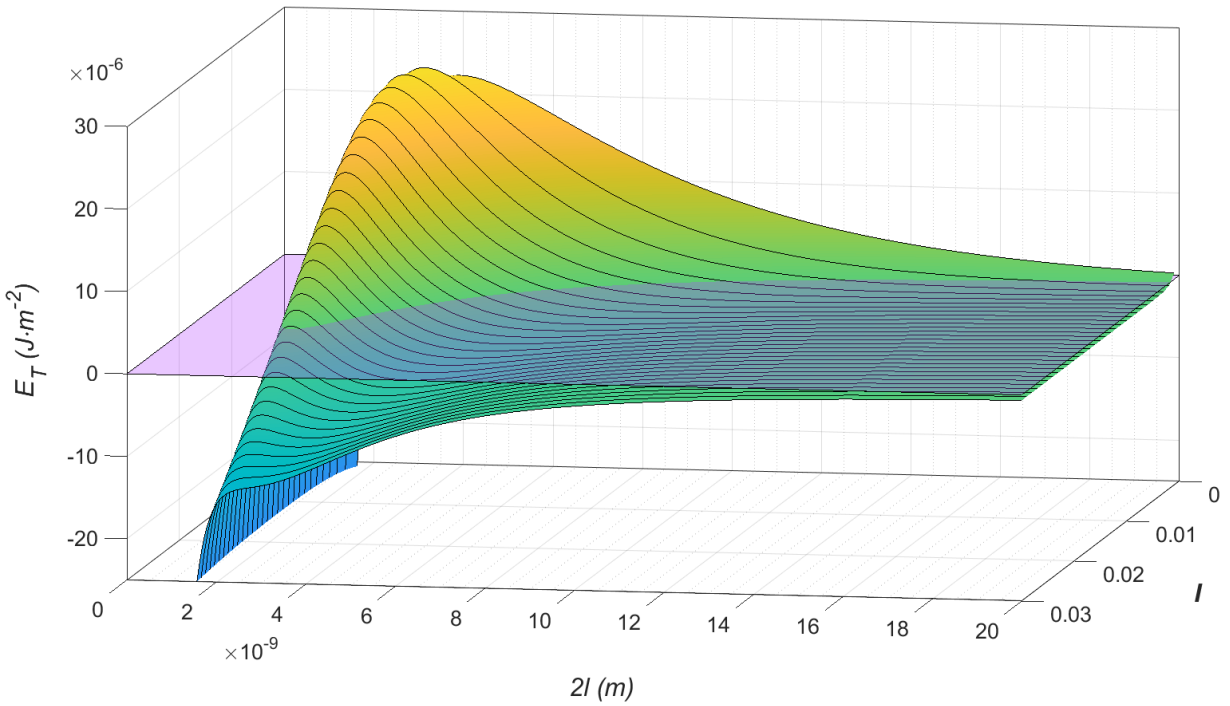

Figure 3.2. *Graphical representation of the DLVO theory* $(\mathbf{3.32})$ *at fixed* ζ *of ±50 mV and* A_H *fixed at* $1{\cdot}10^{-20}$ *J.*

According to the van't Hoff equation, the difference in ions concentration (Δc_i), in the $2l$ gap with respect to the bulk electrolyte produces an osmotic pressure (Π) as follows:

$$\Pi = RT\sum_i \Delta c_i = k_B T\sum_i \Delta n_i\,, \qquad (\mathbf{3.24})$$

in which $\Delta n_i = n_i - n_{i,0}$, and R is the gas constant ($R = N_A k_B$). It follows from $(\mathbf{3.23})$ that the difference in the local number of ions at a distance l with respect to the bulk electrolyte is defined as:

$$\sum_i \Delta n_i = \sum_i n_i - \sum_i n_{i,0} = \sum_i n_{i,0}\cdot\left\{\exp\left[-\frac{Z_i e\cdot 2(\varphi(\xi)-\varphi_s)}{k_B T}\right]-1\right\}. \qquad (\mathbf{3.25})$$

At this point, by following an analogous procedure to $(\mathbf{3.14})$, $(\mathbf{3.25})$ can be approximated with its Taylor series up to the third term, yielding[i]:

$$\sum_i \Delta n_i = -\frac{1}{2}\sum_i n_{i,0}\cdot\left[\frac{Z_i e\cdot 2(\varphi(\xi)-\varphi_s)}{k_B T}\right]^2 = -\left(\frac{2e^2}{k_B^2 T^2}\sum_i Z_i^2 n_{i,0}\right)\cdot(\varphi(\xi)-\varphi_s)^2\,. \qquad (\mathbf{3.26})$$

By combining $(\mathbf{3.24})$ with $(\mathbf{3.26})$, it results that:

$$\Pi = -\left(\frac{2e^2}{k_B T}\sum_i Z_i^2 n_{i,0}\right)\cdot(\varphi(\xi)-\varphi_s)^2\,, \qquad (\mathbf{3.27})$$

then, the rearrangement of $(\mathbf{3.27})$ according to $(\mathbf{3.16})$, $(\mathbf{3.17})$ and $(\mathbf{3.22})$ yields:

[i] Note that the second term in the Taylor series of $(\mathbf{3.25})$ is $\frac{2(\varphi(\xi)-\varphi_s)}{k_B T}\cdot\sum_i n_{i,0}Z_i e = 0$, since the overall charge of ions cancel out, *i.e.*, $\sum_i n_{i,0}Z_i = 0$.

$$\Pi = -\frac{1}{2}\varepsilon_0\varepsilon_r\kappa^2\zeta^2 \cdot \exp(-2\kappa\xi) \ . \qquad (\mathbf{3.28})$$

Hence, the energy per unit area[i] due to the osmotic pressure results from two times the integration of $(\mathbf{3.28})$ from $\xi = \infty$ to $\xi = l$ as follows:

$$E_\Pi = -\varepsilon_0\varepsilon_r\kappa^2\zeta^2 \int_\infty^l \exp(-2\kappa\xi)\, dl \qquad (\mathbf{3.29})$$

$$\downarrow$$

$$E_\Pi = \frac{1}{2}\varepsilon_0\varepsilon_r\kappa\zeta^2 \exp(-2\kappa l) \ . \qquad (\mathbf{3.30})$$

On the contrary, the energy per unit area resulting from the attraction of two parallel surfaces, placed at a distance of $2l$, due to van der Waals forces is expressed as:

$$E_{VdW} = -\frac{A_H}{12\pi}\frac{1}{(2l)^2} \qquad (\mathbf{3.31})$$

in which A_H is the Hamaker constant that assumes values between $7{\cdot}10^{-22}$ and $3{\cdot}10^{-19}$ J, with $1{\cdot}10^{-20}$ J as average value[86]. The DLVO theory describes the interaction between electrically charged solid particles dispersed into a liquid medium. In the case of charged planar plate-like particles, the total energy per unit area (E_T) as a function of the distance ($2l$) can be merely described as the sum of $(\mathbf{3.30})$ and $(\mathbf{3.31})$, *i.e.*,

$$E_T = \frac{1}{2}\varepsilon_0\varepsilon_r\kappa\zeta^2 \exp(-2\kappa l) - \frac{A_H}{12\pi}\frac{1}{(2l)^2} \ . \qquad (\mathbf{3.32})$$

The magnitude of $E_T(2l)$ is illustrated at fixed ζ of ±50 mV and variable $\boldsymbol{I}$ in **Figure 3.2**[ii]. At $\boldsymbol{I}$ approaching to zero[iii], $E_T(2l)$ presents a positive global maximum at $2l$ values of approximately 3 nm. The global maximum represents the energy barrier that charged nanosheets, dispersed into an electrolyte, must overcome in order to coagulate (*i.e.*, the global minimum at $2l$ approaching to zero). At $\boldsymbol{I}$ values of 0.01 (*e.g.*, 10 mM $NaCl$), $E_T(2l)$ still presents a positive global maximum, however at $2l$ about 5 nm, a local minimum does occur. The local minimum represents the phenomenon of flocculation. In a flocculated precipitate, the particles (or nanosheets) are trapped into the local minimum, hence they stay at a fixed distance from each other without coagulating. Flocculation is a reversible phenomenon since the precipitate can be suspended again for a brief period of time (hours or days). By increasing further $\boldsymbol{I}$, the magnitude of the global maximum decreases until it reaches negative values, at this point the irreversible coagulation of the particles is favoured. For the sake of completeness, $E_T(\zeta)$ and $E_T(A_H)$ are not graphically represented since they are quadratic and linear, respectively.

[i] The units of E_Π in $(\mathbf{3.30})$, but also of E_{VdW} in $(\mathbf{3.31})$ are J/m^2.
[ii] $\boldsymbol{I} \propto \kappa^2$ according to $(\mathbf{3.16})$.
[iii] The minimum $\boldsymbol{I}$ for aqueous electrolytes is $1.004{\cdot}10^{-7}$ at 25°C due water self-dissociation[85]. In a general case, the minimum $\boldsymbol{I}$ in a protonic solvent is equal to the square root of its self-dissociation constant.

3.3. Dispersion of layered double hydroxides in ethanol

I decided to develop a way to exfoliate LDHs in ethanol, since it constitutes an unharmful solvent with a low boiling point, *i.e.*, 78°C[i]. My idea is covering LDH layers with a surfactant, similarly to how amphiphilic surfactants are used to exfoliate LDHs into nonpolar or weakly polar solvents[59]. The surfactant I have chosen is sodium acetate, for its similarity with ethanol, and its capability to form hydrogen bonds through its carboxylic group[78]. As a starting point, I have used sodium acetate to stabilize few-layer nanosheets of carbonate-intercalated NiFe-LDH dispersed in ethanol. From now I will refer to the aforementioned dispersion as NiFe-CO_3-1. To achieve this, I have first synthetized the carbonate intercalated NiFe-LDH with the "urea hydrolysis" method[87], and then I exposed the synthetized product to a sodium acetate aqueous solution. Then, by performing subsequential washings with ethanol, the excess of sodium acetate and water is removed, and the NiFe-LDH starts to disperse, yielding NiFe-CO_3-1. The dispersion process can be easily monitored, since the ethanol turns yellow due to the dispersed NiFe-LDH nanosheets. A more accurate monitoring of the dispersion process is achieved by electronic spectroscopy (UV-Vis-NIR) as shown in **Figure 3.3**. In fact, as the washing procedure with ethanol goes on, the absorbance at 350 nm of the dispersion increases up to saturation[ii]. The concentration of NiFe-CO_3-1 at saturation is 0.16 g·L^{-1}, while the dispersed particles are hexagonal nanosheets with an expected lateral size, $\langle L \rangle$, of 242 nm, as illustrated in **Figure 3.4a**. The stability of NiFe-CO_3-1 lasted for more than six months, and this stability cannot be explained neither by the close matching between the surface energies of LDH and ethanol, nor by the close matching between Hansen parameters (*cf.* **Table 3.1**). Hence, the value of $|\zeta|$ provides insights on the mechanism exploited by acetate anions into stabilizing NiFe-CO_3-1. More in detail, a ζ of tens of mV indicates that acetate anions dissolve into the ethanol leaving behind a charged LDH surface. In this case,

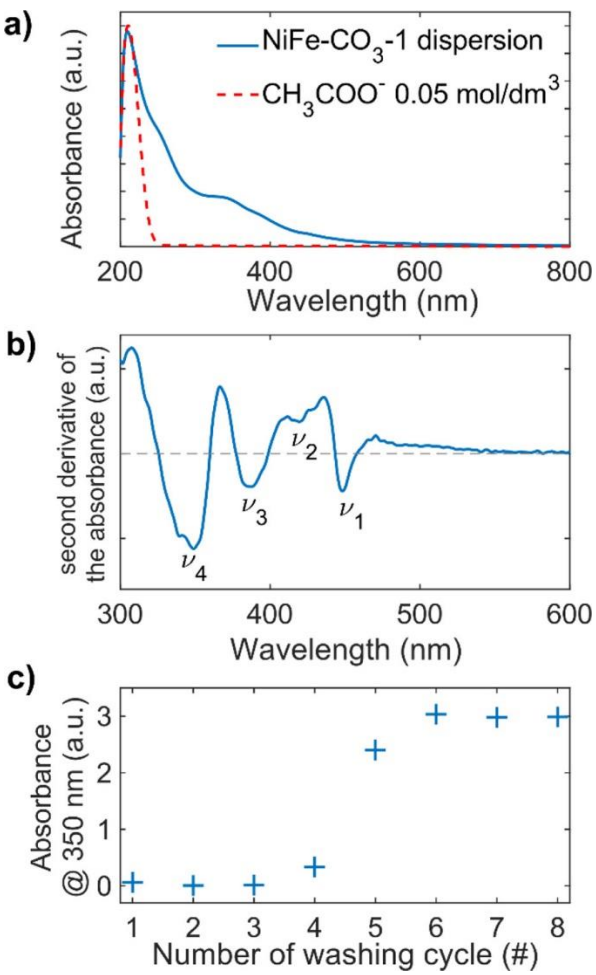

Figure 3.3. *a) Electronic spectra of NiFe-LDH nanosheets dispersed in ethanol compared with an ethanol sodium acetate solution. b) Second derivative electronic spectrum of NiFe-LDH nanosheets dispersed in ethanol, c) Absorbance measured @ 350 nm of supernatants collected during washing cycles. Reprinted with permission from Piccinni, M.; Bellani, S.; Bianca, G.; Bonaccorso, F. Nickel-Iron Layered Double Hydroxide Dispersions in Ethanol Stabilized by Acetate Anions. Inorg Chem* ***2022****, 61 (11), 4598–4608. Copyright 2022 American Chemical Society.*

[i] Refer to data sheets from the supplier (Sigma-Aldrich).
[ii] The absorbance spectrum of transition metal based LDHs is described in Chapter 6.

the dispersion would be stabilized by osmotic swelling according to $(\mathbf{3.32})$. On the contrary, a ζ close to zero indicates that acetate anions are bound to the LDH surface at the IHP, acting as a surfactant. The measured ζ for NiFe-CO_3-1 is +1.68 mV, while the same carbonate intercalated NiFe-LDH yielded a ζ of +43.2 mV when suspended in water. However, the water suspension of carbonate-intercalated NiFe-LDH flocculated completely in one day. Despite multiple, subsequential washings during the dispersion process, the reduction of ζ in ethanol, compared to water, suggests that acetate anions are bound to the LDH surface at the Helmholtz planes, effectively neutralizing the σ_0 and acting as a surfactant. Furthermore, I have decided to investigate the effect of acetate anions when introduced during the LDH synthesis. To achieve this, I used nickel acetate as the source of nickel in the synthesis of carbonate-intercalated NiFe-LDH. Then, I have dispersed the obtained product in ethanol by following the same procedure adopted for NiFe-CO_3-1. The obtained ethanol dispersion, namely NiFe-CO_3-2, saturated at a concentration of 0.22 g·L^{-1} with a ζ value of +1.59 mV. Moreover, the effect of acetate in the synthesis environment led to a larger $\langle L \rangle$ of 416 for nanosheets in NiFe-CO_3-2, as illustrated in **Figure 3.4b**. I ascribe this increased $\langle L \rangle$ to the absorption of acetate anions on the surface of LDH nanosheets while they are still forming during the synthesis, thus favouring the lateral growth of nanosheets. Eventually, the presence of acetate does not significantly influence the iron content in NiFe-LDHs, since NiFe-CO_3-1 and NiFe-CO_3-2 showed a 19.20% and 20.29% of iron content, respectively.

Since acetate anions have been proven to be effective stabilizers for ethanol dispersion of carbonate intercalated NiFe-LDHs, I have decided to replace carbonate with citrate as the interlayer anion in NiFe-LDH. The choice of citrate has been driven by three main factors. Firstly, citrate is a tricarboxylic anion, hence it can bind on the surface in a similar fashion as acetate does[78]. However, citrate possesses three negative charges instead of one; hence, I expect it is able to perform a charge reversal of the LDH surface. For the sake of clarity, a charge reversal happens when $|\pm(\sigma_{st} + \sigma_{H^+})| < |\mp(\sigma_{IHP} + \sigma_{OHP})|$. Secondly, citrate-intercalated MgAl-, NiAl- and ZnAl-LDHs have been reported in literature[69,88], and they are prone to osmotic swelling in distilled water[77,80,81], meaning that an exfoliation down to single layer is feasible according to $(\mathbf{3.32})$. Thirdly, citrate forms coordination compounds with iron[89,90], preventing the formation of unwanted ferric oxide phases that may occur during the iron-based LDH synthesis[91]. Unfortunately, I could not rely on the ammonia produced during urea hydrolysis for the precipitation of NiFe-LDH, because the hydrolysis of urea also produces carbonates as follows:

$$OC(NH_2)_2 + 2H_2O \xrightarrow{T>60°C} CO_3^{2-} + 2NH_4^+ \qquad (\mathbf{3.33a})$$

$$CO_3^{2-} + 2NH_4^+ \rightarrow CO_2 \uparrow + 2NH_3 \qquad (\mathbf{3.33b})$$

Hence, I had to use $NaOH$ to provide the alkaline environment for the LDH formation. The investigation on the formation mechanism of citrate intercalated LDHs is discussed in Chapter 4. The freshly formed citrate-intercalated NiFe-LDH spontaneously disperse in water forming gels with a LDH concentration up to 6.7 g·L^{-1} and a pH near to 8 due to the partial protonation of citrate anions as follows:

$$HCit^{3-} + H_2O \rightleftharpoons H_2Cit^{2-} + OH^- \qquad (\mathbf{3.34})$$

where Cit^{4-} is $C_6H_4O_7^{4-}$. For the sake of clarity, in this thesis I will always consider citric acid as tetraprotic, since its hydroxylic proton is exchanged in strong alkali or as a result of coordination compounds[92]. When dispersed in water, citrate-intercalated NiFe-LDH showed a ζ of -45.3 mV, indicating chat citrate anions are able to perform a charge reversal of the LDH surface. By performing the acetate treatment and subsequent dispersion of the citrate-intercalated NiFe-LDH in ethanol, the obtained dispersion, namely NiFe-Cit, reached saturation at 0.16 g·L^{-1}, yielding a ζ of -3.94 mV. This time, the reduction in $|\zeta|$ is also indicative that acetate anions not only bind on the LDH surface, but also compete with citrate for the same binding sites. The dispersed NiFe-Cit nanosheets are shown in **Figure 3.4c**. The nanosheets are round shaped with $\langle L \rangle$ of 208 nm, while their thickness measured with atomic force microscopy (AFM) is 1.2 nm. This value matches the basal spacing of 1.23 nm in citrate-intercalated LDHs[i]. Thus, I can state that citrate-intercalated NiFe-LDH can be exfoliated down to single layer in ethanol, by pre-treating them with acetate anions as a surfactant.

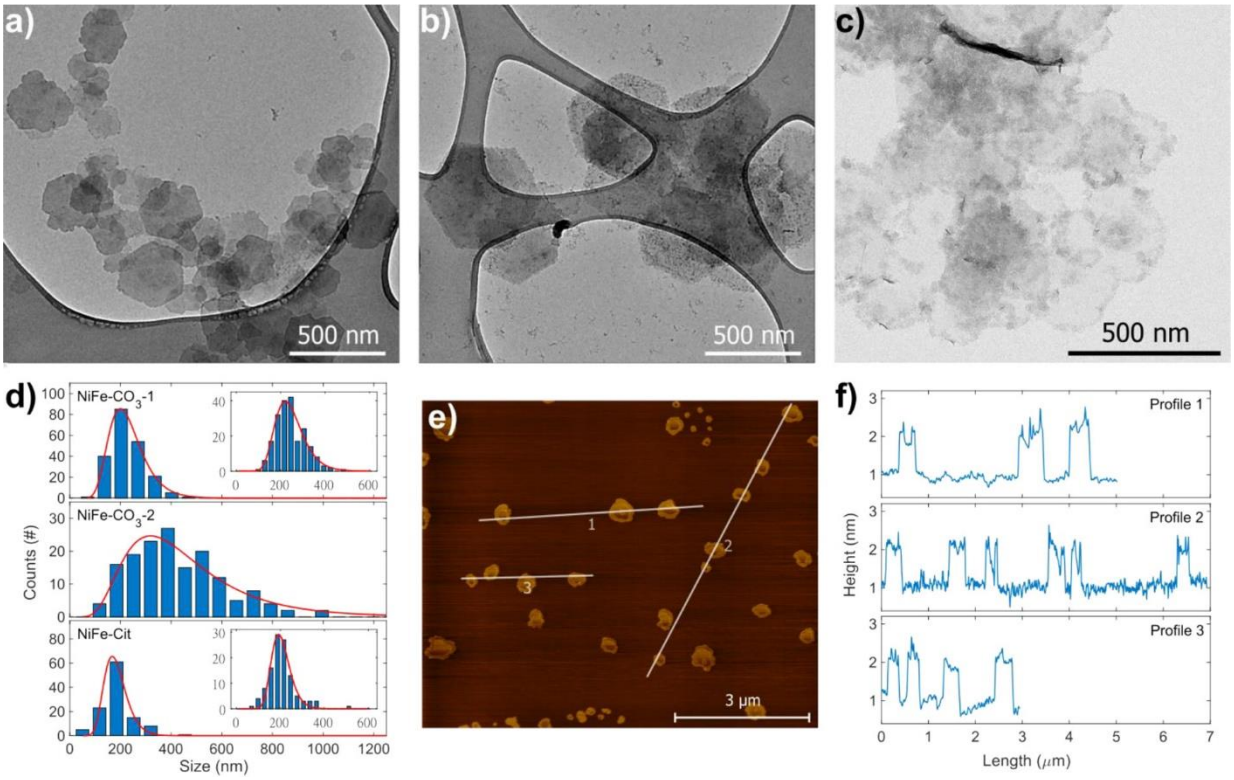

Figure 3.4. *Bright field transmission electron microscopy images of a) NiFe-CO3–1 nanosheets, b) NiFe-CO3–2 nanosheets and c) NiFe-Cit nanosheets. d) Size histograms of NiFe–LDH particles fitted by a lognormal distribution (red line). e) Atomic force microscopy image, and f) the corresponding height profiles of NiFe-Cit nanosheets. Reprinted with permission from Piccinni, M.; Bellani, S.; Bianca, G.; Bonaccorso, F. Nickel-Iron Layered Double Hydroxide Dispersions in Ethanol Stabilized by Acetate Anions. Inorg Chem* ***2022****, 61 (11), 4598–4608. Copyright 2022 American Chemical Society.*

[i] The basal spacing is the thickness of one layer plus the thickness of one interlayer space. The basal spacing is obtained in a straightforward manner from the X-ray diffraction patterns and is described in detail in Chapter 2. Check **Table 9.2** in Appendix 9.1 for LDHs crystallographic data.

4. Electrocatalytic properties of LDHs

The transition to a carbon neutral energy infostructure, in the next decades, requires the development of energy storage technologies able to make up for the intermittence of renewable energy sources like wind and solar. To this point the production of molecular hydrogen from water electrolysis (or water splitting) is an appealing energy storage solution, provided that the electricity from the process originate from renewable energy sources. Moreover, molecular hydrogen can be recombined with atmospheric oxygen in fuel cells yielding electricity, or directly burned as fuel. However, the main obstacle to the development of an efficient electrolysis process is the oxygen evolution reaction (OER) happening at the anode during the water electrolysis process. In fact, the OER is a complex reaction involving four electron transfers coupled with four proton releases also including the formation of the double bond in the dioxygen molecule. For this reason, are required overpotentials of hundreds of millivolts to perform the water electrolysis at feasible reaction rate. To this point, the choice of a performant catalyst toward the OER is pivotal for the development of a carbon neutral society. Recently, oxides and hydroxides based on the iron group elements (Fe, Co and Ni) are being widely studied as catalyst for the OER, since the aforenamed materials are earth abundant, cheap, easy to prepare and stable under the OER conditions[58–62]. For this reason, I decided to investigate how the dispersion process in ethanol influences the electrocatalytic properties of NiFe-LDH nanosheets described in Chapter 3. Hence, I fabricated the NiFe-LDH electrodes by spraying the LDH ethanol dispersions onto graphite paper heated at 100°C. Here, the low boing point of ethanol is pivotal to ensure a straightforward spraying process. In fact, the ethanol immediately evaporates in contact with the hot graphite paper, allowing a fine control of the mass loading to 0.1 mg/cm^2. Then, I performed the evaluation of the electrocatalytic properties of NiFe-LDHs for the OER by polarization measurements in 0.1 M KOH electrolyte. For the sake of clarity, the solubility of LDHs in alkaline pH is negligible[93] and, as described in the previous chapter (*cf*. **Figure 3.2**), the dispersion of charged particles is unfavoured at 0.1 M KOH. Therefore, I assumed that NiFe-LDH electrodes are stable in the 0.1 M KOH electrolyte. To acquire reliable polarization curves of LDH electrodes, I decided to use the staircase voltammetry (SV), which is a derivative technique of the more popular cyclic voltammetry (CV). In fact, whereas in CV the potential-time waveform is continuous, the SV involves successive, equally spaced potential steps with a duration adequate to achieve a steady-state current. Then, the current is sampled at the end of each step. In this way, any capacitive contribution to the measured current, due to diffuse double layers, has decayed to a negligible value. Then, the analysis of polarization measurements provides insights on the performance and mechanism of the catalyst towards the OER. Thus, I also provide the physical meaning of the overpotential, the Tafel slope and the turnover frequency, which are used as benchmarks for the OER.

4.1. The physical meaning of the overpotential and Tafel slope

By considering a generic redox equilibrium

$$Ox + ne^- \rightleftharpoons Red\,, \qquad (\mathbf{4.1})$$

in which n electrons are exchanged, its kinetic constant rate (k) is defined as

$$k = k_0 \exp\left(-\frac{\Delta G^{\ddagger}}{k_B T}\right). \qquad (\mathbf{4.2})$$

Here $\Delta G^{\ddagger}$ is the free energy difference between the activated complex and the reactants, and k_0 describes the motion of nuclei in the activated complex, which is characteristic of the reaction considered[94]. Since the free energy of redox species in electrochemical processes depends on the potential applied to the electrode, *i.e.*, $E = \varphi_{electrode} - \varphi_s$, it follows that the current density due to the cathodic (forward) reaction in $(\mathbf{4.1})$ is defined as

$$j^{-}(E) = -nFc_{Ox}k_0^{-} \exp\left(-\frac{\beta nFE}{RT}\right), \qquad (\mathbf{4.3a})$$

whereas the current due to the anodic (backward) reaction is defined as

$$j^{+}(E) = nFc_{Red}k_0^{+} \exp\left[\frac{(1-\beta)nFE}{RT}\right]. \qquad (\mathbf{4.3b})$$

Here $j^{\pm}(E)$ is the current density measured at the electrode. The minus sign indicates the cathodic reaction in $(\mathbf{4.1})$, while the plus sign indicates the anodic reaction. k_0^{-} and k_0^{+} are the analogous to k_0 from $(\mathbf{4.2})$ for the cathodic and anodic reactions, respectively. F is the Faraday constant, while c_{Ox} and c_{Red} are the concentration of Ox and Red in the bulk electrolyte, respectively. β is the asymmetry parameter and reflects the degree of symmetry of the reaction path between Ox and Red. Usually, a β value of 0.5 is assumed[85]. Since $(\mathbf{4.3})$ equations describe two opposite reactions occurring at the same electrode, there is a rest potential, E_r, at which the current density at the electrode is equal to zero, *i.e.*,

$$j^{-}(E_r) + j^{+}(E_r) = 0. \qquad (\mathbf{4.4})$$

Hence, the E_r is straightforward from $(\mathbf{4.3})$ and $(\mathbf{4.4})$, yielding:

$$E_r = \frac{RT}{nF}\ln\frac{k_0^{+}}{k_0^{-}} + \frac{RT}{nF}\ln\frac{c_{Ox}}{c_{Red}}, \qquad (\mathbf{4.5})$$

which leads to the Nerst equation by defining the first addend of $(\mathbf{4.5})$ as the standard reduction potential (E_0), as follows

$$E_r = E_0 + \frac{RT}{nF}\ln\frac{c_{Ox}}{c_{Red}} \qquad (\mathbf{4.6})$$

Moreover, according to $(\mathbf{4.4})$ the exchange current, j_0, is defined as follows:

$$j_0 = |j^{-}(E_r)| = |j^{+}(E_r)|. \qquad (\mathbf{4.7})$$

More in detail:

$$-j_0 = j^{-}(E_r) = -nFc_{Ox}k_0^{-} \exp\left(-\frac{\beta nFE_r}{RT}\right) \qquad (\mathbf{4.8a})$$

and

$$+j_0 = j^{+}(E_r) = nFc_{Ox}k_0^{+} \exp\left[\frac{(1-\beta)nFE_r}{RT}\right]. \qquad (\mathbf{4.8b})$$

Now, given a redox reaction, the overpotential η can be defined as the difference between the potential applied at the electrode and the rest potential as follows:

$$\eta = E - E_r \,. \tag{4.9}$$

Hence, by combining (4.3), (4.8) and (4.9), the Butler-Volmer equation follows, *i.e.*,

$$j(\eta) = j_0 \left\{ \exp\left[\frac{(1-\beta)nF\eta}{RT}\right] - \exp\left(-\frac{\beta nF\eta}{RT}\right) \right\}. \tag{4.10}$$

Here, the first exponential term refers to the anodic reaction in (4.1), whereas the second exponential term refers to the cathodic reaction. Hence, the Butler-Volmer equation (4.10), provides the physical meaning of η. In fact, η represents the amount of potential "wasted" that must be provided to achieve the desired current density. If $|\eta| \gg RT/nF$ (*i.e.*, 25.7/n mV at 25°C), depending on the sign of η, one out of the two exponential terms in (4.10) can be neglected, leading to the Tafel equation, *i.e.*,

$$\eta = \left| \frac{RT}{\beta nF} \ln\left(\frac{j}{j_0}\right) \right|, \tag{4.11}$$

or, by changing the base of the logarithm:

$$\eta = \left| \ln(10) \cdot \frac{RT}{\beta nF} \log_{10}\left(\frac{j}{j_0}\right) \right|. \tag{4.12}$$

For the sake of simplicity, (4.12) is usually linearized as follows

$$\eta = q + m \cdot \log_{10}|j| \tag{4.13}$$

where q is the intercept on the ordinate axis and the angular coefficient m is referred to as Tafel slope. At 25°C the $|m|$ value is 118/n mV/dec, whereas the sign of m is negative for cathodic reactions and positive for anodic ones.

4.2. The oxygen evolution reaction in alkaline electrolytes

The oxygen evolution reaction (OER) is a complex reaction involving four electron transfers coupled with the release of four protons. Moreover, in alkaline environments, three different mechanisms are possible, depending on the catalyst surface chemistry. The first possible mechanism involves four identical electron transfers on different catalyst active sites (M^*) as follows:

$$M^* + OH^- \rightleftharpoons MOH + e^- \,. \tag{4.14}$$

Then, the four MOH intermediate species recombine by following three different paths: the oxide path

$$2MOH \rightleftharpoons MO + M^* + H_2O \tag{4.15a}$$

$$2MO \rightleftharpoons 2M^* + O_2 \,, \tag{4.15b}$$

the hydrogen peroxide path

$$2MOH \rightleftharpoons MH_2O_2 + M^* \tag{4.16a}$$

$$MOH + MH_2O_2 \rightleftharpoons MHO_2 + H_2O + M^* \tag{4.16b}$$

$$MHO_2 + MOH \rightleftharpoons O_2 + H_2O + 2M^* \tag{4.16c}$$

or the electrochemical metal peroxide path

$$2MOH \rightleftharpoons MO + H_2O + M^* \quad (\mathbf{4.17a})$$

$$MO + MOH \rightleftharpoons MHO_2 + M^* \quad (\mathbf{4.17b})$$

$$2MHO_2 \rightleftharpoons MO + O_2 + H_2O + M^* . \quad (\mathbf{4.17c})$$

The second possible mechanism involves two sequential electron transfers at different catalyst active site, *i.e.*,

$$M^* + OH^- \rightleftharpoons MOH + e^- \quad (\mathbf{4.14})$$

$$MOH + OH^- \rightleftharpoons MO + H_2O + e^- \quad (\mathbf{4.18})$$

and then the recombination of products follows as

$$2MO \rightleftharpoons 2M^* + O_2 \quad (\mathbf{4.15b})$$

The third possible mechanism involves all four sequential electron transfers happening on the same catalyst active site, as follows

$$M^* + OH^- \rightleftharpoons MOH + e^- \quad (\mathbf{4.14})$$

$$MOH + OH^- \rightleftharpoons MO + H_2O + e^- \quad (\mathbf{4.18})$$

$$MO + OH^- \rightleftharpoons MOOH + e^- \quad (\mathbf{4.19a})$$

$$MOOH + OH^- \rightleftharpoons MOO^- + H_2O \quad (\mathbf{4.19b})$$

$$MOO^- \rightleftharpoons M^* + O_2 + e^- . \quad (\mathbf{4.19c})$$

For the sake of clarity, the Tafel equation is strictly valid for single step reactions in which n electrons are simultaneously transferred[85,95]. For multistep reaction, like OER, the Tafel slope should be evaluated by a microkinetic analysis to also consider the role of intermediate species[85,95]. However, in multi-step reactions, it tuns out that the Tafel slope at steady-state conditions (*i.e.*, SV) reflects the number of electron transfers prior to the rate determining step (included)[85,95]. Hence, for the OER, ~120 mV/dec of Tafel slope is expected if ($\mathbf{4.14}$) is the rate determining step, ~60 mV/dec if ($\mathbf{4.18}$) is the rate determining step, ~40 mV/dec if ($\mathbf{4.19a}$) or ($\mathbf{4.19b}$) is the rate determining step, and ~30 mV/dec if ($\mathbf{4.19c}$) is the rate determining step.

4.3. Overpotential, Tafel analysis and turnover frequency

The overpotential at current densities of 10 mA·cm^{-2} (η_{10}), is considered the simplest benchmark of an electrocatalyst[96]. The η_{10} evaluation is straightforward from ($\mathbf{4.9}$) as follows

$$\eta_{10} = E_{(|j|=10\ mA\cdot cm^{-2})} - E_r . \quad (\mathbf{4.20})$$

Since for OER the standard reduction potential (E_0) is 1.229 V[29], by combining ($\mathbf{4.20}$) with the Nerst equation ($\mathbf{4.5}$), yields

$$\eta_{10} = E_{(|j|=10\ mA\cdot cm^{-2})} - (1.229 - 0.0592 \cdot pH) \quad (\mathbf{4.21})$$

at 25°C. The SV measurements indicate that the electrode fabricated from NiFe-CO_3-1 shows the highest electrocatalytic activity among the samples, yielding a η_{10} value of 0.38 V. The electrode

fabricated from NiFe-Cit yielded a η_{10} value of 0.43 V, whereas the electrode fabricated from NiFe-CO_3-2 yielded a η_{10} value of 0.54 V. The trend in η_{10} observed is consistent with the basicity of anions present in the LDH interlayer space[97]. In fact, the lower the LDH η_{10} toward OER (*i.e.*, higher performance), the lower the Lewis acidity (*i.e.*, higher pK_a) of conjugated acids of interlayer anions[97]. In this case, the following acid-base equilibria must be considered[92,94]:

$$HCO_3^- + H_2O \rightleftharpoons CO_3^{2-} + H_3O^+ \qquad pK_a = 10.33\,, \qquad (\mathbf{4.22a})$$

$$H_2Cit^{2-} + H_2O \rightleftharpoons HCit^{3-} + H_3O^+ \qquad pK_a = 6.40 \qquad (\mathbf{4.22b})$$

and

$$CH_3COOH + H_2O \rightleftharpoons CH_3COO^- + H_3O^+ \qquad pK_a = 4.76\,. \qquad (\mathbf{4.22c})$$

Hence, the reverse trend of measured η_{10} is reflected into the trend of pK_a values, *i.e.*, $HCO_3^- > H_2Cit^{2-} > CH_3COOH$. The explanation to this behaviour resides into the magnitude of Tafel slopes, which are displayed in **Figure 4.1**, indicating that a base-assisted deprotonation of OER intermediates is facilitated by Lewis bases[97]. More in detail, the electrode fabricated from NiFe-CO_3-1 showed a Tafel slope of 30 mV/dec suggesting that the rate determining step is the last electron transfer described in $(\mathbf{4.19c})$. On the contrary, the electrode fabricated from NiFe-Cit yielded a Tafel slope of 38 mV/dec. This value close to 40 mV/dec suggests that the rate determining step almost completely shifted from the last electron transfer to the deprotonation of the "$MOOH$" intermediate in $(\mathbf{4.19b})$. In fact, I argue that the lower pK_a of H_2Cit^{2-}, compared to the pK_a of HCO_3^-, implies that citrate is less effective than carbonate at deprotonating the "$MOOH$" intermediate, therefore making $(\mathbf{4.19b})$ the rate determining step. Furthermore, the electrode fabricated from NiFe-CO_3-2 yielded a Tafel slope of 47 mV/dec, placing it as intermediate between 40 mV/dec, which is expected if $(\mathbf{4.19a})$ or $(\mathbf{4.19b})$ is the rate determining step, and 60 mV/dec which is expected if $(\mathbf{4.18})$ is the rate determining step. The reason for the NiFe-CO_3-2 behaviour is that its nanosheets have been in contact with acetate anions since their formation in the reaction mixture, and it is reasonable to assume that acetates are incorporated into the LDH structure. Hence, the even lower pK_a of CH_3COOH, with respect to the previous two cases, suggests that an excessive quantity of acetate anions can also partially hinder the deprotonation of the "MOH" intermediate of the second electron transfer, *i.e.*, $(\mathbf{4.18})$. Lastly, I calculated the turnover frequency (TOF) of NiFe-LDHs toward the OER, *i.e.*, the

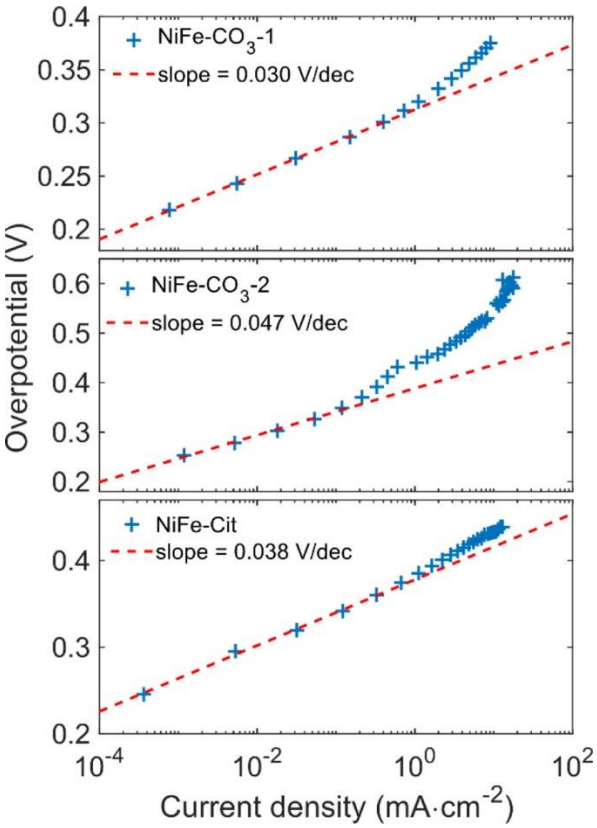

Figure 4.1. *Polarization curves and Tafel slopes, measured in 0.1 M KOH, of NiFe-LDH electrodes with 0.1 mg/cm² mass loading. Reprinted with permission from Piccinni, M.; Bellani, S.; Bianca, G.; Bonaccorso, F. Nickel-Iron Layered Double Hydroxide Dispersions in Ethanol Stabilized by Acetate Anions. Inorg Chem* ***2022****, 61 (11), 4598–4608. Copyright 2022 American Chemical Society.*

average number of reaction cycles performed per second by the active sites of the catalyst. Hence, for a redox reaction involving n electrons, by definition[i], the TOF is:

$$TOF = \frac{i}{n \cdot e} \cdot \frac{1}{N_{sites}}, \qquad (\mathbf{4.23})$$

in which i is the measured current ($i = j \cdot Area$) and N_{sites} is the number of active sites on the electrode. In case of Co- or Ni-based electrocatalysts, it is commonly accepted that N_{sites} can be estimated by the charge underlying the characteristic redox peaks of Co or Ni that precede the OER onset in CV measurements[96,98]. More in detail, in Ni-based electrocatalysts the oxidation from $Ni^{(II)}$ to $Ni^{(III,IV)}$ precedes the OER onset in CVs[99], *i.e.*,

$$Ni^{(II)} \rightleftharpoons Ni^{(III,IV)} + xe^{-} \qquad (\mathbf{4.24})$$

with a rest potential of ~0.49 V[94,100], and x that ranges from 1 to 1.7[100]. However, in the worst-case scenario, setting the x value to 1 means to overestimate the number of active sites, which implies an underestimation of the TOF with respect to its real value. Hence, $(\mathbf{4.23})$ can be rewritten as:

$$TOF = \frac{i}{n \cdot \Delta q_{Ni^{(II)} \rightleftharpoons Ni^{(III,IV)}}}, \qquad (\mathbf{4.25})$$

in which $\Delta q_{Ni^{(II)} \rightleftharpoons Ni^{(III,IV)}}$ is the charge underling the redox wave related to $(\mathbf{4.24})$. According to the Tafel equation, j, and therefore i, depends on the applied η. Consequently, also the TOF is η dependent. Hence, I report the TOF at a η of 300 mV extrapolated from the linear region of Tafel plots showed in **Figure 4.1**. Again, the electrocatalytic performance trend of NiFe-LDH based electrode is confirmed by the TOF, with NiFe-CO_3-1 yielding a TOF of 61.7 mHz, NiFe-Cit yielding a TOF of 13.8 mHz, and finally NiFe-CO_3-1 yielding a TOF of 3.53 mHz. Overall, the analysis on η_{10}, Tafel slopes and TOF indicate that the quantity of carboxylates contained in NiFe−LDHs must be minimized to avoid hindering the NiFe-LDHs electrocatalytic activity towards the OER.

[i] The first fraction in $(\mathbf{4.23})$ corresponds to the number of molecules produced per second.

5. Formation mechanism of citrate intercalated LDHs: the hydrolytic polymerization

In this chapter I discuss the formation mechanism of citrate intercalated LDH by the lens of potentiometric pH titrations and electronic spectroscopy investigations. As first, I decided to characterize the response to titration of each metal cation considered in the chapter (*i.e.*, Al^{3+}, Fe^{3+}, Ni^{2+}, and Zn^{2+}) and the effect of citrate on titration profiles. All titration profiles are reported as functions of $NaOH$ equivalents (Eq_{NaOH}). The effect of citrate on the titration profiles of Al^{3+}, Fe^{3+}, Ni^{2+}, and Zn^{2+} solutions are presented in **Figure 5.1**. As expected, in the absence of

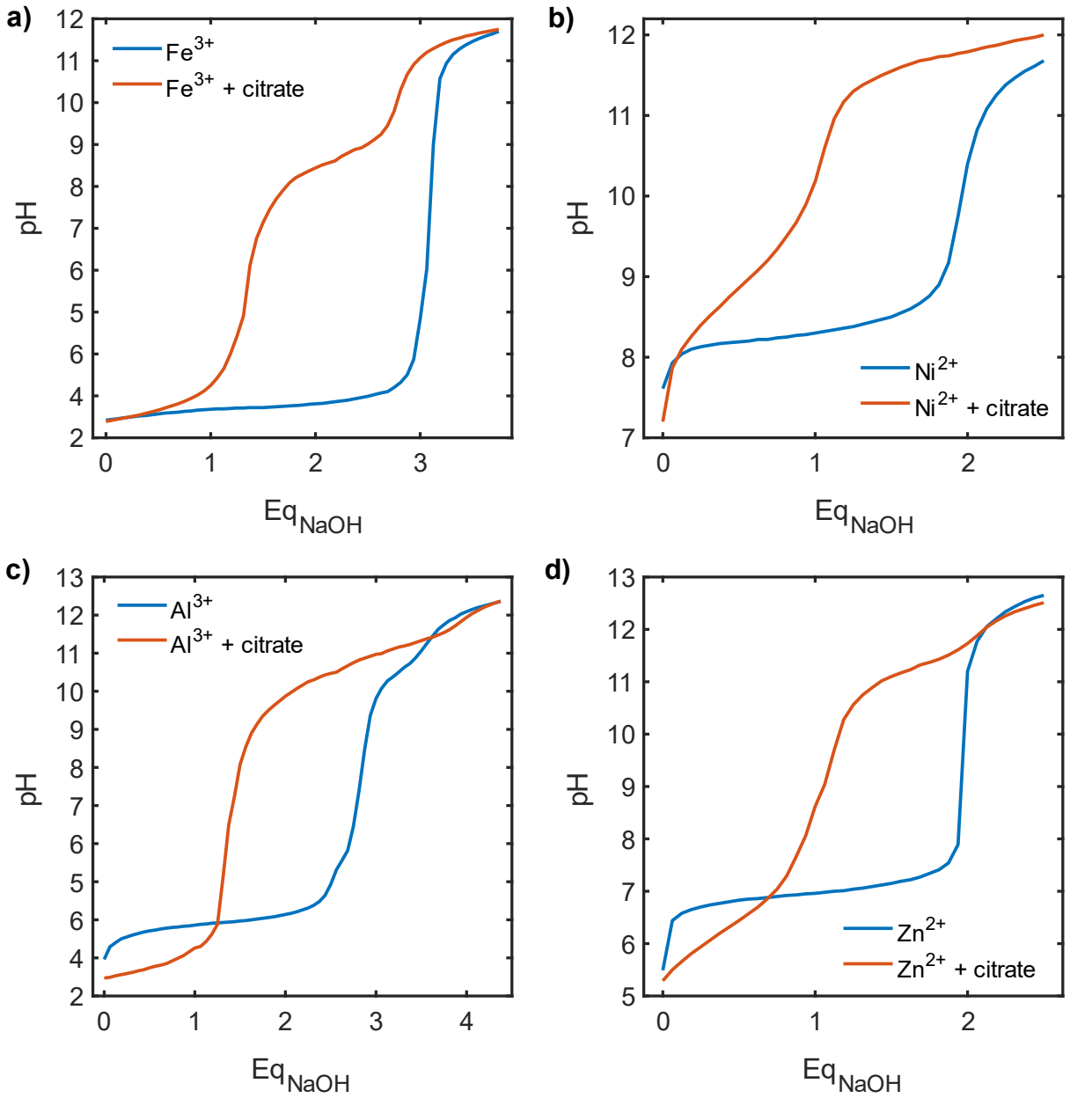

Figure 5.1. *Potentiometric titrations curves of Fe^{3+}, Ni^{2+}, Al^{3+}, and Zn^{2+} monometallic solutions with (orange curves) and without sodium citrate (cyan curves).*

citrate, the titration profiles (blue lines in **Figure 5.1**) only present a single wide buffer region. This buffer region ends at the equivalent point corresponding to the respective stoichiometric Eq_{NaOH}, indicating the precipitation of the related metal hydroxide. For the sake of completeness, the titration responses of several bimetallic solutions (in the absence of complexing agents) have been widely studied by J. Boclair et al.[93,101]. Summarizing, they reported that the titration of bimetallic solutions corresponds to consecutive titrations of monometallic solutions, with an intermediate region that varies depending on the affinity between the metals considered. Refer to Ref. [93,101] for details.

5.1. Titration of metal-citrate solutions

The presence of citrate in aqueous solutions leads to the formation of metal-citrate coordination compounds[102], whose nature depends on both the solution pH and the metal/citrate ratio[90,103]. I decided to set the initial conditions of titration as same as the synthesis conditions of the related LDHs. The titration profile of the iron-citrate solution (orange line in **Figure 5.1a**) is consistent with that obtained by T. G. Spiro et al. in 1967[90]. Here, the titration profile presents two equivalent points at 1.25 Eq_{NaOH} and 2.75 Eq_{NaOH}, respectively. The buffer region preceding the first equivalent point is related to the formation of mono-, bi- and tri-nuclear iron-citrate coordination compounds[103], whereas the second buffer region, located between 1.25 and 2.75 Eq_{NaOH}, is related to the hydrolytic polymerization of iron-citrate coordination compounds[89,90]. Then, the $NaOH$ saturation plateau follows the second equivalent point. During the whole titration, the colour of the Fe^{3+} solution shifted from light orange to dark orange/brown. This colour change is indicative of spin exchange interactions between neighbouring iron atoms, which will be described in detail in Section 5.3. Moreover, the solution remained clear of any precipitate for the duration of the whole titration, indicating the stability (at ambient temperature) of iron-citrate compounds. The titration of the nickel-citrate solution (orange line in **Figure 5.1b**) presents a single equivalent point at 1.25 Eq_{NaOH}. The equivalent point is preceded by a sloped region and followed by the $NaOH$ saturation plateau. To the best of my knowledge, no report has been published about the polymerization of nickel-citrate coordination compounds. On the contrary, several reports regarding the formation of polynuclear nickel-citrate compounds are available[102,104–106]. More in detail, binuclear ($[Ni_2(HCit)_2(H_2O)_4]^{2-}$) and tetranuclear ($[Ni_4(Cit)_3(OH)(H_2O)]^{5-}$) nickel-citrate compounds have been isolated, in the past, from acidic and alkaline solutions, respectively[102,104]. Moreover, it turns out to be an equilibrium, related to the environment pH, between the aforementioned nickel complexes[105]. More recently, M. Murrie et al. crystallized from alkaline solutions the tetramethylammonium salts of nickel-citrate complexes containing seven and twenty-one nickel atoms[106]: namely $[Ni_7(Cit)_6(H_2O)_2]^{10-}$ and $[Ni_{21}(Cit)_{12}(OH)_{10}(H_2O)_{10}]^{16-}$. Therefore, I interpret the sloped region from 0 to 1.25 Eq_{NaOH} in the titration profile of the nickel-citrate solution as the progressive increase in the number of nickel atoms in continuously growing nickel-citrate complexes. Interestingly, the Ni_{21} complex contains a cluster made of seven nickel atoms, in octahedral coordination with hydroxyl groups, arranged in a hexagonal close packed structure that resembles $Ni(OH)_2$[106]. It seems likely to me that coordination compounds such as the Ni_{21} or even larger ones can act as seeds for the formation of nickel-based hydroxides (LDHs included) in alkaline conditions. The titration curves of Al^{3+} and Zn^{2+} (**Figures 5.1c** and **5.1d**) are respective analogous to the one of Fe^{3+} or Ni^{2+}, with the main difference of the amphoteric nature of Al^{3+} and Zn^{2+}, which shifts the $NaOH$ saturation plateau to higher Eq_{NaOH} values[107].

5.2. Titration of bimetallic-citrate solutions

The titration profiles of bimetallic-citrate solutions have a shape resembling a convolution of the corresponding monometallic-citrate titration curves, as illustrated in **Figures 5.2a**, **5.2b** and **5.2c**. More in detail, the titration profiles of NiFe-, NiAl- and ZnAl-citrate solutions present a well-defined equivalent point around 0.4 Eq_{NaOH} followed by a sloped region. The titration profiles of NiAl- and ZnAl-citrate solutions also present a second equivalent point near 1.1 Eq_{NaOH}, whereas the

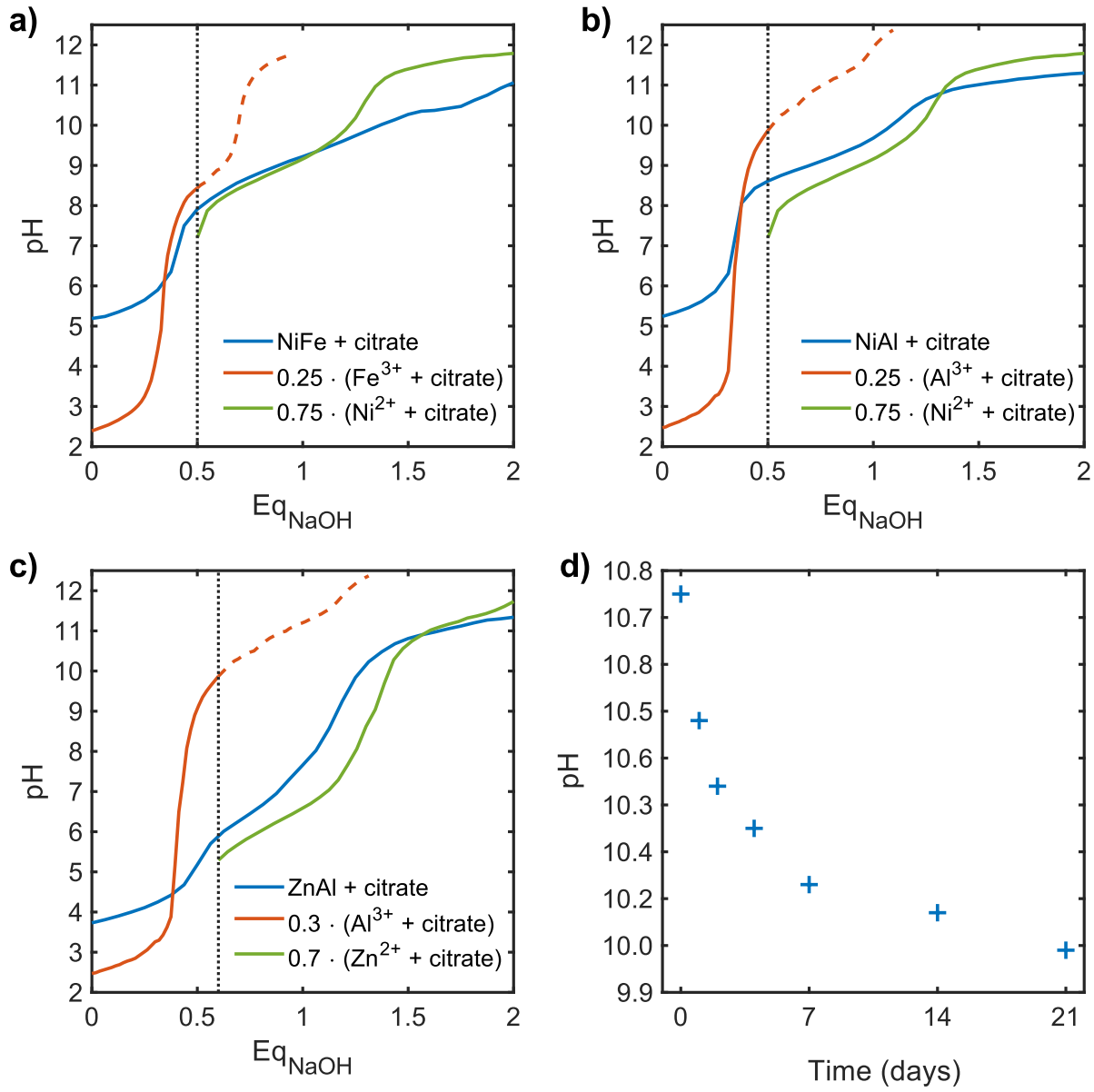

Figure 5.2. *a), b), c) Comparison between titrations of bimetallic citrate solutions and the corresponding monometallic-citrate solutions. Here the Eq_{NaOH} of monometallic-citrate titration curves have been normalized by the stoichiometric ratios of the corresponding metal. The dotted gray line indicates the value of Eq_{NaOH} that corresponds to twice the trivalent metal cation concentration in the bimetallic-citrate solutions. d) pH mesurements of the NiFe-citrate solution left ageing at ambient temperature for three weeks after the addition of 1.88 Eq_{NaOH}.*

titration profile of NiFe-citrate solution does not. I suspect that this anomalous behaviour of the NiFe-citrate solution is related to a cooperative tendency of nickel and iron forming mixed coordination compounds. In the case of NiAl- and ZnAl-citrate solutions, the formation of aluminate anions in alkaline environments[108] represents a competitive reaction to the formation of mixed aluminium coordination compounds with nickel or zinc. This statement is consistent with the 14.22% and 15.14% aluminium atomic ratio found in the NiAl-LDH and ZnAl-LDH, respectively. Those values are significantly lower than the 25% and 30% in moles of aluminium used in the corresponding reaction environment. Otherwise, the iron atomic ratio in the NiFe-LDH is 26.50%, whereas the molar iron content is 25% in its reaction environment. Nevertheless, I hypothesize that the formation mechanisms of NiFe-, NiAl- and ZnAl-LDHs, starting from metal-citrate solutions, follow analogous chemical pathways (*i.e.*, the hydrolysis of coordination compounds). Then, to confirm the slow LDH formation, I have monitored the pH evolution over 21 days in a nickel-iron-citrate solution left sealed at ambient temperature after adding 1.88 Eq_{NaOH} (*i.e.*, the Eq_{NaOH} amount used in the NiFe-LDH synthesis procedure). As shown in **Figure 5.2d**, the solution pH slowly decreases over time, which is consistent with the slow LDH formation. However, after three weeks at ambient temperature, the formation of the NiFe-LDH is far from being complete, since the solution pH is still ~10, whereas the same synthesis carried out at 90°C yields a pH of ~8 within three days.

5.3. Optical investigation on the LDH formation mechanism

The absorbance bands observed in LDH electronic spectra are related to two types of transitions. The first type of transitions is Ligand-to-Metal Charge Transfer (LMCT), which can be roughly described as the excitation of one electron from $2p$ orbitals of an oxygen atom to $3d$ orbitals of a neighbouring transition metal atom. The second type of transition is ascribable to the ligand field, and they are usually referred to as d-d transitions. The absorbance bands related to LMCT transitions are usually observed in the UV region of the electronic spectra (at wavelengths < 400 nm). The d-d transitions are described by the ligand field theory[29,109], whereas their absorbance bands can be observed in the whole spectral range (from UV to NIR). In overall, I have detected six and ten different absorbance bands in NiAl- and NiFe-LDH electronic spectra, respectively; their nature is discussed in detail in Chapter 6. For the sake of clarity, d-d transitions in LDHs are parity-forbidden by symmetry[29], whereas some of them involve states with different spin multiplicity, being also spin-forbbidden[29]. Therefore, d-d transitions are expected to be orders of magnitude less intense in comparison to the completely allowed LMCT transitions[29]. However, exchange interactions between neighbouring paramagnetic cations (*e.g.*, Cr^{3+}, Mn^{2+}, Fe^{3+} or Ni^{2+}) can not only lift the aforementioned restrictions, but also dramatically increase the absorbance related to spin-forbidden d-d transitions[110–118]. The magnetic exchange interactions between multiple paramagnetic ions are described by the Heisenberg Hamiltonian ($\boldsymbol{\mathcal{H}}_{ex}$) as follows:

$$\boldsymbol{\mathcal{H}}_{ex} = -2\sum_{i<j} J_{ij}\boldsymbol{S}_i \cdot \boldsymbol{S}_j \,. \qquad (\mathbf{5.1})$$

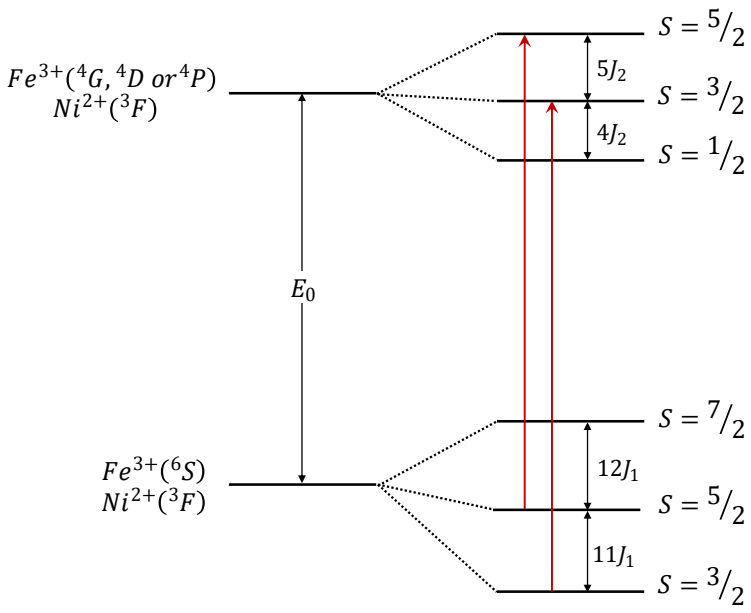

Figure 5.3. *Schematic representation of the spin exchange interaction in an Fe^{3+}-Ni^{2+} ion pair. E_0 represents the energy gap between the ground state and an exited state without accounting for the exchange interactions. J_1 and J_2 represent the exchange integrals of the Fe^{3+}-Ni^{2+} ion pair in its ground state and exited state, respectively. The energy levels splitting, and position are calculated according to* $(\mathbf{5.5})$*. The electronic transitions between states with the same S are represented by red arrows.*

In which $\boldsymbol{S}_i$ and $\boldsymbol{S}_j$ are the overall electronic spin vector of the i^{th} and j^{th} ion, respectively, whereas the exchange integral J_{ij} represents magnitude and type of interaction between each possible i-j ion pair. Conventionally, J_{ij} is assumed to be positive for ferromagnetic interactions and negative for anti-ferromagnetic interactions. Given any possible i-j ion pair, the total spin vector, $\boldsymbol{S}_{ij}$, can be expressed as:

$$\boldsymbol{S}_{ij}^2 = \left(\boldsymbol{S}_i + \boldsymbol{S}_j\right)^2 = \boldsymbol{S}_i^2 + \boldsymbol{S}_j^2 + 2\boldsymbol{S}_i \cdot \boldsymbol{S}_j \,. \tag{5.2}$$

whereas the modulus of the total spin vector (S_{ij}) can assume multiple values as follows:

$$S_{ij} = \left(S_i + S_j\right), \left(S_i + S_j - 1\right), \dots, \left|S_i - S_j\right| . \tag{5.3}$$

By combining $(\mathbf{5.1})$ with $(\mathbf{5.2})$, it follows that

$$\boldsymbol{\mathcal{H}}_{ex} = -\sum_{i<j} J_{ij}\left[\boldsymbol{S}_{ij}^2 - \left(\boldsymbol{S}_i^2 + \boldsymbol{S}_j^2\right)\right] . \tag{5.4}$$

Hence, the energy eigenstates obtained from $(\mathbf{5.4})$ are defined as

$$\begin{aligned} E(S) &= -\textstyle\sum_{i<j} J_{ij}\left(\langle \boldsymbol{S}_{ij}^2 \rangle - \langle \boldsymbol{S}_i^2 \rangle - \langle \boldsymbol{S}_j^2 \rangle\right) = \\ &= -\textstyle\sum_{i<j} J_{ij}\left[S_{ij}\left(S_{ij}+1\right) - S_i(S_i+1) - S_j\left(S_j+1\right)\right] . \end{aligned} \tag{5.5}$$

However, since for each i-j ion pair, S_{ij} can assume different values from $\left(S_i + S_j\right)$ to $\left|S_i - S_j\right|$,

electronic transitions between states with the same S are possible because they are lifted from restrictions mentioned before (*cf.* **Figure 5.3**).

In **Figure 5.4** the electronic spectrum of carbonate-intercalated NiFe-LDH dispersed in water (**Figures 5.4a** and **5.4b**) is compared with the electronic spectra of subsequent aliquots of the reaction mixture taken at different steps during the synthesis of citrate-intercalated NiFe-LDH (**Figure 5.4c** and **5.4d**). Prior to the addition of any Eq_{NaOH}, the solution appears green due to three absorbance bands located at 740 and 660 and ~450 nm (black line in **Figure 5.4c**). The two bands at 740 and 660 nm are related to d-d transitions of $Ni^{(II)}$, while the absorbance band at ~450 nm is mainly d-d transitions in $Fe^{(III)}$, although I cannot exclude a partial contribution of two other d-d transitions in $Ni^{(II)}$ (see **Table 6.1** in Chapter 6 for details about d-d transitions). Then, the LMCT absorbance edge begins at 400 nm saturating the spectrophotometer's detector at 290 nm. The addition of Eq_{NaOH}, makes the solution colour starts turning from green to yellow beyond the equivalent point at 0.4 Eq_{NaOH} (*cf.* **Figure 5.4c**). Thereafter, I observed a progressive increase in the absorbance intensity in the 350-500 nm region. This observation is consistent with the interpretation of the titration profiles. In fact, the polymerization of metal-citrate compounds implies an increasing number of possible exchange interactions between neighbouring $Fe^{(III)}$ and $Ni^{(II)}$ atoms, and therefore an increasing intensity of related spin-forbidden transitions. At the same time, as more Eq_{NaOH} are added, the LMCT absorbance edge shifts by ~100 nm to lower wavelengths. This shift can be explained by the chemical bonds' hydrolysis between transition metals and citrate carboxylic groups forming complexes. In fact, the increase of the photon energy required for a LMCT fits well with the alteration of the $Fe^{(III)}$ or $Ni^{(II)}$ coordination environment. More in detail, it is consistent with a shift from a ligand electron-rich environment constituted by carboxylic groups to a ligand electron-poor environment constituted by hydroxide ions. When the addition Eq_{NaOH} has been completed, the reaction mixture still appears clear of any precipitate, whereas its absorbance spectrum (red line in **Figure 5.4c** and **5.4d**) resembles that of carbonate-intercalated NiFe-LDH (**Figure 5.4a** and **5.4b**). Nevertheless, after performing the ageing treatment at 90°C, the reaction mixture became opaque due to suspended LDH particles, whereas its absorbance spectrum (blue line in **Figure 5.4c** and **5.4d**) shows a further increase of absorbance related to d-d transitions.

Overall, the shape of electronic spectra of carbonate- and citrate-intercalated NiFe-LDHs presented in **Figure 5.4** is similar, showing analogous absorbance features. Moreover, I have shown how the progressive increase in the intensity of absorbance contributions related to spin-forbidden d-d transitions indicates the progressive polymerization of metal-citrate complexes during the NiFe-LDH synthesis.

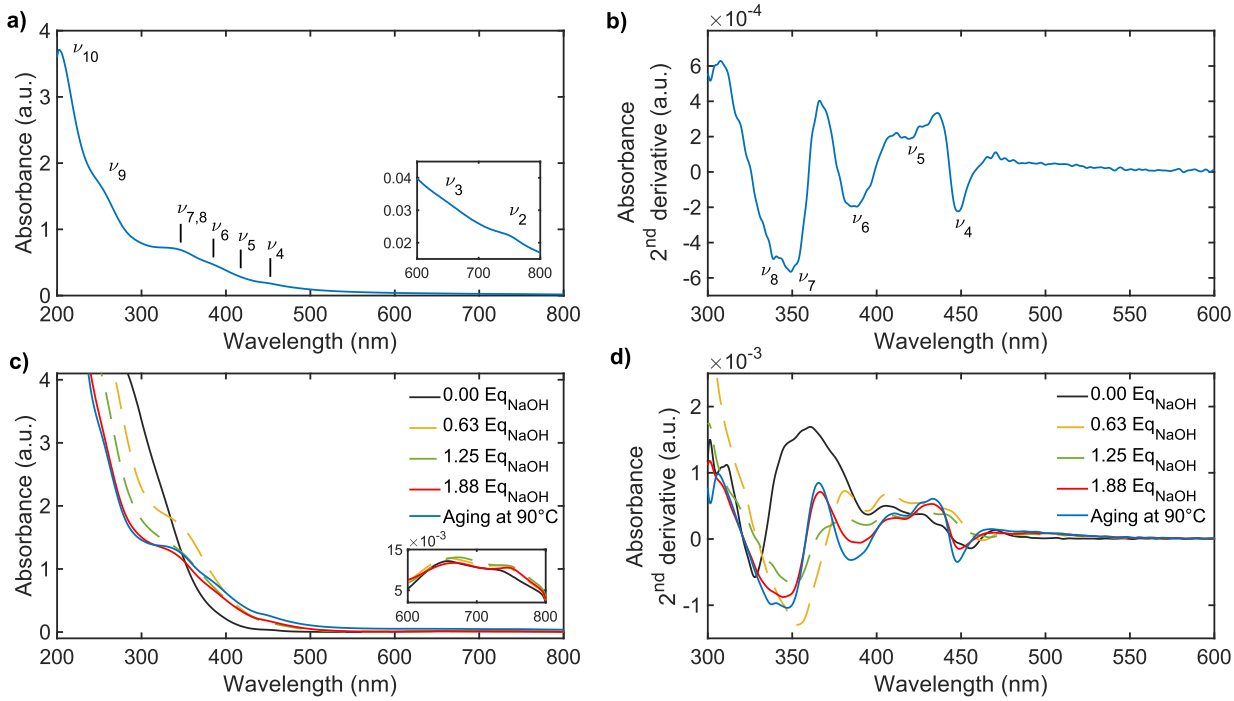

Figure 5.4. *a) Electronic spectrum of carbonate intercalated NiFe-LDH suspended in water, b) second derivative of a). c) Electronic spectra of aliquots collected during the synthesis of citrate intercalated NiFe-LDH via hydrolytic polymerization, d) second derivative of c).*

6. Electronic spectroscopy: absorbance and reflectance of ultraviolet, visible and near infrared light

Despite LDHs are suitable materials to probe the behaviour of transition metal atoms in two-dimensional environments, the electronic spectroscopy of transition-metal-based LDHs is a topic often disregarded in current literature. In fact, only a few studies analysed LDHs' electronic spectra merely assigning the ligand field transitions[35,119,120]. Moreover, these assignments are often carried out by a "citation cascade" leading to incomplete or incorrect absorbance band assignments. Therefore, here I provide first an introduction to the ligand field theory, and then, I describe in detail the absorbance features observed in NiAl- and NiFe-LDHs. For the sake of clarity, I consider transition metals in LDH crystal lattice as if they were coordinated in a perfect octahedral (O_h) symmetry, despite LDHs possess a dihedral (D_{3d}) coordination symmetry with an angle of ~97°. The reduction of symmetry from the O_h to the D_{3d} symmetry involves a splitting of transitions originating from and directed to triply degenerate states (*i.e.*, T_1 and T_2 Mülliken symmetry terms). However, in experimental electronic spectra the splitting of triply degenerate states happens to be less than the resolution of second derivative spectroscopy. Hence, the O_h symmetry is a fair approximation. Eventually, I report for the $Fe^{(III)}$ and $Ni^{(II)}$, in LDH crystal lattices, their respective ligand field strengths ($10Dq$), and their respective Racah parameters (B and C) of Coulomb and exchange interactions.

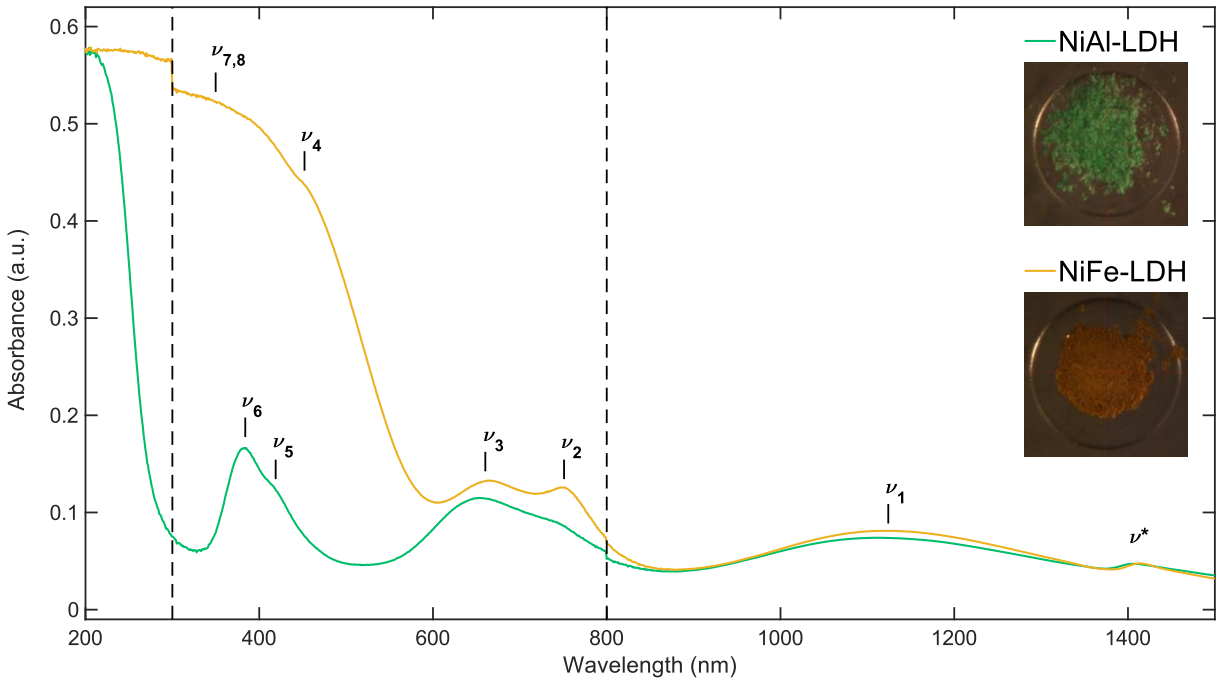

Figure 6.1. *Absorbance spectra computed from reflectance data of citrate intercalated NiAl- and NiFe-LDHs powders. The ligand field transitions are labelled from ν_1 to ν_8. Cf. also* ***Figure 5.4a*** *and* ***5.4b*** *for the absorbance spectra of carbonate-intercalated NiFe-LDH suspended in water. The dashed lines at 300 and 800 indicate the UV lamp and IR detector switches, respectively. ν^* is caused by the overtone of bending vibration modes of residual water.*

Table 6.1. *Electronic transitions observed in the UV-Vis-NIR light absorbance spectra of $Ni_{0.75}Fe_{0.25}$-LDH. The assignment of absorbance bands has been performed according to the ligand field analysis results exposed in Section 6.2.*

Band	Wavelength (nm)	Energy (cm^{-1})	Type	Transition
ν_1	1,120	8,929	d-d $(Ni^{(II)})$	$^3A_{2g}(^3F) \rightarrow {}^3T_{2g}(^3F)$
ν_2	750	13,330	d-d $(Ni^{(II)})$ ‡	$^3A_{2g}(^3F) \rightarrow {}^1E_g(^1D)$
ν_3	665	15,040	d-d $(Ni^{(II)})$	$^3A_{2g}(^3F) \rightarrow {}^3T_{1g}(^3F)$
ν_4	448	22,320	d-d $(Fe^{(III)})$ ‡	$^6A_{1g}(^6S) \rightarrow {}^4E_g, {}^4A_{1g}(^4G)$
ν_5	420	23,810	d-d $(Ni^{(III)})$ ‡	$^3A_{2g}(^3F) \rightarrow {}^1T_{2g}(^1D), {}^1A_{1g}(^1G)$
ν_6	386	25,910	d-d $(Ni^{(II)})$	$^3A_{2g}(^3F) \rightarrow {}^3T_{1g}(^3P)$
			d-d $(Fe^{(III)})$ ‡	$^6A_{1g}(^6S) \rightarrow {}^4T_{2g}(^4D)$
ν_7	348	28,740	d-d $(Fe^{(III)})$ ‡	$^6A_{1g}(^6S) \rightarrow {}^4E_g(^4D)$
ν_8	338	29,590	d-d $(Fe^{(III)})$ ‡	$^6A_{1g}(^6S) \rightarrow {}^4T_{1g}(^4P)$
ν_9	250	40,000	LMCT	$t_{1u}^{\beta} \rightarrow t_{2g}^{\beta}$ $(Fe^{(III)})$
ν_{10}	210	47,620	LMCTs	$t_{1u}^{\beta} \rightarrow e_g^{\beta}$ $(Fe^{(III)}, Ni^{(II)})$
			MOs of $R\text{-}COO^-$	$n \rightarrow \pi^*$ (HOMO → LUMO)

‡ Spin-forbidden transitions.
d-d = Ligand Field Transitions (parity-forbidden).
LMCT = Ligand-to-Metal Charge Transfer.
MO = Molecular Orbital.
HOMO and LUMO = Highest Occupied MO and Lowest Unoccupied MO.

6.1. The ligand field theory

By considering the hydrogenic atom approximation, if a transition-metal atom is surrounded by six Ze point-charges (where e is the elementary charge), arranged in an O_h symmetry, at a distance of a from the central atom, the five d orbital wavefunctions undergo a loss of degeneracy. It follows that two new sets of orbitals are formed, constituted respectively by three and two of the five formers d orbitals. The three orbitals at lower energy are referred to as t_2, while the remaining two, at higher energy, are referred to as e (not to be confused with the elementary charge)[i]. The energy gap between t_2 and e is known as "ligand field splitting parameter" or "ligand field strength", and is defined as $10Dq$ (or $\Delta_0 = 10Dq$), in which

$$Dq = -\frac{Ze^2}{6a^5} \cdot \langle r^4 \rangle_{nl} \,, \qquad (\mathbf{6.1}\boldsymbol{a})$$

[i] The t_2 and e nomenclature originates from Mülliken symmetry terms T_2 and E. Lower-case letters are used to indicate hydrogenic orbital wavefunctions instead of symmetries. In octahedral symmetry, the orbitals formed by the ligand field are often referred to as t_{2g} and e_g, where the g letter stands for "gerade" (*even* in German), indicating the presence of a centre of inversion. The same model can also be applied for tetrahedral symmetry which lacks a centre of inversion; hence, in this section I omit the g subscript.

with

$$\langle r^{2+m}\rangle_{nl} = \int |R_{nl}(r)|^2 \cdot r^{2+m} dr\,. \qquad (\mathbf{6.1b})$$

Here $R_{nl}(r)$ represents the radial component of the hydrogenic d orbitals wavefunction, r is the modulus of the coordinate vector, whereas n, l and m are the three quantum numbers. Moving away from the hydrogenic atom approximation implies increasing complexity, because the presence of more than one electron in the d shell requires linear combinations of multiple Slater determinants to describe the electronic state wavefunctions. The number of Slater determinants is given by the binomial coefficient

$$\binom{m}{n} = \frac{m!}{n!\,(m-n)!} \qquad (\mathbf{6.2})$$

in which m is the maximum number of electrons that can be accommodated into d orbitals (*i.e.*, 10) and n is the number of electrons located into d orbitals (*e.g.*, 45 determinants for the d^2 configuration). In 1954, and the following years, Y. Tanabe and S. Sugano published a series of papers in which they describe the energy of ligand field states in the form of matrices[121–123]. Given a generic d^n configuration, its energy matrices ($\boldsymbol{\mathcal{T}}_{S\Gamma}$) group together states having wavefunctions with the same spin-symmetry term (*i.e.*, $S\Gamma$). Here, Γ is a Mülliken symmetry term and S its total spin (not to be confused with the S symbol for the orbital momentum). Each $\boldsymbol{\mathcal{T}}_{S\Gamma}$ results by the sum of the matrix of configurations ($\boldsymbol{\mathcal{E}}_{S\Gamma}$) and the matrix of Coulomb interactions ($\boldsymbol{\mathcal{C}}_{S\Gamma}$) as follows:

$$\boldsymbol{\mathcal{T}}_{S\Gamma} = \boldsymbol{\mathcal{E}}_{S\Gamma} + \boldsymbol{\mathcal{C}}_{S\Gamma}\,. \qquad (\mathbf{6.3})$$

$\boldsymbol{\mathcal{E}}_{S\Gamma}$ is a diagonal matrix whose elements are the integrals of unperturbed $S\Gamma$ states (non-interacting electrons), *i.e.*,

$$\boldsymbol{\mathcal{E}}_{S\Gamma} = diag\left(\left\langle t_2^h e^k \middle| \boldsymbol{\mathcal{H}}_0 \middle| t_2^h e^k \right\rangle_{S\Gamma(SL_1)}, \ldots, \left\langle t_2^h e^k \middle| \boldsymbol{\mathcal{H}}_0 \middle| t_2^h e^k \right\rangle_{S\Gamma(SL_i)}\right)\,, \qquad (\mathbf{6.4})$$

where $\boldsymbol{\mathcal{H}}_0$ is the unperturbed ligand field Hamiltonian, h and k are the number of electrons occupying t_2 and e orbitals, respectively ($h + k = n$ for d^n). SL_i is the spin-orbit term of the i^{th} state, in which L is the orbital momentum term (*i.e.*, S, P, D, F, …). As a result, the elements of $\boldsymbol{\mathcal{E}}_{S\Gamma}$ are multiple of Dq as follows:

$$\left\langle t_2^h e^k \middle| \boldsymbol{\mathcal{H}}_0 \middle| t_2^h e^k \right\rangle_{S\Gamma(SL_i)} = (6k - 4h) \cdot 10Dq\,, \qquad (\mathbf{6.5a})$$

or

$$\left\langle t_2^{6-h} e^{4-k} \middle| \boldsymbol{\mathcal{H}}_0 \middle| t_2^{6-h} e^{4-k} \right\rangle_{S\Gamma(SL_i)} = (4h - 6k) \cdot 10Dq \qquad (\mathbf{6.5b})$$

for complementary configurations (*i.e.*, d^{10-n}). The $\boldsymbol{\mathcal{C}}_{S\Gamma}$ matrix is symmetric, having as diagonal elements the integrals arising from the $\boldsymbol{\mathcal{H}}_1$ perturbation term of the ligand field Hamiltonian, *i.e.*, $\left\langle t_2^h e^k \middle| \boldsymbol{\mathcal{H}}_1 \middle| t_2^h e^k \right\rangle_{S\Gamma(SL_i)}$, while the off-diagonal elements of $\boldsymbol{\mathcal{C}}_{S\Gamma}$ are superposition integrals between the i^{th} and j^{th} state belonging to the same $S\Gamma$ term, *i.e.*, $\left\langle t_2^u e^w \middle| \middle| t_2^h e^k \right\rangle_{S\Gamma(SL_{i,j})}$. All elements of Coulomb interactions matrices across d^n systems have been expressed as linear combinations of Racah parameters, namely B and C[i], by Y. Tanabe and S. Sugano[109,121]. Hence, the

[i] Racah parameters are defined as linear combinations of Slater-Condon integrals $F^{(k)}$, where $k = 2l$. $B = \frac{1}{49}F^{(2)} - \frac{5}{441}F^{(4)}$ and $C = \frac{5}{63}F^{(4)}$.

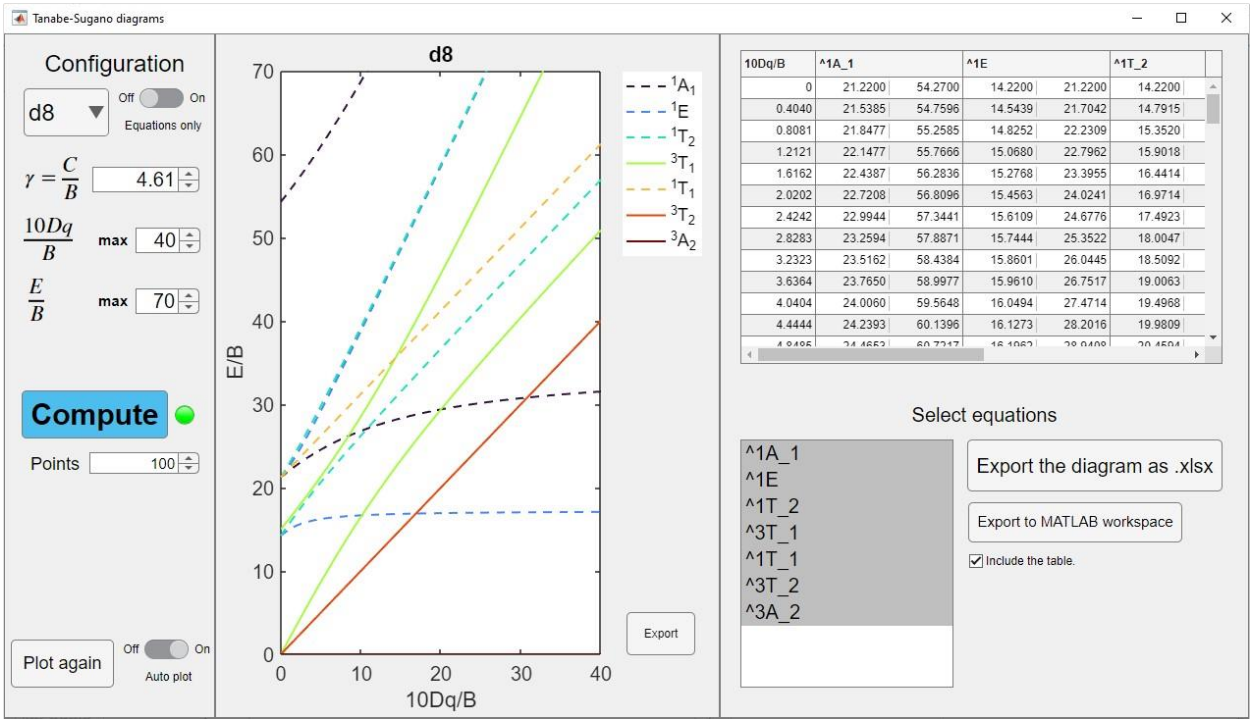

Figure 6.2. *GUI of the MATLAB app I built to compute the eigenvalues of Tanabe-Sugano matrices and the respective diagrams (version 1.1). Computation options are in the left tab. The diagram is displayed in the central panel, from which it can be exported as a separate figure. The right panel contains the table containing the diagram's numerical data that can be exported as a Microsoft Excel file or onto the MATLAB workspace. The right tab also displays a selection menu to export symbolic equations to the MATLAB workspace to perform the ligand field analysis.*

expressions describing the energy of ligand field states ($\tilde{\nu}_{S\Gamma(SL_i)}$) as functions of Dq, B and C, are the eigenvalues of $\boldsymbol{\mathcal{T}}_{S\Gamma}$ as follows:

$$eig(\boldsymbol{\mathcal{T}}_{S\Gamma}) = \begin{pmatrix} \tilde{\nu}_{S\Gamma(SL_1)} \\ \vdots \\ \tilde{\nu}_{S\Gamma(SL_i)} \end{pmatrix}, \qquad (\mathbf{6.6})$$

Therefore, energies of electronic transitions are computed by subtracting the energy of the ground state ($\tilde{\nu}_{[S\Gamma(SL)]_{gs}}$) from the diagonal elements of $\boldsymbol{\mathcal{T}}_{S\Gamma}$, as follows[i]:

$$eig\left(\boldsymbol{\mathcal{T}}_{[S\Gamma(SL)]_{gs}\rightarrow S\Gamma}\right) = eig(\boldsymbol{\mathcal{T}}_{S\Gamma}) - \tilde{\nu}_{[S\Gamma(SL)]_{gs}} \cdot \boldsymbol{I}\,. \qquad (\mathbf{6.7})$$

6.2. Ligand field analysis

In the past, the eigenvalues of 2×2 matrices were manually computed, whereas the eigenvalues of larger matrices were computed by approximating off-diagonal elements as multiples of $B^2/(10Dq)$[124]. Nowadays, to the best of my knowledge, only two pieces of open-access software, designed to run on modern computers (*i.e.*, 64-bit systems), can compute the eigenvalues of $\boldsymbol{\mathcal{T}}_{S\Gamma}$

[i] Given the $n \times n$ matrix $\boldsymbol{\mathcal{A}}$ with eigenvalues $\{\lambda_1, \ldots, \lambda_n\}$, the eigenvalues of $\alpha\boldsymbol{I} + \boldsymbol{\mathcal{A}}$ are $\{\lambda_1 + \alpha, \ldots, \lambda_n + \alpha\}$ with $\alpha \in \mathbb{C}$ and $\boldsymbol{I}$ is the identity matrix.

matrices and plot the respective Tanabe-Sugano diagrams (*e.g.*, see **Figure 6.3**)[125,126]. However, these two pieces of software present themselves multiple scripts and require the user to run preliminary tasks, by command line, to correctly execute the program. Hence, I have decided to code my own program with MATLAB to compute the eigenvalues of Tanabe-Sugano matrices. The main advantage of MATLAB programming language is that it assumes all variables to be matrices, thus symbolic operations on matrices are easy to code. Moreover, by writing the code, I have followed a procedure in-line with how Tanabe and Sugano approached to the ligand field theory (the approach in Section 6.1). In fact, instead of writing multiple scripts, I have stored only the $\boldsymbol{\mathcal{C}}_{S\Gamma}$ matrices of d^2, d^3, d^4 and d^5 configurations as local functions written inside the main code of the program. Then, the program calls the appropriate function according to the d^n configuration requested by the user. Subsequently, the elements of $\boldsymbol{\mathcal{E}}_{S\Gamma}$ are computed according to $(\mathbf{6.5}\boldsymbol{a})$ for d^2 to d^5 configurations, or according to $(\mathbf{6.5}\boldsymbol{b})$ for complementary configurations (*i.e.*, d^{10-n}). Eventually, the expressions for the energy of ligand field transitions are symbolically computed according to $(\mathbf{6.6})$ and $(\mathbf{6.7})$, and stored into a cell array to be used for the ligand field analysis. The advantage of symbolic computations is that algebraic expressions are returned[i] and then used for subsequent computations. If requested by the user, Tanabe-Sugano diagrams are also computed at a fixed C/B ratio over an array of Dq/B values. The number of elements and the upper limits of the Dq/B arrays are also defined by the user. Lastly, I have provided a graphical user interface (GUI) *via* the MATLAB app designer (*cf.* **Figure 6.2**). The software is available for download at the MATLAB Central File Exchange[127].

Given three non-degenerate electronic transitions, at least one out of which is spin-forbidden, the ligand field analysis consists into solving a system of the three equations describing the energy of the selected transitions, from the ground state $[S\Gamma(SL)]_{gs}$, to three non-degenerate exited states $[S\Gamma(SL)]_n$, placing as known terms the energy experimentally observed ($\tilde{\nu}_{n,obs}$), *i.e.*,

$$\begin{pmatrix} \tilde{\nu}_{[S\Gamma(SL)]_{gs}\rightarrow[S\Gamma(SL)]_1} \\ \tilde{\nu}_{[S\Gamma(SL)]_{gs}\rightarrow[S\Gamma(SL)]_2} \\ \tilde{\nu}_{[S\Gamma(SL)]_{gs}\rightarrow[S\Gamma(SL)]_3} \end{pmatrix} = \begin{pmatrix} \tilde{\nu}_{1,obs} \\ \tilde{\nu}_{2,obs} \\ \tilde{\nu}_{3,obs} \end{pmatrix} \qquad (\mathbf{6.8})$$

The solutions to $(\mathbf{6.8})$ are not always trivial, hence for straightforward ligand field analysis is pivotal to reduce as much as possible the degree of $(\mathbf{6.8})$. For instance, by picking transitions to exited states belonging to the same $S\Gamma$ in the d^8 configuration (*i.e.*, $Ni^{(II)}$), the quadratic terms cancel out lowering $(\mathbf{6.8})$ to the 1st degree. Analogously, in the d^5 configuration (*i.e.*, $Fe^{(III)}$) spin-flip transitions are only linearly dependent on B and C, hence by placing two spin-flip transitions into $(\mathbf{6.8})$, its degree with respect to Dq is lowered to the 2nd. The next two sub-sections refer mainly to NiFe-LDHs electronic spectra; however, analogous considerations can also be applied to NiAl-LDHs. The ligand field analysis results are reported in **Table 6.2** and used to plot the Tanabe-Sugano diagrams displayed in **Figure 6.3**. To avoid confusion in text, tables and diagrams, I use the standard spectroscopic notation from now on, in which $S\Gamma(SL)$ states are labelled according to their spin multiplicity, instead of their total spin, resulting into the ${}^{2S+1}\Gamma({}^{2S+1}L)$ notation (*e.g.*, the ${}^6A_1({}^6S)$ state has $L = 0$ and $S = 5/2$).

[i] MATLAB algebraically computes eigenvalues up to 4×4 matrices by default. In case of larger matrices, MATLAB algebraically computes the eigenvalues whenever possible; when this is not possible, the eigenvalues are expressed via the `root(_)` function.

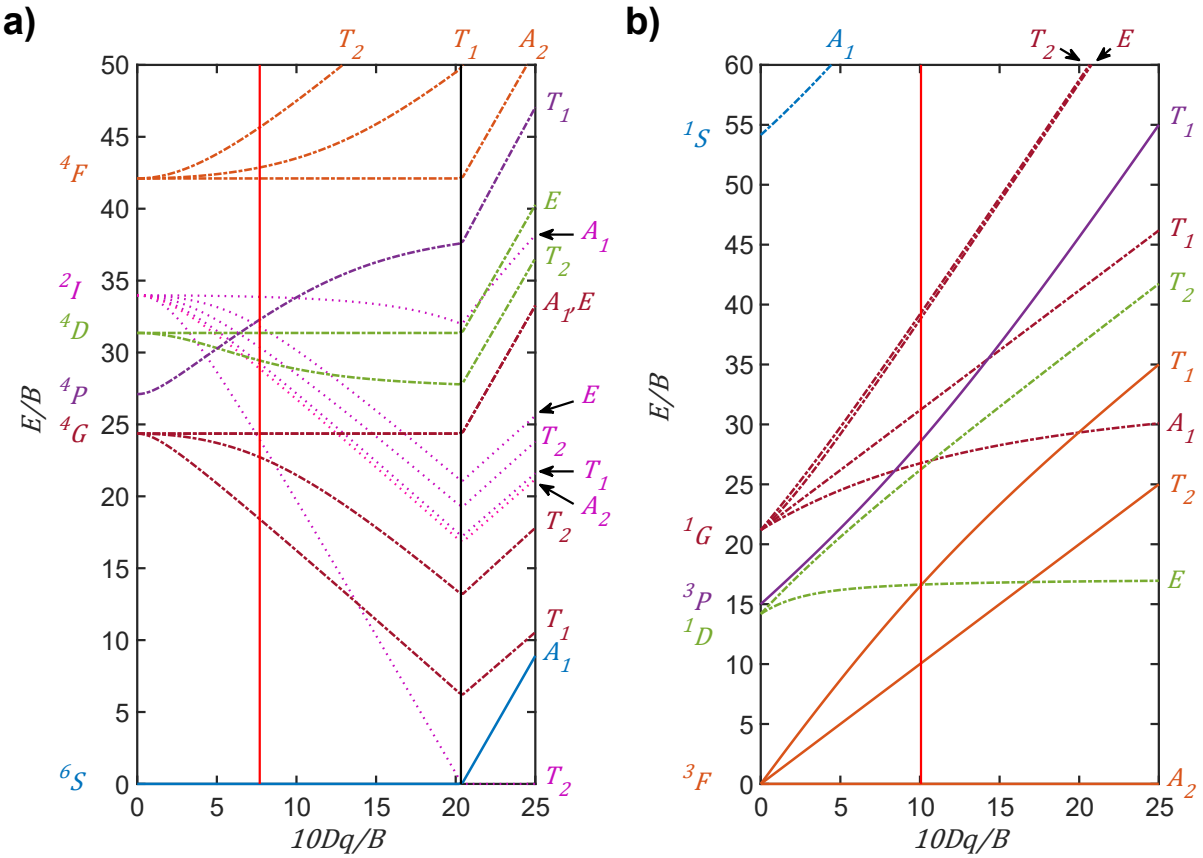

Figure 6.3. *Tanabe-Sugano diagrams of a) d^5 octahedral and tetrahedral configurations and b) d^8 octahedral or d^2 tetrahedral configuration. The abscissae report the ligand field strength, normalized by B, while the ordinates report the energies, also normalized by B, of ligand field states. In each diagram the abscissae axis always corresponds to the ground state. Here, energy states are colour-coded according to their spin-orbit terms which are reported on the left (i.e., blue for S, violet for P, green for D, orange for F, purple for G and pink for I). Moreover, energy states with the same spin multiplicity as the high-spin ground state are represented with a plain line, while energy states with a spin multiplicity different from the high-spin ground state are represented with a dashed line. The symmetry term of each energy state is reported on the top-right of the diagrams according to the Mulliken nomenclature (the spin multiplicity is omitted). The vertical black line in the d^5 diagram represents the boundary between the high-spin region (left) and the low-spin region (right). The red vertical lines indicate the $10Dq/B$ ratios I computed for NiFe-LDH. Racah parameters used in computations: a) B = 916 cm^{-1}, C = 2,632 cm^{-1}; b) B = 887 cm^{-1}, C = 4,075 cm^{-1}.*

Table 6.2. *Ligand field analysis results on NiAl- and NiFe-LDHs spectra displayed in* ***Figure 6.1****.*

		Ligand field parameters (cm^{-1})					Nephelauxetic ratios	
	Material	$\mathbf{10}\boldsymbol{Dq}$	$\boldsymbol{B}$	$\boldsymbol{C}$	$\boldsymbol{Dq/B}$	$\boldsymbol{C/B}$	$\boldsymbol{\beta}$	$\boldsymbol{\beta_1}$[a]
$\boldsymbol{Ni^{(II)}}$	NiAl-LDH	9,009	892	4,054	1.01	4.54	0.857	1.200
	NiFe-LDH	8,929	887	4,075	1.01	4.59	0.852	1.199
	Ni^{2+}	-	1,041[29]	4,831[29]	-	4.64	1	$\sqrt{2}$
$\boldsymbol{Fe^{(III)}}$	NiFe-LDH	7,682[b]	916	2,632	0.84	2.87	0.903	1.056
	Fe^{3+}	-	1,015[128]	4,800[128]	-	4.73	1	$\sqrt{2}$

[a] Defined as: $\beta_1 = \sqrt{\left(\frac{B}{B_0}\right)^2 + \left(\frac{C}{C_0}\right)^2}$, *cf.* ref. [129] for details.

[b] Computed from the contribution to the absorbance of ${}^6A_{1g}({}^6S) \rightarrow {}^4T_{1g}({}^4P)$.

6.2.1. Nickel

The Ni^{2+} ion has an $[Ar]4s^0 3d^8$ electronic configuration, resulting into seven different symmetry terms (*i.e.*, ${}^3A_2$, ${}^3T_2$, ${}^3T_1$, ${}^1A_1$, ${}^1E$, ${}^1T_2$ and ${}^1T_1$), spread across five spin-orbit terms (*i.e.*, ${}^3P$, ${}^3F$, ${}^1S$, ${}^1D$ and ${}^1G$), *cf.* **Figure 6.3b**. In the d^8 configuration, the ground state is ${}^3A_2({}^3F)$, whose energy is expressed as follows:

$$eig\left(\boldsymbol{\mathcal{T}}_{{}^3A_2}\right) = \tilde{\nu}_{{}^3A_2({}^3F)} = -8B - 12Dq\,. \qquad (\mathbf{6.9})$$

Transitions from the ${}^3A_2({}^3F)$ ground state to ${}^3T_2({}^3F)$, ${}^3T_1({}^3F)$ and ${}^3T_1({}^3P)$ exited states produce the characteristic absorbance features present in electronic spectra of nickel-based compounds[30,35,52,115,130–136]. For the sake of conciseness, I refer to these transitions as ν_1, ν_3 and ν_6, respectively[i] (*cf.* **Table 6.1**). I have detected all out of these transitions in NiFe-LDH (and NiAl-LDH) electronic spectra, although I resorted to second-derivative spectroscopy to resolve ν_6[119]. The energy of ${}^3T_2({}^3F)$, which is the first exited state is defined as

$$eig\left(\boldsymbol{\mathcal{T}}_{{}^3T_2}\right) = \tilde{\nu}_{{}^3T_2({}^3F)} = -8B - 2Dq\,, \qquad (\mathbf{6.10})$$

by subtracting $(\mathbf{6.9})$ from $(\mathbf{6.10})$, results that the value of Dq is straightforward from the energy of the first observed transition (*i.e.*, $\tilde{\nu}_1$) as follows:

$$eig\left(\boldsymbol{\mathcal{T}}_{{}^3A_2({}^3F)\rightarrow{}^3T_2({}^3F)}\right) = \tilde{\nu}_{{}^3A_2({}^3F)\rightarrow{}^3T_2({}^3F)} = \tilde{\nu}_1 = 10Dq\,. \qquad (\mathbf{6.11})$$

In nickel-based hydroxides, $\tilde{\nu}_1$ falls at ~9,000 cm^{-1} (~1,100 nm)[35,52,132,137], with slightly variations depending on dopant $M^{(III)}$ species, as illustrated in **Figure 6.1** and in **Table 6.2**. The energies of transitions from ${}^3A_2({}^3F)$ ground state to ${}^3T_2({}^3F)$ and ${}^3T_1({}^3P)$ exited states (*i.e.*, $\tilde{\nu}_3$ and $\tilde{\nu}_6$) are eigenvalues of the 2 × 2 matrix $\boldsymbol{\mathcal{T}}_{{}^3A_2({}^3F)\rightarrow{}^3T_1({}^3F,{}^3P)}$ as follows:

$$eig\left(\boldsymbol{\mathcal{T}}_{{}^3A_2({}^3F)\rightarrow{}^3T_1({}^3F,{}^3P)}\right) = \begin{pmatrix}\tilde{\nu}_{{}^3A_2({}^3F)\rightarrow{}^3T_1({}^3F)}\\ \tilde{\nu}_{{}^3A_2({}^3F)\rightarrow{}^3T_1({}^3P)}\end{pmatrix} = \begin{pmatrix}\tilde{\nu}_3\\ \tilde{\nu}_6\end{pmatrix} = \begin{pmatrix}7.5B + 15Dq - \sigma_1\\ 7.5B + 15Dq + \sigma_1\end{pmatrix}$$
$$\sigma_1 = 0.5 \cdot \sqrt{(15B)^2 + (10Dq)^2 - 180Dq \cdot B} \qquad (\mathbf{6.12})$$

Hence, by rearranging $(\mathbf{6.12})$, the value of B proceeds as follows:

$$\tilde{\nu}_6 + \tilde{\nu}_3 = 15(B + 2Dq)\,. \qquad (\mathbf{6.13})$$

Unfortunately, at $10Dq$ of ~9,000 cm^{-1} the ${}^3T_1({}^3F)$ state is close in energy to the spin-flip ${}^1E({}^1D)$ state, resulting into a state mixing[133–135]. This state mixing enhances the absorbance related to the ${}^3A_2({}^3F) \rightarrow {}^1E({}^1D)$ spin-forbidden transition[133–135], namely ν_2. Hence, ν_2 and ν_3 appear as a two-peaked absorbance band centred at ~700 nm (~14,300 cm^{-1}) as illustrated in **Figure 6.1**, therefore several authors prefer to report it as a single ${}^3A_2({}^3F) \rightarrow {}^3T_1({}^3F)$, ${}^1E({}^1D)$ transition[52,132,136,138]. Given this, I have decided to separately report $\tilde{\nu}_2$ and $\tilde{\nu}_3$ for an easy comparison with literature data, however I used the average $\tilde{\nu}_2$ and $\tilde{\nu}_3$ values in $(\mathbf{6.13})$. Thus, $(\mathbf{6.13})$ yielded similar values of B close to 890 cm^{-1} in both NiAl- and NiFe-LDHs, leading to a Dq/B ratio of 1.01 in both cases. In addition, I observed the contribution to the absorbance of two spin-forbidden transitions from the ground state ${}^3A_2({}^3F)$ to the ${}^1A_1({}^1G)$ and ${}^1T_2({}^1D)$ exited states. I refer to their combined

[i] I label the electronic transitions with ν, whereas I refer to the energy (in cm^{-1}) of electronic states and transitions between them as $\tilde{\nu}$.

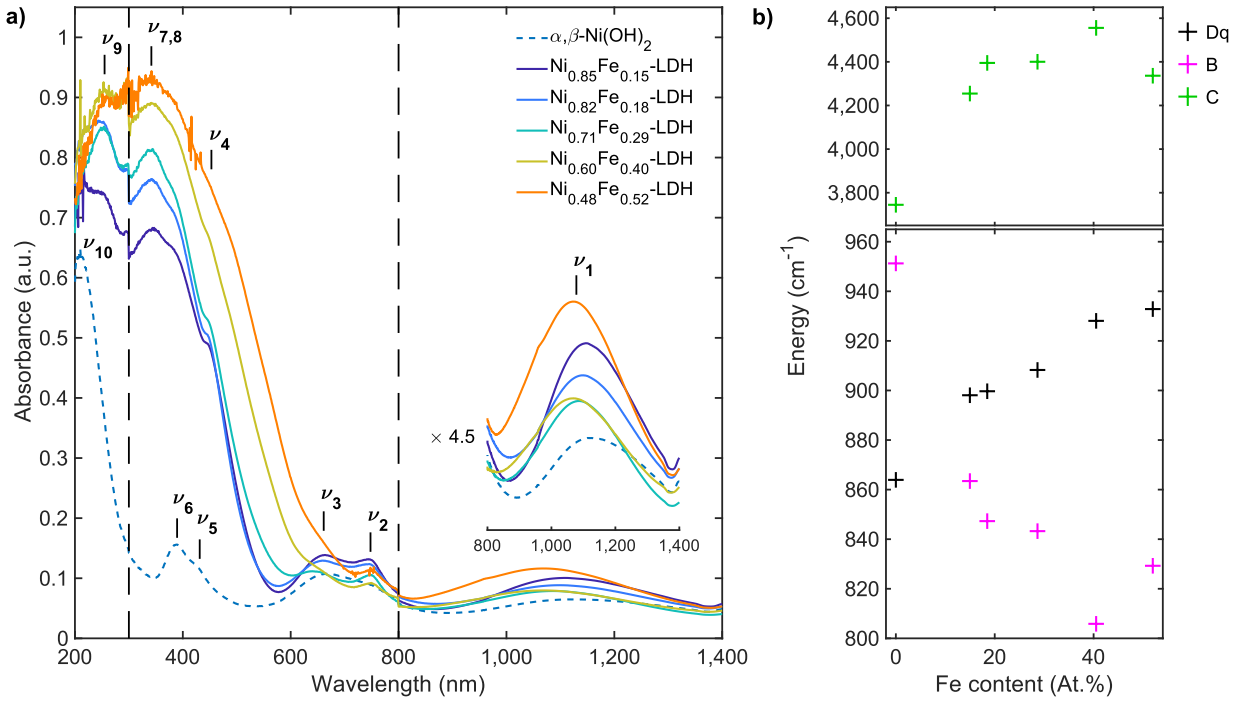

Figure 6.4. *a) Electronic spectra of layered $Ni^{(II)}$ hydroxides with variable content of $Fe^{(III)}$. b) Ligand field parameters of $Ni^{(II)}$ in layered hydroxides with variable content of $Fe^{(III)}$.*

contribution to the absorbance as ν_5. In a d^8 electronic configuration, the expressions of spin-forbidden transitions are defined as follows:

$$eig\left(\boldsymbol{\mathcal{T}}_{^3A_2(^3F)\rightarrow{}^1A_1(^1G,^1S)}\right) = \begin{pmatrix} 10Dq + 17B + 4.5C - \sigma_2 \\ 10Dq + 17B + 4.5C + \sigma_2 \end{pmatrix}$$
$$\sigma_2 = 0.5 \cdot \sqrt{(20Dq)^2 + (10B)^2 + (5C)^2 + 80Dq \cdot B + 40Dq \cdot C + 100B \cdot C} \quad , \qquad (\mathbf{6.14})$$

$$eig\left(\boldsymbol{\mathcal{T}}_{^3A_2(^3F)\rightarrow{}^1E(^1D,^1G)}\right) = \begin{pmatrix} 10Dq + 8.5B + 2C - \sigma_3 \\ 10Dq + 8.5B + 2C + \sigma_3 \end{pmatrix}$$
$$\sigma_3 = 0.5 \cdot \sqrt{(20Dq)^2 + (7B)^2 + 40Dq \cdot B} \quad , \qquad (\mathbf{6.15})$$

$$eig\left(\boldsymbol{\mathcal{T}}_{^3A_2(^3F)\rightarrow{}^1T_2(^1D,^1G)}\right) = \begin{pmatrix} 15Dq + 8.5B + 2C - \sigma_4 \\ 15Dq + 8.5B + 2C + \sigma_4 \end{pmatrix}$$
$$\sigma_4 = 0.5 \cdot \sqrt{(10Dq)^2 + (7B)^2 + 20Dq \cdot B} \qquad (\mathbf{6.16})$$

and

$$eig\left(\boldsymbol{\mathcal{T}}_{^3A_2(^3F)\rightarrow{}^1T_1(^1G)}\right) = 10Dq + 12B + 2C\,. \qquad (\mathbf{6.17})$$

Hence, the C parameter can be computed from the $(\mathbf{6.14})$ with the negative sign before the square root term as follows:

$$\begin{pmatrix} 10Dq \\ 15(B + 2Dq) \\ 10Dq + 17B + 4.5C - \sigma_2 \end{pmatrix} = \begin{pmatrix} \tilde{\nu}_1 \\ \tilde{\nu}_6 + \tilde{\nu}_3 \\ \tilde{\nu}_5 \end{pmatrix} \qquad (\mathbf{6.18})$$

Eventually, the values of C calculated according $(\mathbf{6.18})$ are 4,045 and 4,074 cm^{-1} for NiAl- and NiFe-LDH, respectively. Placing $(\mathbf{6.15})$ as third equation onto $(\mathbf{6.18})$ yielded C values ~200 cm^{-}

[1] lower, whereas C calculated according ($\mathbf{6.16}$) were ~200 cm^{-1} higher in comparison with values reported above. Noteworthy, the ionic degree of ligand-metal bond is historically defined as $\beta = B/B_0$ and called nephelauxetic ratio[29] (if β is equal to 1 the ligand-metal bond is completely ionic). Where B_0 corresponds to the Racah parameter B of the corresponding isolated metal ion. However, M. Brik et al.[129,139] recently proposed an alternative version of the nephelauxetic ratio in which C and C_0 (*i.e.*, the B_0 analogous) are also considered. This alternative nephelauxetic ratio, namely β_1, is defined as $\sqrt{(B/B_0)^2 + (C/C_0)^2}$. I point out that a proper comparison between β and β_1 should be made by normalizing the latter by $\sqrt{2}$. It follows that both NiAl- and NiFe-LDHs have a $\beta_1/\sqrt{2}$ value of 0.849 that is comparable to the analogous value of β (*cf.* **Table 6.2**). By comparison, I performed the same ligand field analysis on the spectroscopic data provided by M. Oliver-Tolentino et al.[35] yielding a $\beta_1/\sqrt{2}$ value of 0.862 for carbonate-intercalated nickel-based LDHs. Whereas the data provided by L. Poul et al.[137] yielded a $\beta_1/\sqrt{2}$ value of 0.860 for nickel hydroxide-acetate (which is isomorphous to LDHs). On the contrary, from the data provided by A. Harvey et al.[52], a β value of 0.797 is yielded for ~10 layer thick β-$Ni(OH)_2$ nanosheets (the authors disregarded the C Racah parameter, nor provided the wavelength of any spin-forbidden transitions). Hence, I conclude that the $Ni^{(II)}$ nephelauxetic ratio in nickel based LDHs is not significantly influenced by the nature of the trivalent metal cation hosted in the hydroxide layers, nor by the nature of the anions amid them.

Table 6.3. *Ligand field parameters and nephelauxetic ratios of layered $Ni^{(II)}$ hydroxides with variable content of $Fe^{(III)}$.*

$Fe^{(III)}$ (At. %)	$10Dq$ (cm^{-1})	B (cm^{-1})	C (cm^{-1})	$\beta_1/\sqrt{2}$
0.02[a]	8,639	951.3	3,745	0.847
14.97	8,981	863.4	4,255	0.855
18.48	8,997	847.3	4,395	0.863
28.65	9,083	843.3	4,400	0.862
40.39	9,281	805.9	4,556	0.863
51.97	9,328	829.3	4,334	0.848

[a] Reagent impurities.

I have decided to also investigate how the quantity in iron content alters the optical properties of NiFe-LDHs (**Figure 6.4a**) and consequently their $Ni^{(II)}$ ligand field parameters (**Table 6.3** and **Figure 6.4b**). As shown in **Figure 6.4b**, I have observed a progressive increase of the $10Dq$ value of $Ni^{(II)}$, with increased $Fe^{(III)}$ content. According to ($\mathbf{6.1}\boldsymbol{a}$), I associate this $10Dq$ increase to a progressive contraction of the LDH unit cell long the crystallographic a-axis. According to literature, the a-axis of bulk β-$Ni(OH)_2$ measures 3.126 Å[30], the a-axis of turbostratic α-$Ni(OH)_2$ measures ~3.08 Å[30], whereas the a-axes of takovite[i] and reevesite[ii] minerals measure 3.0250 and 3.082 Å, respectively[53]. Thus, by means of X-ray diffraction, I measured an a-axis length of 3.1057 Å for mixed α,β-$Ni(OH)_2$, 3.0886 Å for $Ni_{0.82}Fe_{0.18}$-LDH, 3.0837 Å for $Ni_{0.71}Fe_{0.29}$-LDH, and

[i] Natural $Ni_6Al_2(OH)_{16}CO_3 \cdot 4H_2O$.
[ii] Natural $Ni_6Fe_2(OH)_{16}CO_3 \cdot 4H_2O$.

3.0849 Å nm $Ni_{0.48}Fe_{0.52}$-LDH[i]. Moreover, the Racah parameters of $Ni^{(II)}$ follow a diverging trend with the increase of $Fe^{(III)}$ content. Nevertheless, across all materials, the overall $Ni^{(II)}$ nephelauxetic ratio variation is only 0.016, indicating that the ratio of $Fe^{(III)}$ does not significantly affect the ionic degree of Ni-O bond.

6.2.2. Iron

The Fe^{3+} ion has an $[Ar]4s^0 3d^5$ electronic configuration, resulting into ten different symmetry terms (*i.e.*, ${}^6A_1$, ${}^4A_1$, ${}^4A_2$, ${}^4E$, ${}^4T_1$, ${}^4T_2$, ${}^2A_2$, ${}^2A_1$, ${}^2E$, ${}^2T_1$ and ${}^2T_2$) spread across 16 spin-orbit terms. Eleven out of the 16 spin-orbit terms are doublets, four are quartets and one is a sextet (*i.e.*, ${}^6S$, ${}^4P$, ${}^4D$, ${}^4F$, ${}^4G$, ${}^2S$, ${}^2P$, $a\ {}^2D$, $b\ {}^2D$, $c\ {}^2D$, $a\ {}^2F$, $b\ {}^2F$, $a\ {}^2G$, $b\ {}^2G$, ${}^2H$ and ${}^2I$). However, since ferric oxides and hydroxides are limited to high-spin $Fe^{(III)}$, I can ignore all doublet terms and only consider the sextet ${}^6A_1({}^6S)$ that is the ground state, and the quartet terms. The electronic states belonging to aforementioned terms are graphically represented in **Figure 6.3a**, with the addition of the ${}^2I$ team that is needed to define the boundary between the high-spin regime and the low-spin regime. Contrary to $Ni^{(II)}$, the energy of the $Fe^{(III)}$ ground state is independent by Dq, being dependent only on B as follows:

$$\tilde{\nu}_{{}^6A_1({}^6S)} = eig\left(\boldsymbol{\mathcal{T}}_{{}^6A_1}\right) = -35B\ . \qquad (\mathbf{6.19})$$

Transitions from the ${}^6A_1({}^6S)$ ground state to the exited states ${}^4E({}^4G)$ and ${}^4E({}^4D)$ are "pure" spin-flips, since the energy of these exited states is also independent from Dq, being dependent only on B and C. More in detail, the ${}^6A_1({}^6S) \rightarrow {}^4E({}^4G)$ transition results from a spin-flip into t_2 orbitals while the ${}^6A_1({}^6S) \rightarrow {}^4E({}^4D)$ results from a spin-flip into e orbitals[109,121]. For the sake of simplicity, I refer to the aforementioned transitions as ν_4 and ν_7, respectively, while their energy is defined as follows:

$$eig\left(\boldsymbol{\mathcal{T}}_{{}^6A_1({}^6S)\rightarrow{}^4E({}^4G,{}^4D)}\right) = \begin{pmatrix}\tilde{\nu}_{{}^6A_1({}^6S)\rightarrow{}^4E({}^4G)}\\ \tilde{\nu}_{{}^6A_1({}^6S)\rightarrow{}^4E({}^4D)}\end{pmatrix} = \begin{pmatrix}\tilde{\nu}_4\\ \tilde{\nu}_7\end{pmatrix} = \begin{pmatrix}10B+5C\\ 17B+5C\end{pmatrix}\ . \qquad (\mathbf{6.20})$$

A third "pure" spin-flip transition is also expected[110,111], namely ${}^6A_1({}^6S) \rightarrow {}^4A_2({}^4F)$, of which the energy is defined as follows:

$$eig\left(\boldsymbol{\mathcal{T}}_{{}^6A_1({}^6S)\rightarrow{}^4A_2({}^4F)}\right) = \tilde{\nu}_{{}^6A_1({}^6S)\rightarrow{}^4A_2({}^4F)} = 22B+7C\ . \qquad (\mathbf{6.21})$$

However, the energy of ${}^6A_1({}^6S) \rightarrow {}^4A_2({}^4F)$ exceeds the one of the first LMCT transition, hence the former is not detectable[110,111]. For the sake of completeness, another Dq independent transition is expected, namely ${}^6A_1({}^6S) \rightarrow {}^4A_1({}^4G)$, whose energy is provided as follows:

$$eig\left(\boldsymbol{\mathcal{T}}_{{}^6A_1({}^6S)\rightarrow{}^4A_1({}^4G)}\right) = \tilde{\nu}_{{}^6A_1({}^6S)\rightarrow{}^4A_1({}^4G)} = 10B+5C\ . \qquad (\mathbf{6.22})$$

[i] The $Ni_{0.48}Fe_{0.52}$-LDH X-ray reflections were sitting on a background ascribable to an amorphous phase. The large excess of iron hinders the complete crystallization of the LDH phase.

I point out that ${}^6A_1({}^6S) \rightarrow {}^4E({}^4G)$ and ${}^6A_1({}^6S) \rightarrow {}^4A_1({}^4G)$ transitions are degenerate by pure chance. In fact, whereas the former originates from a spin-flip, the latter originates from the spin-spin interactions between t_2 and e subshells half-filled of electrons[i].

For the sake of conciseness, I report the equations describing electronic transitions to Dq-dependent exited states, *i.e.*, ${}^4T_1({}^4G, {}^4P, {}^4F)$ and ${}^4T_2({}^4G, {}^4D, {}^4F)$, in the form of determinants as follows:

$$eig\left(\boldsymbol{\mathcal{T}}_{{}^6A_1({}^6S)\rightarrow {}^4T_1({}^4G,{}^4P,{}^4F)}\right) \Downarrow \quad -\begin{vmatrix} 10B+6C-10Dq-\tilde{\nu} & 3\sqrt{2}B & -C \\ 3\sqrt{2}B & 19B+7C+0Dq-\tilde{\nu} & -3\sqrt{2}B \\ -C & -3\sqrt{2}B & 10B+6C+10Dq-\tilde{\nu} \end{vmatrix} = 0 \qquad (\mathbf{6.23})$$

and

$$eig\left(\boldsymbol{\mathcal{T}}_{{}^6A_1({}^6S)\rightarrow {}^4T_2({}^4G,{}^4D,{}^4F)}\right) \Downarrow \quad -\begin{vmatrix} 18B+6C-10Dq-\tilde{\nu} & -\sqrt{6}B & -4B-C \\ -\sqrt{6}B & 13B+5C+0Dq-\tilde{\nu} & -\sqrt{6}B \\ -4B-C & -\sqrt{6}B & 18B+6C+10Dq-\tilde{\nu} \end{vmatrix} = 0 . \qquad (\mathbf{6.24})$$

By rearranging $(\mathbf{6.20})$ the $Fe^{(III)}$ Racah parameters (*i.e.*, B and C) can be directly obtained from $\tilde{\nu}_4$ and $\tilde{\nu}_7$, whereas the magnitude of Dq in ferric compounds is usually yielded by the energy of transitions from ${}^6A_1({}^6S)$ ground state to ${}^4T_1({}^4G)$ or ${}^4T_2({}^4G)$ exited states[110,111] according to $(\mathbf{6.23})$ or $(\mathbf{6.24})$. However, I have detected these transitions at 557 and 493 nm[ii], respectively, only in the electronic spectra of samples with an atomic iron percentage greater than 33%. This suggests that two adjacent iron atoms are required to enable transitions to ${}^4T_{1g}({}^4G)$ and ${}^4T_{2g}({}^4G)$ states. Hence, I had to resort to the energy of the ${}^6A_1({}^6S) \rightarrow {}^4T_{1g}({}^4P)$, which is present in the electronic spectra of all samples, for the determination of Dq. My calculations yielded a $10Dq$ value of 7,682 cm^{-1} for $Fe^{(III)}$ in NiFe-LDHs. This value is approximately half of the ~15,000 cm^{-1} $10Dq$ accepted from octahedral $Fe^{(III)}$ in metal-oxide crystal lattices[110–112], being consistent with $(\mathbf{6.1}\boldsymbol{a})$ that describes the linear relationship between Dq and the effective charge of the ligands[109]. According to my ligand field analysis (*cf*. the red vertical line in **Figure 6.3a**), the aforementioned two transitions from the ${}^6A_{1g}({}^6S)$ ground state of $Fe^{(III)}$ to the ${}^4T_{1g}({}^4G)$ and ${}^4T_{2g}({}^4G)$ exited states should fall at ~590 and ~480 nm, respectively (between ν_3 and ν_4 in **Figure 6.4a**). These values are close to the observed ones in spectra of samples with iron percentage greater than 33%. Meanwhile the values of $Fe^{(III)}$ Racah parameters B and C are equal to 916 and 2,632 cm^{-1}. This yielded the unusual C/B ratio equal to 2.87 I have found for $Fe^{(III)}$ in NiFe-LDH. In fact, in ferric oxide compounds a C/B ratio ranging from 4 to 6 is usually expected[110,111,128]. I speculate that this

[i] In the high-spin d^5 configuration, the ground state of the t_2 subshell is the quartet ${}^4A_2$ ($S_{{}^4A_2} = 3/2$), whereas the ground state of the e subshell is the quartet ${}^3A_2$ ($S_{{}^3A_2} = 1$)[109]. Hence the spin-spin interactions between ${}^4A_2$ and ${}^3A_2$ terms produces three states namely: ${}^6A_1({}^6S)$ with $S = 5/2$, ${}^4A_1({}^4G)$ with $S = 3/2$ and ${}^2A_1({}^2G)$ with $S = 1/2$.

[ii] Values obtained by means of second derivative spectroscopy.

unusual C/B is the result of exchange interactions between $Fe^{(III)}$ and $Ni^{(II)}$, because a similar decrease in C/B ratio has been reported for interactions between $Cr^{(III)}$ pairs in metal-oxide crystal lattices[118]. The yielded $\beta_1/\sqrt{2}$ value for $Fe^{(III)}$ in NiFe-LDH is 0.747 (the B_0 and C_0 values of Fe^{3+} are 1,015 and 4,800 cm^{-1}, respectively)[128]. I also performed the same ligand field analysis on the spectroscopic data of ferric compounds provided by D. M. Sherman et al.[110,111] to have a reliable comparison. As shown in **Figure 6.5**, the excepted $\beta_1/\sqrt{2}$ value of $Fe^{(III)}$ in metal-oxide compounds ranges between 0.6 and 0.7; it follows that the Fe-O bond is more ionic in NiFe-LDH rather than in metal-oxide compounds. In my opinion, the evidence that $Fe^{(III)}$ in NiFe-LDH exhibits superior nephelauxetic ratio, compared to the corresponding ferric oxides, is consistent to the benchmarking catalytic performance of the NiFe-LDH for oxygen evolution reaction[140–142], which I also described in Chapter 4.

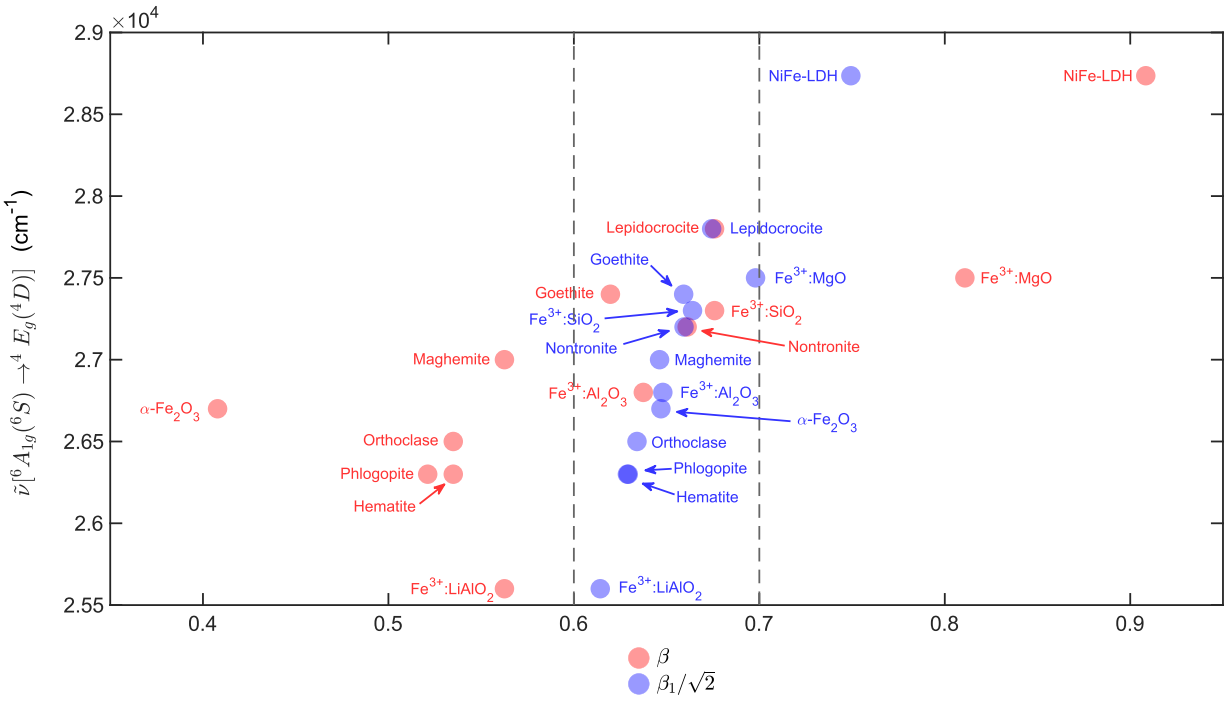

Figure 6.5. *Scatter plot of the energy of the $^6A_{1g}(^6S) \rightarrow {}^4E_g(^4D)$ transitions in ferric compounds vs. their respective nephelauxetic ratios. Apart from NiFe-LDH, the nephelauxetic ratios were computed from the spectroscopic data provided in refs. [110,111]. The dashed lines delimit the range of nephelauxetic ratios expected in ferric compounds.*

7. Conclusions and future perspectives

In this thesis, I analysed the stability of nickel-iron layered double hydroxides (NiFe-LDHs) dispersed in ethanol with acetate anions, through the lens of surface energy, Hansen parameters and zeta potential. It turns out that acetate anions bind to the surface of LDHs at the inner Helmholtz plane, effectively neutralizing the LDH native positive surface charge. Hence, acetate anions cover the surface of LDH nanosheets stabilizing the ethanol dispersion like a surfactant. However, the excessive presence of acetate on the surface limits the LDH performances toward electrocatalytic oxygen evolution reaction (OER). In fact, the lower Lewis basicity of acetate anions, compared to carbonate and citrate, hinders the base-assisted deprotonation steps required for OER, limiting the whole process. Interestingly, intercalating citrate anions in LDH lead to the direct formation of single-layer nanosheets. As revealed by pH-potentiometric titrations and electronic spectroscopy investigations, citrate intercalated LDH nanosheets form in two steps. The first step involves a partial hydrolysis and polymerization of metal-citrate coordination compounds resulting from an increase in the reaction environment pH. The second step consists of the complete hydrolysis of the metal-citrate compounds following heating of the reaction environment, which leads to the direct formation of LDH nanosheets. Lastly, I performed an extensive study on the electronic spectra on NiFe-LDH, which led to an in-depth ligand field analysis on $Ni^{(II)}$ and $Fe^{(III)}$ located in the LDH crystal lattices. The analysis results indicate that the ligand field strength ($10Dq$) of $Ni^{(II)}$ in NiFe-LDH increases with the $Fe^{(III)}$ content. On the contrary, the $Ni^{(II)}$ nephelauxetic ratio, *i.e.*, the ionic degree of the Ni-O bond, is not significantly affected by the $Fe^{(III)}$ content. On the other hand, $Fe^{(III)}$ in NiFe-LDH showed $10Dq$ of 7,682 cm^{-1} that is approximately half of the ~15,000 cm^{-1} value expected in ferric oxides. Moreover, a $Fe^{(III)}$ nephelauxetic ratio of 0.747 suggests that the Fe-O bond in NiFe-LDH is more ionic than oxide counterparts, whose nephelauxetic ratio ranges from 0.6 to 0.7.

In conclusion, the stabilization LDH nanosheets in ethanol by acetate anions provides insights on greener methodologies to produce LDH dispersions, possibly using water as a solvent. These dispersions may find future applications in industry for the fabrication of electrodes to be used for water electrolysis, fuel cells or battery applications. Moreover, the effect of acetate anions on the electrocatalytic properties of NiFe-LDHs provides additional information about its electrocatalytic mechanism towards the OER, which is still under debate[35,143–146]. Hence, a full comprehension of the NiFe-LDH electrocatalytic mechanism towards the OER may lead in the future to the development of more efficient electrocatalysts improving the yield of molecular hydrogen and oxygen production through water electrolysis, opening new possibilities for a carbon free society and new developments in space exploration. In addition, the results about the formation mechanism of LDHs in the presence of citrate may be extended to other hydroxy-carboxylate anions (*e.g.*, lactate, malate), providing important information about the behaviour of LDH materials in biological systems, which can lead to an improvement of LDHs as drug delivery systems. Lastly, the spectroscopic and ligand field analysis results on NiFe-LDHs constitute an important milestone in the comprehension of the behaviour of iron group elements into a two-dimensional environment. Ultimately, these spectroscopic results may lead to more advanced ligand field engineering strategies aimed at mimicking metal-based enzymes, which, according to the alkaline vents hypothesis, originated from LDH deposits on the Hadean Ocean floor more than four billion years ago[63,64].

8. Acknowledgements

Warm thanks are due to the following people:

Francesco Bonaccorso: Supervisor at Istituto Italiano di Tecnologia, and for providing help, advice, and research facilities at Istituto Italiano di Tecnologia and at BeDimentional s.p.a.

Diego Colombara: Supervisor at Università degli Studi di Genova, and for providing help, advice and research facilities at Università degli Studi di Genova.

Liberato Manna: For providing help, advice, and research facilities at Istituto Italiano di Tecnologia.

Sebastiano Bellani: For providing assistance and precious suggestions in all topics treated in my PhD.

Michele Ferri: For providing support for electrochemical characterizations.

Gabriele Bianca: For providing support for transmission electron microscopy imaging.

Elisa Mantero: For performing support at Graphene Labs.

Lea Pasquale: For performing the X-ray fluorescence analysis of LDH samples.

Sergio Marras: For acquiring the X-ray diffraction pattern.

Andrea Griesi: For refining the X-ray diffraction pattern.

Giammarino Pugliese: For performing support for zeta potential measurements.

Gabriele La Rosa: For performing support for electronic spectroscopy.

Simone Nitti: For performing support in the chemistry laboratory.

Filippo Drago: For performing support in the chemistry laboratory.

Francesco De Donato: For performing support in the chemistry laboratory.

Renata Riva: PhD coordinator at Università degli Studi di Genova.

The present work was carried out at Graphene Labs, Chemistry Lab Facility, Materials Characterization Facility, and Electron Microscopy Facility at Istituto Italiano di Tecnologia, via Morego 30, 16163 Genoa, Italy.

9. Appendices

9.1. Comparison Tables

Table 9.1. *Recent electrochemical data of the electrocatalytic activities of NiFe-LDH electrodes. I referred to studies in which are used substrate with area comparable to my case (i.e., graphite paper). Adapted with permission from Piccinni, M.; Bellani, S.; Bianca, G.; Bonaccorso, F. Nickel-Iron Layered Double Hydroxide Dispersions in Ethanol Stabilized by Acetate Anions. Inorg Chem* ***2022****, 61 (11), 4598–4608. Copyright 2022 American Chemical Society.*

Catalyst @Support	**Substrate material**	**Electrolyte**	**Tafel slope (mV/dec)**	**Overpotential (V) @ 10 mA/cm$^2_{geom}$**	**Ref.**
NiFe-CO_3-1	Graphite paper	0.1 M KOH	30	0.38	This thesis, [119]
NiFe-CO_3-2	Graphite paper	0.1 M KOH	47	0.54	This thesis, [119]
NiFe-Cit	Graphite paper	0.1 M KOH	38	0.43	This thesis, [119]
NiFe(DS^-)LDH @graphitized carbon	Glassy carbon RDE	1 M KOH	36	0.30	[147]
NiFe-LDH nanosheets	Cu mesh	1 M KOH	78.19	0.292	[148]
NiFe-LDH nanopsheets	Glassy carbon	0.1 M KOH	33.4	0.29	[149]
NiFe-LDH spheres @activated carbon	Glassy carbon	1 M KOH	59	0.295	[150]
Fe-doped $Ni(OH)_2$ @carbon black	Glassy carbon	1 M KOH	37	0.216	[151]
NiFe-LDH nanosheets	Graphite paper	1M KOH	32	0.254	[152]
NiFe-LDH @graphdiyne	Cu foil	1M KOH	95	0.260	[153]
NiFe-LDH @SWNT	Glassy carbon	1M KOH	35	0.250	[154]

Table 9.2. *Crystallographic parameters of synthetic LDHs and related minerals. Table continues in the following page.*

Synthetic LDHs

$M^{(II)}$	$M^{(III)}$	A^{n-}	**Basal spacing (nm)**	**a-axis (nm)**	**c-axis (nm)**	**Reference**
Ni	Al	Citrate	1.223	0.3019	3.669	This thesis
Ni	Fe	Citrate	1.227	0.3053	3.680	This thesis
Zn	Al	Citrate	1.222	0.3056	3.665	This thesis
Ni	Fe	Carbonate	0.77561	0.30907	2.32684	This thesis
Ni	Fe	Carbonate	0.770	n.a.	n.a.	[119]
Ni	Fe	Carbonate	0.784	n.a.	n.a.	[119]
Ni	Fe	Citrate	1.22	n.a.	n.a.	[119]
Mg	Al	Citrate	1.20	n.a.	n.a.	[70]
Mg	Al	Citrate	1.18	n.a.	n.a.	[69]
Ni	Al	Citrate	1.17	n.a.	n.a.	[69]
Zn	Al	Citrate	1.23	n.a.	n.a.	[69]
Zn	Al	Citrate	1.22	n.a.	n.a.	[88]
Zn	Al	Nitrate	0.89	0.308	n.a.	[88]
Ni	Al	Carbonate	0.7513	0.3023	2.2538	[35]
Ni	Fe	Carbonate	0.7481	0.3070	2.2443	[35]
Ni	Fe	Carbonate	0.7596	0.3080	2.2789	[35]
Ni	Al	Nitrate	0.860	0.300	2.58	[31]
Ni	Fe	Nitrate	0.794	0.307	2.382	[31]
Ni	Fe	Adipate	1.308	0.307	3.925	[31]
Ni	Fe	Sebacate	1.539	0.307	4.617	[31]

Table continues in the following page.

LDH minerals[a]

Mineral name	Composition	Basal spacing (nm)	a-axis (nm)	c-axis (nm)	Reference
Hydrotalcite	$Mg_6Al_2(OH)_{16}CO_3 \cdot 4H_2O$	n.a.	0.3065	2.307	[53]
Takovite	$Ni_6Al_2(OH)_{16}CO_3 \cdot 4H_2O$	n.a.	0.30250	2.2595	[53]
Reevesite	$Ni_6Fe_2(OH)_{16}CO_3 \cdot 4H_2O$	n.a.	0.3082	2.2770	[53]
Zaccagnaite	$Zn_4Al_2(OH)_{12}CO_3 \cdot 4H_2O$	n.a.	0.30662	2.26164	[53]

[a] All LDH minerals are referred to 3R polymorphs. Despite for 3R LDH polymorphs the unit cell c axis and the basal plane are in a 3:1 relationship, we decided to only include what is actually reported in referenced works.

n.a. = not available.

Table 9.3. *Absorbance bands in electronic spectra of natural and synthetic oxide and hydroxides of $Ni^{(II)}$ and $Fe^{(III)}$.*

Nickel based LDHs

Sample	Transition wavelength (nm)										Ref.
	ν_1	ν_2	ν_3	ν_4	ν_5	ν_6	ν_7	ν_8	ν_9	ν_{10}	
NiFe-LDH	1,120	750	665	448	420	386	348	338	250	210	-
NiAl-LDH	1,110	740	655	-	420	383	-	-	-	210	-
NiFe-LDH	-	750	650	450	420	385	350	-	250	210	[119]
NiFe-LDH	1,105	730	630	450	420	375	350	-	260	210	[35]
NiAl-LDH	1,105	730	630	-	420	375	-	-	-	210	[35]
NiAl-LDH	-	730	630	-	420	375	-	-	-	-	[120]

Nickel based compounds

Sample	Transitions wavelength (nm)										Ref.
	ν_1	ν_2	ν_3	ν_4	ν_5	ν_6	ν_7	ν_8	ν_9	ν_{10}	
$Ni^{(II)}$:Pyrophyllite	1,086	725	649	-	388[a]		-	-	-	-	[132]
Exfoliated $Ni(OH)_2$	1,100	700[a]		-	400[a]		-	-	-	-	[52]
$Ni^{(II)}$ hydroxy-acetate	1,240	761	671	-	440	387	-	-	-	-	[137]
NiO	-	715[a]		-	429	379	-	-	-	295	[136]
β-$Ni(OH)_2$	-	705[a]		-	423	381	-	-	-	226	[138]

Iron based compounds

Sample	Transitions wavelength (nm)										Ref.
	ν_1	ν_2	ν_3	ν_4	ν_5	ν_6	ν_7	ν_8	ν_9	ν_{10}	
Fe^{3+}:Al_2O_3	-	-	-	449	-	392	373	308	259	194	[111]
Fe^{3+}:MgO	-	-	-	460	-	398	364	322	279 246[c]	216	[111]
Synthetic α-Fe_2O_3	-	-	-	420	-	-	374	314	257	223	[111]
Nontronite	-	-	-	444	-	384	367	-	261	200	[111]
Hematite	-	-	-	444	-	405	380	319	270	-	[110]
Goethite	-	-	-	435	-	-	365	285	250	225	[110]
Maghemite	-	-	-	435	-	-	370	315	250	-	[110]
Lepidocrocite	-	-	-	435	-	-	365	305	239	210	[110]

[a] The authors reported the average value of ν_2 and ν_3.
[b] The authors reported the average value of ν_5 and ν_6.
[c] The contribution to the absorbance of $t_{2u}^{\beta} \rightarrow t_{2g}^{\beta}$ LMCT transition is also present.

9.2. Materials end methods

9.2.1. Chemicals

Table 9.4. *Chemicals used. All chemicals were purchased from Sigma-Aldrich and used without purifications.*

Name	Formula	Notes
Aluminium nitrate nonahydrate	$Al(NO_3)_3 \cdot 9H_2O$	ACS reagent, ≥98%
Ethanol	CH_3CH_2OH	puriss. p.a., absolute, ≥99.8% (GC)
Ferric nitrate nonahydrate	$Fe(NO_3)_3 \cdot 9H_2O$	ACS reagent, ≥98%
Nickel acetate tetrahydrate	$Ni(CH_3O_2)_2 \cdot 4H_2O$	purum p.a., ≥99.0% (KT)
Nickel nitrate hexahydrate	$Ni(NO_3)_2 \cdot 6H_2O$	puriss. p.a., ≥98.5% (KT)
Potassium hydroxide	KOH	reagent grade, 90%, flakes
Sodium hydroxide	$NaOH$	reagent grade, ≥98%, pellets (anhydrous)
Triethanolamine	$N(CH_2CH_2OH)_3$	≥99.0% (GC)
Trisodium citrate dihydrate	$Na_3HC_6H_4O_7 \cdot 2H_2O$	meets USP testing specifications
Urea	$OC(NH_2)_2$	ACS reagent, 99.0-100.5%
Zinc nitrate hexahydrate	$Zn(NO_3)_2 \cdot 6H_2O$	purum p.a., crystallized, ≥99.0% (KT)

Unless otherwise specified, I used as solvent only Milli-Q water previously degassed by boiling it for 20 min under Ar bubbling, to avoid atmospheric CO_2 contamination.

9.2.2. Characterizations

Table 9.5. *Characterization techniques. Sample preparations are listed under the header lines indicating the characterization, instrumentation, and supplier. Table continues in the following page.*

Technique	Instrumentation	Supplier
Atomic force microscopy (AFM)	**Innova AFM**	**Bruker**
• Sample: 10 µL of LDH ethanol dispersion are drop casted on mica. • Tip diameter less than 10 nm. Tapping mode on an area of 20×20 µm^2, resolution 1024×1024 points.		
Electrochemistry	**Potentiostat/galvanostat station VMP3**	**Biologic**
• Working electrode preparation: the electrodes were produced by manually spray-coating the LDH dispersions onto a graphite paper (PGS, Panasonic) placed on a hot plate at 100°C. The dispersion volume loaded in the air brusher was empirically adjusted to control the mass loading of the LDHs at a value of 0.1 mg/cm^2. About 20% of the loaded material is lost during the spray coating process, the loss quantity may vary with different operators. • Counter electrode: platinum wire. • Reference electrode: Ag/AgCl in saturated KCl. • Electrolyte: KOH 0.1 M. • Cyclic voltammetry (CV): 10 activation cycles, from 0 to 1.5 V vs. reference electrode at 5 mV/s scan rate. • Electrochemical impedance spectroscopy (EIS): 200 kHz to 0.1 Hz range, with 10 mV wave amplitude at open circuit potential. • Staircase voltammetry (SV): sequential chronoamperometry scans at increasing potential. The current is sampled manually once steady state is reached. • Potential correction by the cell resistance: the cell resistance (R) is obtained from the intercept of the EIS Nyquist plot with the real axis. Then all measured potentials in SV are corrected according to $E_{corr} = E_{measured} - R \cdot i$, where is the measured current i.		
Electronic spectroscopy (UV-Vis-NIR)	**Varian Cary 5000**	**Agilent**
• Liquid samples: dispersions and solutions in ethanol or water. Operating transmission mode. Samples are placed into Suprasil® QS quartz cuvettes with 4 mm optical path (Hellma Analytics). • Solid samples: powders. Operating in reflection mode. Powders are placed on Suprasil® QX quarts slabs (Hellma Analytics). 1 mg of LDH material is suspended in 100 µL of water, drop casted onto the quartz slab and let dry at 100°C on a hot plate.		

Table continues in the following page.

Technique	Instrumentation	Supplier
Potentiometric pH-titrations	**Sension+ PH3**	**HACH**
• Titrations performed manually • Electrode: CRISON 50 14T • Calibration buffer solutions from HACH: pH 4.01/7.00/10.01 • Temperature 25°C		
Transmission electron microscopy (TEM)	**JEM 1400 Plus - 120 kV TEM (thermionic source LaB_6 crystal)** **JEM 1011 - 100 kV TEM (W filament thermionic source).**	**JEOL**
• Sample: drop-casting the 1:100 diluted LDH dispersions (approx. 0.001 g/L) in ethanol onto ultrathin C-on-holey C-coated Cu grids by Ted Pella.		
X-ray diffraction (XRD)	**PANalytical EmpyreanX-ray diffractometer**	**Malvern Panalytical**
• Sample: thin film drop casted from LDH dispersions in ethanol or water on Si(100) or LDH powder (pellet).		
X-ray fluorescence (XRF)	**M4 TORNADO micro-XRF**	**Bruker**
• Sample: thin film drop casted on Si(100) or powder (pellet).		
Zeta potential (ζ)	**Zetasizer Nano**	**Malvern Panalytical**
• Samples are diluted by a factor of 10 to avoid particle aggregation (approx. 0.01 g/L).		

9.2.3. Synthesis procedures

Table 9.6. *Synthesis procedure, via the "urea hydrolysis" method, for carbonate-intercalated NiFe-LDHs. Samples used in* ***Figure 6.4*** *are synthetized by varying the ratio between nickel and iron precursors and then analysing the atomic composition of each product (powder) by X-ray fluorescence as described in* ***Table 9.5****.*

Step	Procedure
1)	Degassing water is not necessary for this synthesis. 1.2 mmol of $Ni(NO_3)_2 \cdot 6H_2O$ (349 mg), 0.4 mmol of $Fe(NO_3)_3 \cdot 9H_2O$ (161.6 mg) and 2.8 mmol of urea (168.2 mg) are dissolved in water up to a volume of 160 ml.
1a)	1.2 mmol of $Ni(CH_3CO_2)_2 \cdot 4H_2O$ (*i.e.*, 298.6 mg) are used instead of $Ni(NO_3)_2 \cdot 6H_2O$ for synthesis that rely on acetate anions in the reaction mixture
2)	The solution from Step 1 (or 1a) is transferred in a glass bottle and 1.6 mmol of triethanolamine (212.4 µL) are added dropwise under vigorous stirring, then the bottle is sealed and left under stirring for 24h at ambient temperature.
3)	A ferrihydrite (iron oxyhydroxide) precipitate forms as suspension at the end of Step 2. This suspension is transferred in a 250 ml round flask and heated at 100°C under reflux for 48h.
4)	At the end of Step 3 a yellowish precipitate is formed at the bottom of the flask. The most supernatant is carefully removed with a pipette. Then the obtained product is then isolated by centrifugation at 3000 relative centrifugal force and washed three times by replacing the remaining supernatant with 10 mL of water.

Carbonate-intercalated LDHs can be stored as dry powders obtained by freeze-drying the precipitates from step 4) at -50°C for two days.

The freeze-dried LDH powders should be handled with care since the risk to inhale them is real. I always handled LDH powders under fume hood while wearing FFP2 face masks. Then, all surfaces that may be exposed to LDH powders are cleaned with water.

Table 9.7. *Optimized synthesis procedure, via the "hydrolytic polymerization", for citrate-intercalated LDHs.*

Step	Procedure for NiAl- or NiFe-LDH	Procedure for ZnAl-LDH
1)	0.4 mmol of $Al(NO_3)_3 \cdot 9H_2O$ (*i.e.*, 150.0 mg) or $Fe(NO_3)_3 \cdot 9H_2O$ (*i.e.*, 161.6 mg) are dissolved into 160 mL of water alongside 1.2 mmol of $Ni(CH_3CO_2)_2 \cdot 4H_2O$ (*i.e.*, 298.6 mg) in a 250 mL glass bottle.	6 mmol of $Al(NO_3)_3 \cdot 9H_2O$ (*i.e.*, 2.25 g) are dissolved into 160 mL of water alongside 12 mmol of $Zn(NO_3)_2 \cdot 6H_2O$ (*i.e.*, 3.57 g) in a 250 mL glass bottle.
2)	1.6 mmol of $Na_3HC_6H_4O_7 \cdot 2H_2O$ (*i.e.*, 470.6 mg) are dissolved into 4 mL of water and then added to the solution prepared in step 1) under vigorous stirring. The bottle is sealed and heated on a hot plate set at 80°C under stirring. After one hour, the bottle is let to cool down to ambient temperature.	18 mmol of $Na_3HC_6H_4O_7 \cdot 2H_2O$ (*i.e.*, 5.29 g) are dissolved into 10 mL of water and then added to the solution prepared in step 1) under vigorous stirring. The bottle is sealed and heated on a hot plate set at 80°C under stirring. After one hour, the bottle is let to cool down to ambient temperature.
3)	30 mL of a $NaOH$ 0.1 M solution is added dropwise to the step 2) solution under vigorous stirring.	34 mL of a $NaOH$ 1 M solution is added dropwise to the step 2) solution under vigorous stirring.
4)	The step 3) solution is transferred into a three-neck 250 mL round flask and heated at 90°C by using a heating mantle. The temperature is measured by placing a thermometer in direct contact with the solution. The flask is connected to a bubble condenser to avoid water evaporation and the whole apparatus is kept filled with Ar to avoid atmospheric CO_2 contamination.	The step 3) solution is transferred into a three-neck 250 mL round flask and heated at 60°C by using a heating mantle. The temperature is measured by placing a thermometer in direct contact with the solution. The flask is connected to a bubble condenser to avoid water evaporation and the whole apparatus is kept filled with Ar to avoid atmospheric CO_2 contamination.
5)	After three days, the product of step 4) is collected by centrifugation at 3000 relative centrifugal force and washed three times with 10 mL of water.	After three days, the product of step 4) is collected by centrifugation at 3000 relative centrifugal force and washed three times with 10 mL of water.

Citrate-intercalated LDHs can be stored as dry powders obtained by freeze-drying the precipitates from step 5) at -50°C for two days.

The freeze-dried LDH powders should be handled with care since the risk to inhale them is real. I always handled LDH powders under fume hood while wearing FFP2 face masks. Then, all surfaces that may be exposed to LDH powders are cleaned with water.

Table 9.8. *Production of LDH nanosheets ethanol dispersions.*

Step	Procedure
1)	Synthetize LDHs according to **Table 9.6** or **Table 9.7**. Collect the LDH by centrifugation at 3000 relative centrifugal force. Do not wash the LDH obtained from the synthesis. Do not dry the LDH.
2)	Suspend the wet LDH from Step 1 in a sodium acetate 0.1 M solution. Leave in contact the LDH with the solution for 20 min under stirring.
3)	Collect the LDH by centrifugation at 3000 relative centrifugal force.
4)	Repeat Step 2 and 3.
5)	Wash the LDH with 10 ml of ethanol.
6)	Separate the LDH by centrifugation at 3000 relative centrifugal force. Then collect an UV-Vis spectrum of the supernatant.
If	The supernatant is yellow and the absorbance at 350 nm has plateaued, proceed to Step 7.
Else	Discard the supernatant and go back to Step 5.
7)	Suspend the LDH in 40 ml of ethanol and centrifugate at 3000 relative centrifugal force to separate undispersed particles.

References

(1) Croft, R. C. Lamellar Compounds of Graphite. *Quarterly Reviews, Chemical Society* **1960**, *14* (1), 1. https://doi.org/10.1039/qr9601400001.

(2) Wu, J.; Lerner, M. M. Structural, Thermal, and Electrical Characterization of Layered Nanocomposites Derived from Sodium-Montmorillonite and Polyethers. *Chemistry of Materials* **1993**, *5* (6), 835–838. https://doi.org/10.1021/cm00030a019.

(3) Joensen, P.; Frindt, R. F.; Morrison, S. R. Single-Layer MoS2. *Mater Res Bull* **1986**, *21* (4), 457–461. https://doi.org/10.1016/0025-5408(86)90011-5.

(4) Adachi-Pagano, M.; Forano, C.; Besse, J.-P. Delamination of Layered Double Hydroxides by Use of Surfactants. *Chemical Communications* **2000**, No. 1, 91–92. https://doi.org/10.1039/a908251d.

(5) WALKER, G. F. Macroscopic Swelling of Vermiculite Crystals in Water. *Nature* **1960**, *187* (4734), 312–313. https://doi.org/10.1038/187312a0.

(6) Novoselov, K. S.; Geim, A. K.; Morozov, S. v.; Jiang, D.; Zhang, Y.; Dubonos, S. v.; Grigorieva, I. v.; Firsov, A. A. Electric Field Effect in Atomically Thin Carbon Films. *Science (1979)* **2004**, *306* (5696), 666–669. https://doi.org/10.1126/science.1102896.

(7) Ferrari, A. C.; Bonaccorso, F.; Fal'ko, V.; Novoselov, K. S.; Roche, S.; Bøggild, P.; Borini, S.; Koppens, F. H. L.; Palermo, V.; Pugno, N.; Garrido, J. A.; Sordan, R.; Bianco, A.; Ballerini, L.; Prato, M.; Lidorikis, E.; Kivioja, J.; Marinelli, C.; Ryhänen, T.; Morpurgo, A.; Coleman, J. N.; Nicolosi, V.; Colombo, L.; Fert, A.; Garcia-Hernandez, M.; Bachtold, A.; Schneider, G. F.; Guinea, F.; Dekker, C.; Barbone, M.; Sun, Z.; Galiotis, C.; Grigorenko, A. N.; Konstantatos, G.; Kis, A.; Katsnelson, M.; Vandersypen, L.; Loiseau, A.; Morandi, V.; Neumaier, D.; Treossi, E.; Pellegrini, V.; Polini, M.; Tredicucci, A.; Williams, G. M.; Hee Hong, B.; Ahn, J. H.; Min Kim, J.; Zirath, H.; Van Wees, B. J.; Van Der Zant, H.; Occhipinti, L.; Di Matteo, A.; Kinloch, I. A.; Seyller, T.; Quesnel, E.; Feng, X.; Teo, K.; Rupesinghe, N.; Hakonen, P.; Neil, S. R. T.; Tannock, Q.; Löfwander, T.; Kinaret, J. Science and Technology Roadmap for Graphene, Related Two-Dimensional Crystals, and Hybrid Systems. *Nanoscale* **2015**, *7* (11), 4598–4810. https://doi.org/10.1039/c4nr01600a.

(8) Pomerantseva, E.; Bonaccorso, F.; Feng, X.; Cui, Y.; Gogotsi, Y. Energy Storage: The Future Enabled by Nanomaterials. *Science (1979)* **2019**, *366* (6468). https://doi.org/10.1126/science.aan8285.

(9) Bonaccorso, F.; Colombo, L.; Yu, G.; Stoller, M.; Tozzini, V.; Ferrari, A. C.; Ruoff, R. S.; Pellegrini, V. Graphene, Related Two-Dimensional Crystals, and Hybrid Systems for Energy Conversion and Storage. *Science (1979)* **2015**, *347* (6217). https://doi.org/10.1126/science.1246501.

(10) Ansaldo, A.; Bondavalli, P.; Bellani, S.; del Rio Castillo, A. E.; Prato, M.; Pellegrini, V.; Pognon, G.; Bonaccorso, F. High-Power Graphene–Carbon Nanotube Hybrid Supercapacitors. *ChemNanoMat* **2017**, *3* (6), 436–446. https://doi.org/10.1002/cnma.201700093.

(11) Service, R. F. Beyond Graphene. *Science (1979)* **2015**, *348* (6234), 490–492. https://doi.org/10.1126/science.348.6234.490.

(12) Bonaccorso, F.; Colombo, L.; Yu, G.; Stoller, M.; Tozzini, V.; Ferrari, A. C.; Ruoff, R. S.; Pellegrini, V. Graphene, Related Two-Dimensional Crystals, and Hybrid Systems for Energy Conversion and Storage. *Science (1979)* **2015**, *347* (6217). https://doi.org/10.1126/science.1246501.

(13) Hassoun, J.; Bonaccorso, F.; Agostini, M.; Angelucci, M.; Betti, M. G.; Cingolani, R.; Gemmi, M.; Mariani, C.; Panero, S.; Pellegrini, V.; Scrosati, B. An Advanced Lithium-Ion Battery Based on a

Graphene Anode and a Lithium Iron Phosphate Cathode. *Nano Lett* **2014**, *14* (8), 4901–4906. https://doi.org/10.1021/nl502429m.

(14) Bellani, S.; Wang, F.; Longoni, G.; Najafi, L.; Oropesa-Nuñez, R.; Del Rio Castillo, A. E.; Prato, M.; Zhuang, X.; Pellegrini, V.; Feng, X.; Bonaccorso, F. WS2-Graphite Dual-Ion Batteries. *Nano Lett* **2018**, *18* (11), 7155–7164. https://doi.org/10.1021/acs.nanolett.8b03227.

(15) Balendhran, S.; Walia, S.; Nili, H.; Sriram, S.; Bhaskaran, M. Elemental Analogues of Graphene: Silicene, Germanene, Stanene, and Phosphorene. *Small*. Wiley-VCH Verlag February 11, 2015, pp 640–652. https://doi.org/10.1002/smll.201402041.

(16) Das, S.; Zhang, W.; Demarteau, M.; Hoffmann, A.; Dubey, M.; Roelofs, A. Tunable Transport Gap in Phosphorene. *Nano Lett* **2014**, *14* (10), 5733–5739. https://doi.org/10.1021/nl5025535.

(17) Zhang, S.; Yang, J.; Xu, R.; Wang, F.; Li, W.; Ghufran, M.; Zhang, Y. W.; Yu, Z.; Zhang, G.; Qin, Q.; Lu, Y. Extraordinary Photoluminescence and Strong Temperature/Angle-Dependent Raman Responses in Few-Layer Phosphorene. *ACS Nano* **2014**, *8* (9), 9590–9596. https://doi.org/10.1021/nn503893j.

(18) Chhowalla, M.; Shin, H. S.; Eda, G.; Li, L. J.; Loh, K. P.; Zhang, H. The Chemistry of Two-Dimensional Layered Transition Metal Dichalcogenide Nanosheets. *Nature Chemistry*. April 2013, pp 263–275. https://doi.org/10.1038/nchem.1589.

(19) Mattheiss, L. F. Band Structures of Transition-Metal-Dichalcogenide Layer Compounds. *Phys Rev B* **1973**, *8* (8), 3719–3740. https://doi.org/10.1103/PhysRevB.8.3719.

(20) Mak, K. F.; Lee, C.; Hone, J.; Shan, J.; Heinz, T. F. Atomically Thin MoS2: A New Direct-Gap Semiconductor. *Phys Rev Lett* **2010**, *105* (13). https://doi.org/10.1103/PhysRevLett.105.136805.

(21) Xiao, D.; Liu, G. bin; Feng, W.; Xu, X.; Yao, W. Coupled Spin and Valley Physics in Monolayers of MoS 2 and Other Group-VI Dichalcogenides. *Phys Rev Lett* **2012**, *108* (19). https://doi.org/10.1103/PhysRevLett.108.196802.

(22) Bonaccorso, F.; Bartolotta, A.; Coleman, J. N.; Backes, C. 2D-Crystal-Based Functional Inks. *Advanced Materials* **2016**, *28* (29), 6136–6166. https://doi.org/10.1002/adma.201506410.

(23) Najafi, L.; Bellani, S.; Oropesa-Nuñez, R.; Ansaldo, A.; Prato, M.; Del Rio Castillo, A. E.; Bonaccorso, F. Engineered MoSe2 -Based Heterostructures for Efficient Electrochemical Hydrogen Evolution Reaction. *Adv Energy Mater* **2018**, *8* (16), 1703212. https://doi.org/10.1002/aenm.201703212.

(24) Kakavelakis, G.; Del Rio Castillo, A. E.; Pellegrini, V.; Ansaldo, A.; Tzourmpakis, P.; Brescia, R.; Prato, M.; Stratakis, E.; Kymakis, E.; Bonaccorso, F. Size-Tuning of WSe2 Flakes for High Efficiency Inverted Organic Solar Cells. *ACS Nano* **2017**, *11* (4), 3517–3531. https://doi.org/10.1021/acsnano.7b00323.

(25) Najafi, L.; Bellani, S.; Oropesa-Nuñez, R.; Martín-García, B.; Prato, M.; Mazánek, V.; Debellis, D.; Lauciello, S.; Brescia, R.; Sofer, Z.; Bonaccorso, F. Niobium Disulphide (NbS2)-Based (Heterogeneous) Electrocatalysts for an Efficient Hydrogen Evolution Reaction. *J Mater Chem A Mater* **2019**, *7* (44), 25593–25608. https://doi.org/10.1039/c9ta07210a.

(26) Browne, M. P.; Sofer, Z.; Pumera, M. Layered and Two Dimensional Metal Oxides for Electrochemical Energy Conversion. *Energy and Environmental Science*. Royal Society of Chemistry January 1, 2019, pp 41–58. https://doi.org/10.1039/c8ee02495b.

(27) Kalantar-zadeh, K.; Ou, J. Z.; Daeneke, T.; Mitchell, A.; Sasaki, T.; Fuhrer, M. S. Two Dimensional and Layered Transition Metal Oxides. *Applied Materials Today*. Elsevier Ltd December 1, 2016, pp 73–89. https://doi.org/10.1016/j.apmt.2016.09.012.

(28) Ma, R.; Sasaki, T. Nanosheets of Oxides and Hydroxides: Ultimate 2D Charge-Bearing Functional Crystallites. *Advanced Materials*. December 1, 2010, pp 5082–5104. https://doi.org/10.1002/adma.201001722.

(29) Huheey, J. E.; Keiter, E. A.; Keiter, R. L. *Inorganic Chemistry: Principles of Structure and Reactivity*; Pearson College Div, 1993.

(30) Hall, D. S.; Lockwood, D. J.; Bock, C.; MacDougall, B. R. Nickel Hydroxides and Related Materials: A Review of Their Structures, Synthesis and Properties. *Proceedings of the Royal Society A: Mathematical, Physical and Engineering Sciences* **2015**, *471* (2174). https://doi.org/10.1098/rspa.2014.0792.

(31) Coronado, E.; Galán-Mascarós, J. R.; Martí-Gastaldo, C.; Ribera, A.; Palacios, E.; Castro, M.; Burriel, R. Spontaneous Magnetization in Ni−Al and Ni−Fe Layered Double Hydroxides. *Inorg Chem* **2008**, *47* (19), 9103–9110. https://doi.org/10.1021/ic801123v.

(32) Hermet, P.; Gourrier, L.; Bantignies, J. L.; Ravot, D.; Michel, T.; Deabate, S.; Boulet, P.; Henn, F. Dielectric, Magnetic, and Phonon Properties of Nickel Hydroxide. *Phys Rev B Condens Matter Mater Phys* **2011**, *84* (23), 1–10. https://doi.org/10.1103/PhysRevB.84.235211.

(33) Enoki, T.; Tsujikawa, I. Specific Heat of a Qusai-Two-Dimensional Antiferromagnet Ni(OH)2. *J Physical Soc Japan* **1978**, *45* (5), 1515–1519. https://doi.org/10.1143/JPSJ.45.1515.

(34) Almansa, J. J.; Coronado, E.; Martí-Gastaldo, C.; Ribera, A. Magnetic Properties of NiIICrIII Layered Double Hydroxide Materials. *Eur J Inorg Chem* **2008**, No. 36, 5642–5648. https://doi.org/10.1002/ejic.200800658.

(35) Oliver-Tolentino, M. A.; Vázquez-Samperio, J.; Manzo-Robledo, A.; González-Huerta, R. D. G.; Flores-Moreno, J. L.; Ramírez-Rosales, D.; Guzmán-Vargas, A. An Approach to Understanding the Electrocatalytic Activity Enhancement by Superexchange Interaction toward OER in Alkaline Media of Ni-Fe LDH. *Journal of Physical Chemistry C* **2014**, *118* (39), 22432–22438. https://doi.org/10.1021/jp506946b.

(36) Melot, B. C.; Tarascon, J.-M. Design and Preparation of Materials for Advanced Electrochemical Storage. *Acc Chem Res* **2013**. https://doi.org/10.1021/AR300088Q.

(37) Manthiram, A. A Reflection on Lithium-Ion Battery Cathode Chemistry. *Nature Communications*. Nature Research December 1, 2020. https://doi.org/10.1038/s41467-020-15355-0.

(38) Pinnavaia, T. J. Intercalated Clay Catalysts. *Science (1979)* **1983**, *220* (4595), 365–371. https://doi.org/10.1126/science.220.4595.365.

(39) Barast, G.; Razakamanantsoa, A. R.; Djeran-Maigre, I.; Nicholson, T.; Williams, D. Swelling Properties of Natural and Modified Bentonites by Rheological Description. *Appl Clay Sci* **2017**, *142*, 60–68. https://doi.org/10.1016/j.clay.2016.01.008.

(40) Luckham, P. F.; Rossi, S. The Colloidal and Rheological Properties of Bentonite Suspensions. *Adv Colloid Interface Sci* **1999**, *82* (1–3), 43–92. https://doi.org/10.1016/S0001-8686(99)00005-6.

(41) Zamora-Ledezma, C.; Narváez-Muñoz, C.; Guerrero, V. H.; Medina, E.; Meseguer-Olmo, L. Nanofluid Formulations Based on Two-Dimensional Nanoparticles, Their Performance, and Potential Application as Water-Based Drilling Fluids. *ACS Omega*. American Chemical Society June 21, 2022, pp 20457–20476. https://doi.org/10.1021/acsomega.2c02082.

(42) Sangian, D.; Naficy, S.; Dehghani, F.; Yamauchi, Y. A Review on Layered Mineral Nanosheets Intercalated with Hydrophobic/Hydrophilic Polymers and Their Applications. *Macromolecular Chemistry and Physics*. Wiley-VCH Verlag July 1, 2018. https://doi.org/10.1002/macp.201800142.

(43) Srivastava, S. K.; Singh, I. P. Hybrid Epoxy Nanocomposites: Lightweight Materials for Structural Applications. *Polym J* **2012**, *44* (4), 334–339. https://doi.org/10.1038/pj.2011.140.

(44) Moraes, J. D. D.; Bertolino, S. R. A.; Cuffini, S. L.; Ducart, D. F.; Bretzke, P. E.; Leonardi, G. R. Clay Minerals: Properties and Applications to Dermocosmetic Products and Perspectives of Natural Raw Materials for Therapeutic Purposes—A Review. *International Journal of Pharmaceutics*. Elsevier B.V. December 20, 2017, pp 213–219. https://doi.org/10.1016/j.ijpharm.2017.10.031.

(45) TITE, M. S.; BIMSON, M.; COWELL, M. R. Technological Examination of Egyptian Blue; 1984; pp 215–242. https://doi.org/10.1021/ba-1984-0205.ch011.

(46) Sgamellotti, A.; Anselmi, C. An Evergreen Blue. Spectroscopic Properties of Egyptian Blue from Pyramids to Raphael, and Beyond. *Inorganica Chimica Acta*. Elsevier B.V. January 24, 2022. https://doi.org/10.1016/j.ica.2021.120699.

(47) Selvaggio, G.; Kruss, S. Preparation, Properties and Applications of near-Infrared Fluorescent Silicate Nanosheets. *Nanoscale*. Royal Society of Chemistry June 22, 2022, pp 9553–9575. https://doi.org/10.1039/d2nr02967g.

(48) DeHoff Robert. *Thermodynamics in Materials Science*, 2nd ed.; Taylor & Francis, 2006.

(49) Owens, D. K.; Wendt, R. C. Estimation of the Surface Free Energy of Polymers. *J Appl Polym Sci* **1969**, *13* (8), 1741–1747. https://doi.org/10.1002/app.1969.070130815.

(50) Nicolosi, V.; Chhowalla, M.; Kanatzidis, M. G.; Strano, M. S.; Coleman, J. N. Liquid Exfoliation of Layered Materials. *Science (1979)* **2013**, *340* (6139), 72–75. https://doi.org/10.1126/science.1226419.

(51) Barton, A. F. M. Solubility Parameters. *Chem Rev* **1975**, *75* (6), 731–753. https://doi.org/10.1021/cr60298a003.

(52) Harvey, A.; He, X.; Godwin, I. J.; Backes, C.; McAteer, D.; Berner, N. C.; McEvoy, N.; Ferguson, A.; Shmeliov, A.; Lyons, M. E. G.; Nicolosi, V.; Duesberg, G. S.; Donegan, J. F.; Coleman, J. N. Production of Ni(OH)2 Nanosheets by Liquid Phase Exfoliation: From Optical Properties to Electrochemical Applications. *J Mater Chem A Mater* **2016**, *4* (28), 11046–11059. https://doi.org/10.1039/c6ta02811j.

(53) Mills, S. J.; Christy, A. G.; Génin, J.-M. R.; Kameda, T.; Colombo, F. Nomenclature of the Hydrotalcite Supergroup: Natural Layered Double Hydroxides. *Mineral Mag* **2012**, *76* (5), 1289–1336. https://doi.org/10.1180/minmag.2012.076.5.10.

(54) Cavani, F.; Trifirò, F.; Vaccari, A. Hydrotalcite-Type Anionic Clays: Preparation, Properties and Applications. *Catal Today* **1991**, *11* (2), 173–301. https://doi.org/10.1016/0920-5861(91)80068-K.

(55) Hochstetter, C. Untersuchung Über Die Zusammensetzung Einiger Mineralien. *Journal für praktische Chemie* **1842**, *27* (1), 375–378.

(56) Bejoy, N. Hydrotalcite. *Resonance* **2001**, *6* (2), 57–61. https://doi.org/10.1007/BF02836942.

(57) Mir, Z. M.; Bastos, A.; Höche, D.; Zheludkevich, M. L. Recent Advances on the Application of Layered Double Hydroxides in Concrete-A Review. *Materials* **2020**, *13* (6). https://doi.org/10.3390/ma13061426.

(58) Shao, M.; Zhang, R.; Li, Z.; Wei, M.; Evans, D. G.; Duan, X. Layered Double Hydroxides toward Electrochemical Energy Storage and Conversion: Design, Synthesis and Applications. *Chemical Communications*. Royal Society of Chemistry 2015, pp 15880–15893. https://doi.org/10.1039/c5cc07296d.

(59) Wang, Q.; Ohare, D. Recent Advances in the Synthesis and Application of Layered Double Hydroxide (LDH) Nanosheets. *Chem Rev* **2012**, *112* (7), 4124–4155. https://doi.org/10.1021/cr200434v.

(60) Song, F.; Bai, L.; Moysiadou, A.; Lee, S.; Hu, C.; Liardet, L.; Hu, X. Transition Metal Oxides as Electrocatalysts for the Oxygen Evolution Reaction in Alkaline Solutions: An Application-Inspired Renaissance. *J Am Chem Soc* **2018**, *140* (25), 7748–7759. https://doi.org/10.1021/jacs.8b04546.

(61) Yin, Q.; Rao, D.; Zhang, G.; Zhao, Y.; Han, J.; Lin, K.; Zheng, L.; Zhang, J.; Zhou, J.; Wei, M. CoFe–Cl Layered Double Hydroxide: A New Cathode Material for High-Performance Chloride Ion Batteries. *Adv Funct Mater* **2019**, *29* (36). https://doi.org/10.1002/adfm.201900983.

(62) Luo, J.; Yin, Q.; Zhang, J.; Zhang, S.; Zheng, L.; Han, J. NiMn-Cl Layered Double Hydroxide/Carbon Nanotube Networks for High-Performance Chloride Ion Batteries. *ACS Appl Energy Mater* **2020**, *3* (5), 4559–4568. https://doi.org/10.1021/acsaem.0c00224.

(63) Duval, S.; Baymann, F.; Schoepp-Cothenet, B.; Trolard, F.; Bourrié, G.; Grauby, O.; Branscomb, E.; Russell, M. J.; Nitschke, W. Fougerite: The Not so Simple Progenitor of the First Cells. *Interface Focus*. Royal Society Publishing December 6, 2019. https://doi.org/10.1098/rsfs.2019.0063.

(64) Duval, S.; Branscomb, E.; Trolard, F.; Bourrié, G.; Grauby, O.; Heresanu, V.; Schoepp-Cothenet, B.; Zuchan, K.; Russell, M. J.; Nitschke, W. On the Why's and How's of Clay Minerals' Importance in Life's Emergence. *Appl Clay Sci* **2020**, *195*. https://doi.org/10.1016/j.clay.2020.105737.

(65) Sławiński, W. A.; Sjåstad, A. O.; Fjellvåg, H. Stacking Faults and Polytypes for Layered Double Hydroxides: What Can We Learn from Simulated and Experimental X-Ray Powder Diffraction Data? *Inorg Chem* **2016**, *55* (24), 12881–12889. https://doi.org/10.1021/acs.inorgchem.6b02247.

(66) Radha, A. v.; Kamath, P. V.; Shivakumara, C. Conservation of Order, Disorder, and "Crystallinity" during Anion-Exchange Reactions among Layered Double Hydroxides (LDHs) of Zn with Al. *Journal of Physical Chemistry B* **2007**, *111* (13), 3411–3418. https://doi.org/10.1021/jp0684170.

(67) Hines, D. R.; Seidler, G. T.; Treacy, M. M. J.; Solin, S. A. Random Stacking of a Commensurate Guest Layer in an Ordered Host: Ni/Al Layer-Double-Hydroxides. *Solid State Commun* **1997**, *101* (11), 835–839. https://doi.org/10.1016/S0038-1098(96)00682-5.

(68) Malherbe, F.; Bigey, L.; Forano, C.; de Roy, A.; Besse, J. P. Structural Aspects and Thermal Properties of Takovite-like Layered Double Hydroxides Pillared with Chromium Oxo-Anions. *Journal of the Chemical Society - Dalton Transactions* **1999**, No. 21, 3831–3839. https://doi.org/10.1039/a903766g.

(69) Zhang, J.; Zhang, F.; Ren, L.; Evans, D. G.; Duan, X. Synthesis of Layered Double Hydroxide Anionic Clays Intercalated by Carboxylate Anions. *Mater Chem Phys* **2004**, *85* (1), 207–214. https://doi.org/10.1016/j.matchemphys.2004.01.020.

(70) Tronto, J.; dos Reis, M. J.; Silvério, F.; Balbo, V. R.; Marchetti, J. M.; Valim, J. B. In Vitro Release of Citrate Anions Intercalated in Magnesium Aluminium Layered Double Hydroxides. *Journal of Physics and Chemistry of Solids* **2004**, *65* (2–3), 475–480. https://doi.org/10.1016/j.jpcs.2003.09.019.

(71) Li, Z. Q.; Lu, C. J.; Xia, Z. P.; Zhou, Y.; Luo, Z. X-Ray Diffraction Patterns of Graphite and Turbostratic Carbon. *Carbon N Y* **2007**, *45* (8), 1686–1695. https://doi.org/10.1016/j.carbon.2007.03.038.

(72) Putman, K. J.; Rowles, M. R.; Marks, N. A.; Suarez-Martinez, I. The Role of the 2D-to-3D Transition in x-Ray Diffraction Analysis of Crystallite Size. *Journal of Physics Condensed Matter* **2021**, *33* (29). https://doi.org/10.1088/1361-648X/ac0083.

(73) Yu, W.; Li, H.; Du, N.; Hou, W. Estimation of Surface Free Energy and Solubility Parameters of Mg–Al Layered Double Hydroxides. *J Colloid Interface Sci* **2019**, *546*, 361–370. https://doi.org/10.1016/j.jcis.2019.03.078.

(74) Hibino, T.; Jones, W. New Approach to the Delamination of Layered Double Hydroxides. *J Mater Chem* **2001**, *11* (5), 1321–1323. https://doi.org/10.1039/b101135i.

(75) Wang, Q.; O'Hare, D. Recent Advances in the Synthesis and Application of Layered Double Hydroxide (LDH) Nanosheets. *Chem Rev* **2012**, *112* (7), 4124–4155. https://doi.org/10.1021/cr200434v.

(76) Gardner, E.; Huntoon, K. M.; Pinnavaia, T. J. Direct Synthesis of Alkoxide-Intercalated Derivatives of Hydrotalcite-like Layered Double Hydroxides: Precursors for the Formation of Colloidal Layered Double Hydroxide Suspensions and Transparent Thin Films. *Advanced Materials* **2001**, *13* (16), 1263–1266. https://doi.org/10.1002/1521-4095(200108)13:16<1263::AID-ADMA1263>3.0.CO;2-R.

(77) Hibino, T.; Kobayashi, M. Delamination of Layered Double Hydroxides in Water. *J Mater Chem* **2005**, *15* (6), 653–656. https://doi.org/10.1039/b416913a.

(78) Xu, Z. P.; Jin, Y.; Liu, S.; Hao, Z. P.; Lu, G. Q. (Max). Surface Charging of Layered Double Hydroxides during Dynamic Interactions of Anions at the Interfaces. *J Colloid Interface Sci* **2008**, *326* (2), 522–529. https://doi.org/10.1016/j.jcis.2008.06.062.

(79) Hou, W.; Kang, L.; Sun, R.; Liu, Z. H. Exfoliation of Layered Double Hydroxides by an Electrostatic Repulsion in Aqueous Solution. *Colloids Surf A Physicochem Eng Asp* **2008**, *312* (2–3), 92–98. https://doi.org/10.1016/j.colsurfa.2007.06.036.

(80) Kumar, P. P.; Kalinichev, A. G.; Kirkpatrick, R. J. Molecular Dynamics Simulation of the Energetics and Structure of Layered Double Hydroxides Intercalated with Carboxylic Acids. *Journal of Physical Chemistry C* **2007**, *111* (36), 13517–13523. https://doi.org/10.1021/jp0732054.

(81) Kumar, P. P.; Kalinichev, A. G.; Kirkpatrick, R. J. Hydration, Swelling, Interlayer Structure, and Hydrogen Bonding in Organolayered Double Hydroxides: Insights from Molecular Dynamics Simulation of Citrate-Intercalated Hydrotalcite. *Journal of Physical Chemistry B* **2006**, *110* (9), 3841–3844. https://doi.org/10.1021/jp057069j.

(82) Pavlovic, M.; Huber, R.; Adok-Sipiczki, M.; Nardin, C.; Szilagyi, I. Ion Specific Effects on the Stability of Layered Double Hydroxide Colloids. *Soft Matter* **2016**, *12* (17), 4024–4033. https://doi.org/10.1039/c5sm03023d.

(83) Yu, W.; Du, N.; Gu, Y.; Yan, J.; Hou, W. Specific Ion Effects on the Colloidal Stability of Layered Double Hydroxide Single-Layer Nanosheets. *Langmuir* **2020**, *36* (23), 6557–6568. https://doi.org/10.1021/acs.langmuir.0c01089.

(84) Avlovic, M.; Rouster, P.; Amas Oncsik, T.; Szilagyi, I. Tuning Colloidal Stability of Layered Double Hydroxides: From Monovalent Ions to Polyelectrolytes. **2017**, *82*, 121–131. https://doi.org/10.1002/cplu.v82.1.

(85) Hamann, C. H.; Hamnett, A.; Vielstich, W. *Electrochemistry*; Wiley-VCH Verlag, 2007.

(86) Hamaker, H. C. The London—van Der Waals Attraction between Spherical Particles. *Physica* **1937**, *4* (10), 1058–1072. https://doi.org/10.1016/S0031-8914(37)80203-7.

(87) Jaśkaniec, S.; Hobbs, C.; Seral-Ascaso, A.; Coelho, J.; Browne, M. P.; Tyndall, D.; Sasaki, T.; Nicolosi, V. Low-Temperature Synthesis and Investigation into the Formation Mechanism of High Quality Ni-Fe Layered Double Hydroxides Hexagonal Platelets. *Sci Rep* **2018**, *8* (1), 4–11. https://doi.org/10.1038/s41598-018-22630-0.

(88) Meyn, M.; Beneke, K.; Lagaly, G. Anion-Exchange Reactions of Layered Double Hydroxides. *Inorg Chem* **1990**, *29* (26), 5201–5207. https://doi.org/10.1021/ic00351a013.

(89) Bino, A.; Shweky, I.; Cohen, S.; Bauminger, E. R.; Lippard, S. J. A Novel Nonairon(III) Citrate Complex: A “Ferric Triple-Decker.” *Inorg Chem* **1998**, *37* (20), 5168–5172. https://doi.org/10.1021/ic9715658.

(90) Spiro, T. G.; Pape, L.; Saltman, P. The Hydrolytic Polymerization of Ferric Citrate. I. The Chemistry of the Polymer. *J Am Chem Soc* **1967**, *89* (22), 5555–5559. https://doi.org/10.1021/ja00998a008.

(91) Abellán, G.; Carrasco, J. A.; Coronado, E. Room Temperature Magnetism in Layered Double Hydroxides Due to Magnetic Nanoparticles. *Inorg Chem* **2013**, *52* (14), 7828–7830. https://doi.org/10.1021/ic400883k.

(92) Silva, A. M. N.; Kong, X.; Hider, R. C. Determination of the PKa Value of the Hydroxyl Group in the α-Hydroxycarboxylates Citrate, Malate and Lactate by 13C NMR: Implications for Metal Coordination in Biological Systems. *BioMetals* **2009**, *22* (5), 771–778. https://doi.org/10.1007/s10534-009-9224-5.

(93) Boclair, J. W.; Braterman, P. S. Layered Double Hydroxide Stability. 1. Relative Stabilities of Layered Double Hydroxides and Their Simple Counterparts. *Chemistry of Materials* **1999**, *11* (2), 298–302. https://doi.org/10.1021/cm980523u.

(94) Atkins, P.; de Paula, J. *Atkins’ Physical Chemistry*, 9th ed.; OUP Oxford, 2009.

(95) Shinagawa, T.; Garcia-Esparza, A. T.; Takanabe, K. Insight on Tafel Slopes from a Microkinetic Analysis of Aqueous Electrocatalysis for Energy Conversion. *Sci Rep* **2015**, *5* (May), 1–21. https://doi.org/10.1038/srep13801.

(96) Anantharaj, S.; Ede, S. R.; Karthick, K.; Sam Sankar, S.; Sangeetha, K.; Karthik, P. E.; Kundu, S. Precision and Correctness in the Evaluation of Electrocatalytic Water Splitting: Revisiting Activity Parameters with a Critical Assessment. *Energy Environ Sci* **2018**, *11* (4), 744–771. https://doi.org/10.1039/c7ee03457a.

(97) Hunter, B. M.; Hieringer, W.; Winkler, J. R.; Gray, H. B.; Müller, A. M. Effect of Interlayer Anions on [NiFe]-LDH Nanosheet Water Oxidation Activity. *Energy Environ Sci* **2016**, *9* (5), 1734–1743. https://doi.org/10.1039/c6ee00377j.

(98) Anantharaj, S.; Kundu, S. Do the Evaluation Parameters Reflect Intrinsic Activity of Electrocatalysts in Electrochemical Water Splitting? *ACS Energy Lett* **2019**, *4* (6), 1260–1264. https://doi.org/10.1021/acsenergylett.9b00686.

(99) Doyle, R. L.; Godwin, I. J.; Brandon, M. P.; Lyons, M. E. G. Redox and Electrochemical Water Splitting Catalytic Properties of Hydrated Metal Oxide Modified Electrodes. *Physical Chemistry Chemical Physics* **2013**, *15* (33), 13737. https://doi.org/10.1039/c3cp51213d.

(100) Lyons, M. E. G.; Doyle, R. L.; Godwin, I.; O'Brien, M.; Russell, L. Hydrous Nickel Oxide: Redox Switching and the Oxygen Evolution Reaction in Aqueous Alkaline Solution. *J Electrochem Soc* **2012**, *159* (12), H932–H944. https://doi.org/10.1149/2.078212jes.

(101) Boclair, J. W.; Braterman, P. S.; Jiang, J.; Lou, S.; Yarberry, F. Layered Double Hydroxide Stability. 2. Formation of Cr(III)-Containing Layered Double Hydroxides Directly from Solution. *Chemistry of Materials* **1999**, *11* (2), 303–307. https://doi.org/10.1021/cm980524m.

(102) Strouse, J.; Layten, S. W.; Strouse, C. E. Structural Studies of Transition Metal Complexes of Triionized and Tetraionized Citrate. Models for the Coordination of the Citrate Ion to Transition Metal Ions in Solution and at the Active Site of Aconitase. *J Am Chem Soc* **1977**, *99* (2), 562–572. https://doi.org/10.1021/ja00444a041.

(103) Silva, A. M. N.; Kong, X.; Parkin, M. C.; Cammack, R.; Hider, R. C. Iron(III) Citrate Speciation in Aqueous Solution. *Dalton Transactions* **2009**, No. 40, 8616–8625. https://doi.org/10.1039/b910970f.

(104) Baker, E. N.; Baker, H. M.; Anderson, B. F.; Reeves, R. D. Chelation of Nickel(II) by Citrate. The Crystal Structure of a Nickel-Citrate Complex, K2[Ni(C6H5O7)(H2O)2]2·4H2O. *Inorganica Chim Acta* **1983**, *78* (C), 281–285. https://doi.org/10.1016/S0020-1693(00)86530-5.

(105) Still, E. R.; Wikberg, P. Solution Studies of Systems with Polynuclear Complex Formation. 2. The Nickel(II) Citrate System. *Inorganica Chim Acta* **1980**, *46* (C), 153–155. https://doi.org/10.1016/S0020-1693(00)84184-5.

(106) Murrie, M.; Stoeckli-Evans, H.; Güdel, H. U. Assembly of Ni7 and Ni21 Molecular Clusters by Using Citric Acid. *Angewandte Chemie - International Edition* **2001**, *40* (10), 1957–1960. https://doi.org/10.1002/1521-3773(20010518)40:10<1957::AID-ANIE1957>3.0.CO;2-S.

(107) Beverskog, B.; Puigdomenech, I. Revised Pourbaix Diagrams for Zinc at 25–300 °C. *Corros Sci* **1997**, *39* (1), 107–114. https://doi.org/10.1016/S0010-938X(97)89246-3.

(108) Oehman, L. O. Equilibrium and Structural Studies of Silicon(IV) and Aluminum(III) in Aqueous Solution. 17. Stable and Metastable Complexes in the System Hydrogen (+)-Aluminum(3+)-Citric Acid. *Inorg Chem* **1988**, *27* (15), 2565–2570. https://doi.org/10.1021/ic00288a003.

(109) Sugano, S.; Tanabe, Y.; Kamimura, H. Pure and Applied Physics: A Series of Monographs and Textbooks. In *Pure and applied physics v. 33.*; 1970; Vol. 33, pp 332–333. https://doi.org/10.1016/b978-0-12-676050-7.50027-5.

(110) Sherman, D. M.; Waite, T. D. Electronic Spectra of Fe3+ Oxides and Oxide Hydroxides in the near IR to near UV. *American Mineralogist* **1985**, *70* (11–12), 1262–1269.

(111) Sherman, D. M. The Electronic Structures of Fe3+ Coordination Sites in Iron Oxides: Applications to Spectra, Bonding, and Magnetism. *Phys Chem Miner* **1985**, *12* (3), 161–175. https://doi.org/10.1007/BF00308210.

(112) Krebs, J. J.; Maisch, W. G. Exchange Effects in the Optical-Absorption Spectrum of Fe3+ in Al2O3. *Phys. Rev. B* **1971**, *4* (3), 757–769. https://doi.org/10.1103/PhysRevB.4.757.

(113) McCarthy, P. J.; Güdel, H. U. Optical Spectroscopy of Exchange-Coupled Transition Metal Complexes. *Coord Chem Rev* **1988**, *88* (C), 69–131. https://doi.org/10.1016/0010-8545(88)80002-X.

(114) L. Lohr, L. Spin-Forbidden Electronic Excitations in Transition Metal Complexes. *Coord Chem Rev* **1972**, *8* (3), 241–259. https://doi.org/10.1016/S0010-8545(00)80030-2.

(115) Wenger, O. S.; Valiente, R.; Güdel, H. U.; Valiente, R. Optical Spectroscopy of the Ni2+-Doped Layer Perovskites Rb2MCl4 (M=Cd,Mn): Effects of Ni2+-Mn2+ Exchange Interactions on the Ni2+ Absorption, Luminescence, and Upconversion Properties. *Phys Rev B Condens Matter Mater Phys* **2001**, *64* (23), 1–8. https://doi.org/10.1103/PhysRevB.64.235116.

(116) Ferguson, J.; J. Guggenheim, H.; Tanabe, Y. The Effects of Exchange Interactions in the Spectra of Octahedral Manganese. II. Compounds. *J Physical Soc Japan* **1966**, *21* (4), 692–704. https://doi.org/10.1143/JPSJ.21.692.

(117) Ferguson, J.; Guggenheim, H. J.; Tanabe, Y. Absorption of Light by Pairs of Like and Unlike Transition-Metal Ions. *Phys Rev Lett* **1965**, *14* (18), 737–738. https://doi.org/10.1103/PhysRevLett.14.737.

(118) Rajendran, V.; Fang, M. H.; Huang, W. T.; Majewska, N.; Lesniewski, T.; Mahlik, S.; Leniec, G.; Kaczmarek, S. M.; Pang, W. K.; Peterson, V. K.; Lu, K. M.; Chang, H.; Liu, R. S. Chromium Ion Pair Luminescence: A Strategy in Broadband near-Infrared Light-Emitting Diode Design. *J Am Chem Soc* **2021**, *143* (45), 19058–19066. https://doi.org/10.1021/jacs.1c08334.

(119) Piccinni, M.; Bellani, S.; Bianca, G.; Bonaccorso, F. Nickel-Iron Layered Double Hydroxide Dispersions in Ethanol Stabilized by Acetate Anions. *Inorg Chem* **2022**, *61* (11), 4598–4608. https://doi.org/10.1021/acs.inorgchem.1c03485.

(120) Rudolf, C.; Dragoi, B.; Ungureanu, A.; Chirieac, A.; Royer, S.; Nastro, A.; Dumitriu, E. NiAl and CoAl Materials Derived from Takovite-like LDHs and Related Structures as Efficient Chemoselective Hydrogenation Catalysts. *Catal Sci Technol* **2014**, *4* (1), 179–189. https://doi.org/10.1039/c3cy00611e.

(121) Tanabe, Y.; Sugano, S. On the Absorption Spectra of Complex Ions. I. *J Physical Soc Japan* **1954**, *9* (5), 753–766. https://doi.org/10.1143/JPSJ.9.753.

(122) Tanabe, Y.; Sugano, S. On the Absorption Spectra of Complex Ions II. *J Physical Soc Japan* **1954**, *9* (5), 766–779. https://doi.org/10.1143/JPSJ.9.766.

(123) Tanabe, Y.; Sugano, S. On the Absorption Spectra of Complex Ions, III The Calculation of the Crystalline Field Strength. *J Physical Soc Japan* **1956**, *11* (8), 864–877. https://doi.org/10.1143/JPSJ.11.864.

(124) Jørgensen, Chr. K. Spectroscopy of Transition-Group Complexes; 2007; pp 33–146. https://doi.org/10.1002/9780470143513.ch2.

(125) Hahn Anselm. *Anselmoo / TanabeSugano* . https://github.com/Anselmoo/TanabeSugano (accessed 2022-10-05).

(126) Oppenheim Julius; Miller Jayce. *JulesOpp / Tanabe-Sugano* . https://github.com/JulesOpp/Tanabe-Sugano (accessed 2022-10-05).

(127) Marco Piccinni. *Tanabe-Sugano diagrams with MATLAB*. MATLAB Central File Exchange. https://www.mathworks.com/matlabcentral/fileexchange/117420-tanabe-sugano-diagrams (accessed 2022-09-12).

(128) Tchougréeff, A. L.; Dronskowski, R. Nephelauxetic Effect Revisited. *Int J Quantum Chem* **2009**, *109* (11), 2606–2621. https://doi.org/10.1002/qua.21989.

(129) Brik, M. G.; Camardello, S. J.; Srivastava, A. M.; Avram, N. M.; Suchocki, A. Spin-Forbidden Transitions in the Spectra of Transition Metal Ions and Nephelauxetic Effect. *ECS Journal of Solid State Science and Technology* **2016**, *5* (1), R3067–R3077. https://doi.org/10.1149/2.0091601jss.

(130) Kuleshov, N. V.; Shcherbitsky, V. G.; Mikhailov, V. P.; Kück, S.; Koetke, J.; Petermann, K.; Huber, G. Spectroscopy and Excited-State Absorption of Ni2+-Doped MgAl2O4. *J Lumin* **1997**, *71* (4), 265–268. https://doi.org/10.1016/S0022-2313(96)00284-0.

(131) Mironova-Ulmane, N.; Brik, M. G.; Sildos, I. Crystal Field Calculations of Energy Levels of the Ni2+ Ions in MgO. *J Lumin* **2013**, *135*, 74–78. https://doi.org/10.1016/j.jlumin.2012.10.026.

(132) Scheinost, A. C.; Ford, R. G.; Sparks, D. L. The Role of Al in the Formation of Secondary Ni Precipitates on Pyrophyllite, Gibbsite, Talc, and Amorphous Silica: A DRS Study. *Geochim Cosmochim Acta* **1999**, *63* (19–20), 3193–3203. https://doi.org/10.1016/S0016-7037(99)00244-6.

(133) González, E.; Rodrigue-Witchel, A.; Reber, C. Absorption Spectroscopy of Octahedral Nickel(II) Complexes: A Case Study of Interactions between Multiple Electronic Excited States. *Coordination Chemistry Reviews*. February 2007, pp 351–363. https://doi.org/10.1016/j.ccr.2006.08.011.

(134) Bussière, G.; Reber, C. Coupled Excited States in Nickel(II) Complexes Probed by Polarized Absorption Spectroscopy. *J Am Chem Soc* **1998**, *120* (25), 6306–6315. https://doi.org/10.1021/ja9740733.

(135) Reedijk, J.; van Leeuwen, P. W. N. M.; Groeneveld, W. L. A Semi-Empirical Energy-Level Diagram for Octahedral, Nickel(II) Complexes. *Recueil des Travaux Chimiques des Pays-Bas* **2010**, *87* (2), 129–143. https://doi.org/10.1002/recl.19680870203.

(136) Qi, Y.; Qi, H.; Li, J.; Lu, C. Synthesis, Microstructures and UV-Vis Absorption Properties of β-Ni(OH)2 Nanoplates and NiO Nanostructures. *J Cryst Growth* **2008**, *310* (18), 4221–4225. https://doi.org/10.1016/j.jcrysgro.2008.06.047.

(137) Poul, L.; Jouini, N.; Fievet, F. Layered Hydroxide Metal Acetates (Metal = Zinc, Cobalt, and Nickel): Elaboration via Hydrolysis in Polyol Medium and Comparative Study. *Chemistry of Materials* **2000**, *12* (10), 3123–3132. https://doi.org/10.1021/cm991179j.

(138) de Moura, A. P.; Lima, R. C.; Paris, E. C.; Li, M. S.; Varela, J. A.; Longo, E. Formation of β-Nickel Hydroxide Plate-like Structures under Mild Conditions and Their Optical Properties. *J Solid State Chem* **2011**, *184* (10), 2818–2823. https://doi.org/10.1016/j.jssc.2011.08.027.

(139) Brik, M. G.; Avram, N. M.; Avram, C. N. Comparative Crystal Field Study of Ni2+ Energy Levels in NiCl2, NiBr2, and NiI2 Crystals. *Physica B Condens Matter* **2006**, *371* (1), 43–49. https://doi.org/10.1016/j.physb.2005.09.034.

(140) Trotochaud, L.; Young, S. L.; Ranney, J. K.; Boettcher, S. W. Nickel-Iron Oxyhydroxide Oxygen-Evolution Electrocatalysts: The Role of Intentional and Incidental Iron Incorporation. *J Am Chem Soc* **2014**, *136* (18), 6744–6753. https://doi.org/10.1021/ja502379c.

(141) Louie, M. W.; Bell, A. T. An Investigation of Thin-Film Ni-Fe Oxide Catalysts for the Electrochemical Evolution of Oxygen. *J Am Chem Soc* **2013**, *135* (33), 12329–12337. https://doi.org/10.1021/ja405351s.

(142) Młynarek, G.; Paszkiewicz, M.; Radniecka, A. The Effect of Ferric Ions on the Behaviour of a Nickelous Hydroxide Electrode. *J Appl Electrochem* **1984**, *14* (2), 145–149. https://doi.org/10.1007/BF00618733.

(143) Friebel, D.; Louie, M. W.; Bajdich, M.; Sanwald, K. E.; Cai, Y.; Wise, A. M.; Cheng, M. J.; Sokaras, D.; Weng, T. C.; Alonso-Mori, R.; Davis, R. C.; Bargar, J. R.; Nørskov, J. K.; Nilsson, A.; Bell, A. T. Identification of Highly Active Fe Sites in (Ni,Fe)OOH for Electrocatalytic Water Splitting. *J Am Chem Soc* **2015**, *137* (3), 1305–1313. https://doi.org/10.1021/ja511559d.

(144) Trzešniewski, B. J.; Diaz-Morales, O.; Vermaas, D. A.; Longo, A.; Bras, W.; Koper, M. T. M.; Smith, W. A. In Situ Observation of Active Oxygen Species in Fe-Containing Ni-Based Oxygen Evolution Catalysts: The Effect of PH on Electrochemical Activity. *J Am Chem Soc* **2015**, *137* (48), 15112–15121. https://doi.org/10.1021/jacs.5b06814.

(145) Chen, J. Y. C.; Dang, L.; Liang, H.; Bi, W.; Gerken, J. B.; Jin, S.; Alp, E. E.; Stahl, S. S. Operando Analysis of NiFe and Fe Oxyhydroxide Electrocatalysts for Water Oxidation: Detection of Fe4+ by Mössbauer Spectroscopy. *J Am Chem Soc* **2015**, *137* (48), 15090–15093. https://doi.org/10.1021/jacs.5b10699.

(146) Anantharaj, S.; Kundu, S.; Noda, S. "The Fe Effect": A Review Unveiling the Critical Roles of Fe in Enhancing OER Activity of Ni and Co Based Catalysts. *Nano Energy* **2021**, *80* (February 2020), 105514. https://doi.org/10.1016/j.nanoen.2020.105514.

(147) Dang, L.; Liang, H.; Zhuo, J.; Lamb, B. K.; Sheng, H.; Yang, Y.; Jin, S. Direct Synthesis and Anion Exchange of Noncarbonate-Intercalated NiFe-Layered Double Hydroxides and the Influence on Electrocatalysis. *Chemistry of Materials* **2018**, *30* (13), 4321–4330. https://doi.org/10.1021/acs.chemmater.8b01334.

(148) Chen, B.; Zhang, Z.; Kim, S.; Lee, S.; Lee, J.; Kim, W.; Yong, K. Ostwald Ripening Driven Exfoliation to Ultrathin Layered Double Hydroxides Nanosheets for Enhanced Oxygen Evolution Reaction. *ACS Appl Mater Interfaces* **2018**, *10* (51), 44518–44526. https://doi.org/10.1021/acsami.8b16962.

(149) Gao, R.; Yan, D. Fast Formation of Single-Unit-Cell-Thick and Defect-Rich Layered Double Hydroxide Nanosheets with Highly Enhanced Oxygen Evolution Reaction for Water Splitting. *Nano Res* **2018**, *11* (4), 1883–1894. https://doi.org/10.1007/s12274-017-1806-x.

(150) Zhong, H.; Liu, T.; Zhang, S.; Li, D.; Tang, P.; Alonso-Vante, N.; Feng, Y. Template-Free Synthesis of Three-Dimensional NiFe-LDH Hollow Microsphere with Enhanced OER Performance in Alkaline Media. *Journal of Energy Chemistry* **2019**, *33*, 130–137. https://doi.org/10.1016/j.jechem.2018.09.005.

(151) Yang, X.; Pan, J.; Nie, Y.; Sun, Y.; Wan, P. A Facile and Scalable Complexation-Precipitation Method of Iron Doped Nickel Hydroxide Nanosheets as a Superior Oxygen Evolution Catalyst. *Int J Hydrogen Energy* **2017**, *42* (43), 26575–26585. https://doi.org/10.1016/j.ijhydene.2017.09.006.

(152) Zhao, Y.; Zhang, X.; Jia, X.; Waterhouse, G. I. N.; Shi, R.; Zhang, X.; Zhan, F.; Tao, Y.; Wu, L.-Z.; Tung, C.-H.; O'Hare, D.; Zhang, T. Sub-3 Nm Ultrafine Monolayer Layered Double Hydroxide Nanosheets for Electrochemical Water Oxidation. *Adv Energy Mater* **2018**, *8* (18), 1703585. https://doi.org/https://doi.org/10.1002/aenm.201703585.

(153) Shi, G.; Yu, C.; Fan, Z.; Li, J.; Yuan, M. Graphdiyne-Supported NiFe Layered Double Hydroxide Nanosheets as Functional Electrocatalysts for Oxygen Evolution. *ACS Appl Mater Interfaces* **2019**, *11* (3), 2662–2669. https://doi.org/10.1021/acsami.8b03345.

(154) Liu, H.; Zhou, J.; Wu, C.; Wang, C.; Zhang, Y.; Liu, D.; Lin, Y.; Jiang, H.; Song, L. Integrated Flexible Electrode for Oxygen Evolution Reaction: Layered Double Hydroxide Coupled with Single-Walled Carbon Nanotubes Film. *ACS Sustain Chem Eng* **2018**, *6* (3), 2911–2915. https://doi.org/10.1021/acssuschemeng.8b00084.